論文 / 著書情報
Article / Book Information

題目(和文)	数値流体力学的アプローチの導入に基づく防波堤及び魚礁の新しい設計・施工法の開発
Title(English)	Development of novel design and construction methods introducing computational fluid dynamics approach for breakwaters and artificial reefs
著者(和文)	三井順
Author(English)	Jun Mitsui
出典(和文)	学位:博士（工学）, 学位授与機関:東京工業大学, 報告番号:甲第9886号, 授与年月日:2015年3月26日, 学位の種別:課程博士, 審査員:灘岡　和夫,大佛　俊泰,鼎　信次郎,鍵　直樹,中村　隆志
Citation(English)	Degree:, Conferring organization: Tokyo Institute of Technology, Report number:甲第9886号, Conferred date:2015/3/26, Degree Type:Course doctor, Examiner:,,,,
学位種別(和文)	博士論文
Type(English)	Doctoral Thesis

Doctoral Dissertation

Development of Novel Design and Construction Methods Introducing Computational Fluid Dynamics Approach for Breakwaters and Artificial Reefs

Jun Mitsui

Supervisor : Professor Kazuo Nadaoka

Department of Mechanical and Environmental Informatics

Graduate School of Information Science and Engineering

Tokyo Institute of Technology

March 2015

Contents

Chapter 1

Introduction

1.1 Background

Japan is surrounded by the sea on all sides, and has achieved growth through the development of its coastal zones. Various marine structures have been constructed to protect lives from threats such as high waves, storm surges, and tsunamis, and to sustain the benefit brought by marine resources and the natural environment of the sea.

The 2011 Off the Pacific Coast of Tohoku Earthquake and Tsunami which occurred on 11 March 2011 took a heavy toll on human life. Marine structures including breakwaters were also severely damaged. One cause of breakwater failure was scouring of the rubble foundation and subsoil at the harbor-side of the breakwater due to overflow. This was a formerly inconceivable type of failure. It became necessary to completely reconsider the design method for the breakwaters (Ministry of Land, Infrastructure, Transport and Tourism of Japan [MLIT], 2013).

In breakwater design work, it is required to determine the mass of the armor units to ensure stability against tsunami overflow. However, the stability of armor units of composite breakwaters against tsunami overflow is not clear since this phenomenon was inconceivable before the Tohoku tsunami in 2011.

Guidelines for Tsunami-Resistant Design of Breakwaters (MLIT, 2013) mention the Isbash formula (Coastal Engineering Research Center [CERC], 1977) as the calculation method for the required mass of armor units against tsunami overflow. However, there are practical issues that the required mass is too sensitive to variations in the estimated flow velocity and that the applicability of the Isbash formula to the tsunami overflow remains unclear. Therefore, the establishment of a practical design method for the armor units against tsunami is an urgent issue.

On the other hand, taking a new look at the utilization of the sea area and the decrease of offshore fishery resources have also become an urgent issue. One example is the development project for fishing ports and grounds in the western part of the Sea of Japan. This has been implemented since FY2007 to recover and increase fishery resources in the offshore exclusive economic zone. This project implements artificial nursery reefs for snow crab and flathead flounder to recover and increase as resources on a national government initiative (e.g., Fisheries Agency of Japan, Construction Division, 2007; Nakamura et al., 2008). The nursery reefs are constructed by placing concrete blocks to a water depth of about 250 m.

Generally, such concrete blocks are placed on the sea bottom using wire ropes. However, this method proved uneconomical in the case of deep water because it took a long time to anchor a floating crane and install the blocks in such deep water. On the other hand, though a method of free-fall was deemed more economical, the accuracy of installation became a problem.

The study addresses the two issues mentioned above: development of a design method for armor units covering rubble mound of composite breakwaters against tsunami overflow, and development of an economical construction method of artificial reefs in deep sea areas. These are taken up and discussed as issues related to the design and construction methods of the concrete blocks in which the author is involved.

When considering these issues, laboratory experiments are essential. Computational fluid dynamics (CFD) approaches are also becoming powerful tools due to advances in numerical analysis technology and the improvement of the performance of computers. For example, a numerical wave flume based on the VOF method, named CADMAS-SURF (Coastal Development Institute of Technology, 2001) has been developed and applied to various problems such as wave overtopping and wave forces acting on structures. However, there are still few examples which treat the behavior of concrete blocks with complex shape in wave and current fields using numerical computation. To deal with the influence of block shape directly, it is necessary to set the grid size very small so that the block shape is reproduced. Numerical models based on a structured grid such as CADMAS-SURF are not a realistic method in terms of computation time because the number of computational grids is enormous.

In contrast, models based on an unstructured grid enable the computation time to be largely reduced since it is possible to locally subdivide the computational grid. An OpenFOAM CFD model is one of the numerical models based on an unstructured grid, and this is being applied to the field of coastal engineering recently (e.g., Jacobsen et al., 2012; Higuera et al., 2013). To apply this model as a numerical wave flume, however, it

is indispensable to validate various items such as wave generation, wave propagation and deformation, wave breaking, wave force on structures, and modeling of porous structures.

1.2 Objective of this Work

The aim of the study herein is to present novel design and construction methods for breakwaters and artificial reefs by introducing the CFD approach. Firstly, a general-purpose numerical wave flume is developed by using an OpenFOAM model. Then the stability of armor blocks covering a rubble mound of a composite breakwater against tsunami overflow is investigated by introducing a CFD approach with associated laboratory experiments for developing a new practical and accurate design method of armor concrete blocks. This study also addresses construction of artificial nursery reefs for snow crabs. The falling behavior of the fish reef blocks in water is investigated by laboratory experiments and numerical computation and an accurate and low-cost placement method by free-fall is developed.

1.3 Thesis Outline

Fig. 1.1 shows a schematic diagram of the research flow. The outline of the present thesis is as follows.

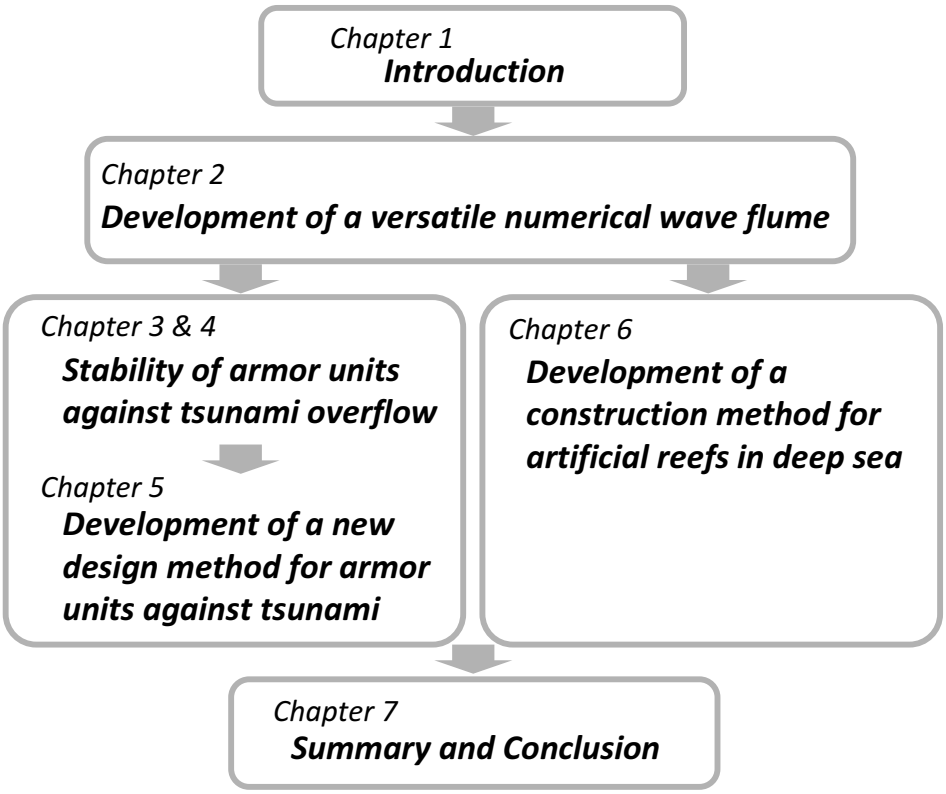

Figure 1.1 : Research flow.

In Chapter 2, a versatile numerical wave flume is developed by using an OpenFOAM model and is validated. Firstly, governing equations are outlined. The validation of the water surface profile and wave force acting on a structure is performed through dam-break tests. A wave generation method by reproducing a wavemaker is presented. The validation of the wave progression and deformation and the application to a flap-piston combined wavemaker are conducted. As a validation of the modeling of porous structures, analysis on the wave transmission of a sloping breakwater and the effectiveness of a detached breakwater against tsunami are performed.

In Chapter 3, the armor stability against overtopping jets caused by tsunami with rapid water level rise is examined. Hydraulic model experiments are conducted to examine the appropriate shapes of armor units against the initial impact of the impingement of water jets. Then a numerical analysis is performed. The stability of the armor blocks is predicted by computing the fluid force acting on each block.

In Chapter 4, the armor stability against steady overflow of tsunami is investigated. Hydraulic model experiments with a wide range of conditions are conducted to clarify the key factors for armor stability. A numerical computation method for the reproduction of the harbor-side flow field is then developed. The failure mechanism of

the armor units is examined by numerical analysis.

Chapter 5 presents a practical design method for armor units against tsunami overflow. Firstly, the applicability of the Isbash formula, the conventional method based on flow velocity is examined. Then a more practical design method for armor units based on overflow depth is proposed. The empirical formulae are derived reflecting the findings obtained by the experiments and numerical analysis. The validity of the method is confirmed by comparing the experimental results.

Chapter 6 presents an economical construction method for artificial reefs in the deep sea. Firstly, a numerical analysis method for fish reef blocks falling through water is investigated. A fish reef block for snow crabs which falls with stable behavior is then developed through laboratory experiments and numerical analysis. The mechanism that stabilizes the falling behavior is discussed based on the numerical results. The distribution of the placement position is investigated by stochastic model. Also, a quick estimation method for the placement position is developed to determine the release point of the block in the presence of an ambient current during actual installation.

Chapter 7 summarizes the thesis and presents some conclusions and suggestions for future work.

References

Coastal Development Institute of Technology (2001) : Research and development of numerical wave flume (CADMAS-SURF), CDIT Library, No. 12, 296p (*in Japanese*).

Coastal Engineering Research Center (1977) : Shore Protection Manual, U.S.Army Corps of Engrs., U.S.Govt. Printing Office, Vol. II, 7_213-7_216.

Fisheries Agency of Japan, Construction Division (2007) : Document for explanation to the prefectures on budget requests for FY2008, October 2 2007, http://www.jfa.maff.go.jp/j/gyoko_gyozyo/g_thema/pdf/sub3954.pdf (*in Japanese*), (accessed 2014-12-21).

Higuera, P., Lara, J.L., Losada, I.J. (2013) : Simulating coastal engineering process with OpenFOAM®, *Coastal Engineering*, **71**, 119-134.

Jacobsen, N.G., Fuhrman, D.R., Fredsoe, J. (2012) : A wave generation toolbox for the open-source CFD library : OpenFoam®, *International Journal for Numerical Methods in Fluids 2012*, **70**, 1073-1088.

Ministry of Land, Infrastructure, Transport and Tourism of Japan, Ports and Harb ours Bureau (2013) : Guidelines for Tsunami-Resistant Design of Breakwaters, September 2013, http://www.mlit.go.jp/common/001012142.pdf (*in Japanese*), (accessed 2014-12-18).

Nakamura, T., Oka, S., Yamamoto, R., Yanase, T., Asakawa, N., Nakagawa, Y. (2008) : The political meaning and the technical issues on development of offshore artificial fishing grounds, *Fisheries Engineering*, **45** (1), 67-74 (*in Japanese*).

OpenFOAM, http://www.openfoam.com/

Chapter 2

Development and Validation of a Versatile Numerical Wave Flume Using an Unstructured Grid

2.1 Introduction

Design of marine structures has been carried out based on hydraulic model experiments and design formula up to now. Meanwhile, the computational fluid dynamics approach has also become a powerful tool due to the advances in numerical analysis technology and improvement in the performance of computers. For example, a numerical wave flume based on the volume of fluid (VOF) method, named CADMAS-SURF (Coastal Development Institute of Technology, 2001) has been developed and applied to various problems such as wave forces acting on breakwaters and wave overtopping of seawalls (e.g., Nakano et al., 2002; Arimitsu et al., 2007; Kotake et al., 2007; Kawasaki et al., 2008; Matsumoto, 2009). As for studies dealing with concrete blocks, there are several studies which investigate the stability of concrete blocks by computing the flow velocity and pressure field around the blocks (e.g., Okuma et al., 2003; Arimitsu et al., 2008; Kondou et al., 2009; Matsumoto et al., 2011). However, the block shapes were not reproduced in these studies.

On the other hand, the stability of a concrete block depends on its shape. It is reported that flat-type armor blocks with large holes have higher stability due to the reduction of uplift forces acting on the blocks (Hamaguchi et al., 2007; Kubota et al., 2008). To deal with the influence of the block shape directly, it is necessary to set the grid size very small so that the block shape is reproduced. The numerical models based on a structured grid as CADMAS-SURF are not realistic in terms of computation time because the number of computational grids is enormous.

In contrast, models based on an unstructured grid enable the computation time to be largely reduced since it is possible to locally subdivide the computational grid. An

OpenFOAM CFD model is one numerical model which is based on an unstructured grid, and is now being applied to the field of the coastal engineering (e.g., Jacobsen et al., 2012; Higuera et al., 2013). The OpenFOAM is able to manage a wide range of problems since it has features such as dynamic mesh functionality, a flexible boundary condition, and easy code customisation. To apply this model as a numerical wave flume, however, it is indispensable to validate various items such as wave generation, wave propagation and deformation, wave breaking, wave force on structures, and modeling of porous structures.

In this Chapter, a versatile numerical wave flume is developed by using an OpenFOAM model and it is validated. Firstly, governing equations of the VOF model are outlined. The validation of the water surface profile and wave forces acting on a structure are confirmed through the dam-break tests. A wave generation method by reproducing a wavemaker is then presented. The validation of wave progression and deformation process is examined. As for the modeling of porous structures, analysis on the wave transmission of a sloping breakwater and the effectiveness of a detached breakwater against tsunami are performed.

2.2 Governing Equations

This study mainly uses the InterFOAM VOF model within the OpenFOAM which deals with a flow with a free surface by solving for both air and water. The governing equations are incompressible Navier-Stokes equation, the continuity equation, and the transport equation of VOF function as shown below:

$$\frac{\partial \rho \mathbf{U}}{\partial t} + \nabla \bullet \left(\rho \mathbf{U}\mathbf{U} \right) = -\nabla p + \nabla \bullet \mathbf{T} + \rho \mathbf{g} + \sigma \kappa \nabla F \,, \tag{2.1}$$

$$\nabla \bullet \mathbf{U} = 0 \,, \tag{2.2}$$

$$\frac{\partial F}{\partial t} + \nabla \bullet \left(\mathbf{U}F \right) + \nabla \bullet \left(\mathbf{U}_r F \left(1 - F \right) \right) = 0 \,, \tag{2.3}$$

where, ρ is the density of the fluid, $\mathbf{U}$ is the velocity vector, p is the pressure, $\boldsymbol{\tau}$ is the viscosity stress tensor, $\mathbf{g}$ is the gravitational acceleration vector, σ is the surface tension coefficient, κ is the curvature of the interface, F is the VOF function, $\mathbf{U}_r$ is the vector in the normal direction of the interface. The left side third term in Eq. (2.3) was introduced to suppress the numerical diffusion of the VOF function. For the details, see Rusche (2002). The right side fourth term in Eq. (2.1) represents the surface tension by means

of the continuum surface force model by Brackbill (1992). The density of fluid ρ and the viscosity coefficient of fluid μ are used as the values averaged for each cell as shown below:

$$\rho = F\rho_{water} + (1-F)\rho_{air}, \tag{2.4}$$

$$\mu = F\mu_{water} + (1-F)\mu_{air}. \tag{2.5}$$

2.3 Validation of the Free Surface Capturing Method

Dam break tests are generally used as benchmark tests for validation of the numerical analysis method on the flow field with free surface. A bore is generated and it propagates on a horizontal bottom by opening a gate separating a channel from the state that water is pooled in one side of the channel. Here, reproduction calculations of past studies which treated dam break tests are performed and the water surface profile and the pressure on a structure are verified.

2.3.1 2-D Dam Break Test for Validation of Water Surface Profile

The validity of this numerical model was confirmed by reproducing the 2 dimensional dam break test performed by Janosi et al. (2004). Fig. 2.1 shows the experimental setup. The length of a water column x_0 was 38 cm, channel length x_1 was 955 cm. Experiments were conducted by changing the initial height of the water column d_0 and the initial water depth in the channel d. A bore was generated by opening a gate at the speed 1.5 m/s, and the propagation of the bore was observed. Here, the initial height of the water column d_0 = 15 cm, and the initial water depth in the channel d = 1.5 cm were selected as the target case.

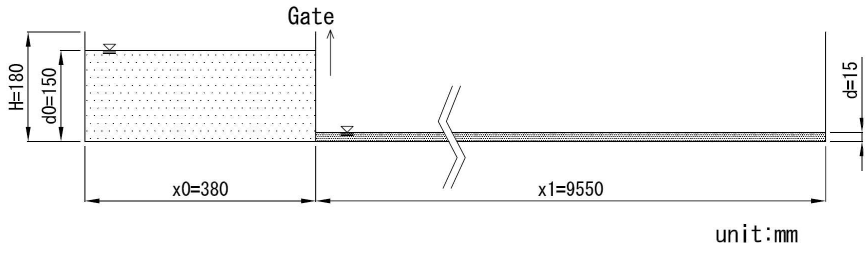

Figure 2.1 : Experimental setup for 2-D dam break test.

Table 2.1 shows the dimensions of the computational domain. It is the same as in the experiment except for the channel length x_1. It was shortened in the numerical analysis without influencing the result to reduce the computation time. Computation conditions and physical properties are summarized in Table 2.2. To reproduce the situation where the gate is pulled up at the speed of 1.5 m/s, the space representing the gate was replaced stepwise by the fluid cells from the bottom every 0.01 seconds as shown in Fig. 2.2.

Table 2.1 : Dimensions of the computational domain.

Parameter	Value
H (m)	0.18
d_0 (m)	0.15
d (m)	0.015
x_0 (m)	0.38
x_1 (m)	1.6175

Table 2.2 : Computation conditions for 2-D dam break test.

Parameter	Value
Grid size	$\Delta x = \Delta z = 2.5$ mm
Number of the cells	$Nx = 800$, $Nz = 72$, Total number of the cells ≈ 57,600
Time increment Δt	Automatic control (Maximum Courant number = 0.25)
Discrete scheme of the transport term	TVD scheme of second-order accuracy
Boundary conditions	Bottom-side, offshore-side, and onshore-side : No-slip Upper-side : Free inlet/outlet with atmospheric pressure
Turbulence model	RNG k-ε model
Physical properties	Density of water : 1.0×10^3 kg/m^3 Kinematic viscosity of water : 1.0×10^{-6} m^2/s
Way of gate opening	Stepwise opened so that the average speed is 1.5 m/s (see Fig. 2.2)

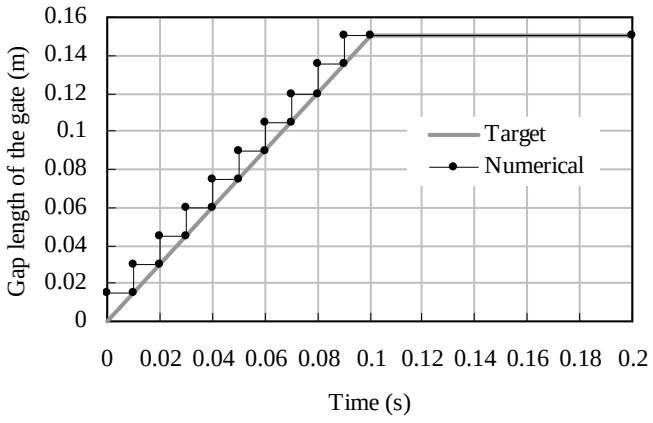

Figure 2.2 : Way of gate opening.

Fig. 2.3 shows a comparison of the water surface profiles obtained by experiment and numerical computation. The numerical result reproduces the characteristics that (1) the wave breaks to the back side (gate-side) immediately after the opening of the gate, (2) the wave then breaks to the front side, and (3) the impinged water jumps up and impinges again. However, the water surface profile in numerical result progresses slightly earlier than that in the experiment.

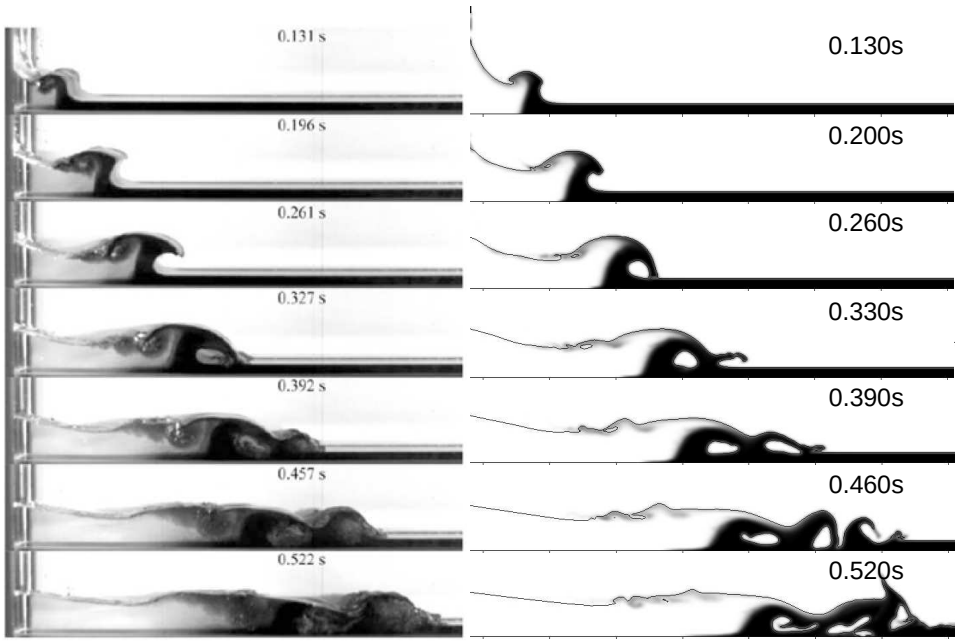

Figure 2.3 : Comparison of water surface profiles. (Left) : Experiment (Janosi et al., 2004). (Right) : Numerical result.

2.3.2 3-D Dam Break Test for Validation of Hydrodynamic Pressure Acting on a Structure

Reproduction of the 3 dimensional dam break test performed by Kleefsman et al. (2005) was conducted. In this test, the water surface profile and the pressure acting on a rectangle structure when a bore impacts to the structure were compared. Fig. 2.4 shows the experimental setup. The flume was 1.0 m in height and 3.22 m in length. A rectangle structure of 0.40 m in width, 0.16 m in length, and 0.16 m in height was fixed on the bottom. The column of water was 1.228 m in length and 0.55 m in height. The gate separating the water column was instantly opened in the computation.

The computation conditions and physical properties are shown in Table 2.3. The measurement position of pressure and water level are shown in Table 2.4.

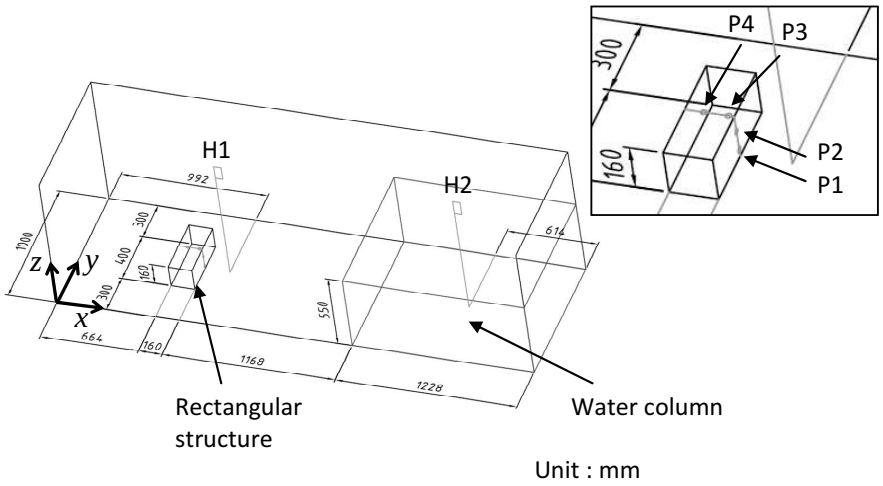

Figure 2.4 : Experimental setup for 3-D dam break test.

Table 2.3 : Computation conditions for 3-D dam break test.

Parameter	Value
Computational domain	Height : 1.0 m, Width : 1.0 m, Length : 3.22 m
Grid size Δx	8.0 mm (0 m < x < 1.992 m), 12.28 mm (1.992 m < x < 3.22 m)
Grid size Δy	20.0 mm
Grid size Δz	5.0 mm (0 m < z < 0.55 m), 10.0 mm (0.55 m < z < 1.0 m)
Number of the cells	Nx = 349, Ny = 50, Nz = 116 Total number of the cells ≈ 2,024,200
Time increment Δt	Automatic control (Maximum Courant number = 0.25)
Discrete scheme of the transport term	TVD scheme of second-order accuracy
Boundary conditions	Bottom-side, offshore-side, and onshore-side : No-slip Upper-side : Free inlet/outlet with atmospheric pressure
Turbulence model	RNG k-ε model
Physical properties	Density of water : 1.0×10^{3} kg/m^{3} Kinematic viscosity of water : 1.0×10^{-6} m^{2}/s
Way of gate opening	Instantly opened at time t = 0 s
Measurement items	Pressure and water surface elevation (see Table 2.4)

Table 2.4 : Measurement positions for the pressure and water level.

(a) Pressure

	x (m)	y (m)	z (m)
P1	0.824	0.5	0.025
P2	0.824	0.5	0.099
P3	0.806	0.5	0.160
P4	0.726	0.5	0.160

(b) Water surface elevation

	x (m)	y (m)
H1	0.992	0.5
H2	2.606	0.5

Fig. 2.5 shows a comparison of the water surface profiles. The numerical result reasonably reproduces the experimental situation that the water splashes when it

impacts on the structure.

Fig. 2.6 shows a comparison of the time series of water surface elevation measured at *H1* (ahead of the structure) and *H2* (in the center of the water column). The water level at *H2* decreases by the opening of the gate until the time t = 2.5 s. Numerical result reproduces it well. Then the water level rises twice at the time t = 3.0 s and t = 3.8 s due to the reflected wave and the re-reflected wave. The numerical result underestimates the re-reflected wave at the time t = 3.8 s. As for *H1*, numerical result overestimates the water level rising when the reflected wave gets over the structure. However, the overall trend of the water surface elevation is reproduced well.

Fig. 2.7 shows a comparison of the time series of the pressure acting on the structure. When the bore impacts on the structure, the impact pressure is generated at *P1* (lower side of the front face) and *P2* (upper side of the front face). The maximum pressure at *P1* is about 12,000 Pa in the experiment, while the computed value is about 13,000 Pa. As for *P2*, the experimental value is about 7,500 Pa, while the computed value is about 6,400 Pa. The pressures at *P3* and *P4* which are on the upper face of the structure show the maximum value when the reflected bore gets over the structure at the time t = 2.0 s. There are subtle differences in the pressures around the time t = 2.0 s between experimental and numerical results. However, the overall trend of the time series of the pressure is also well reproduced in the numerical computation.

From the above results, the validation of the free surface capturing method of this numerical model was confirmed.

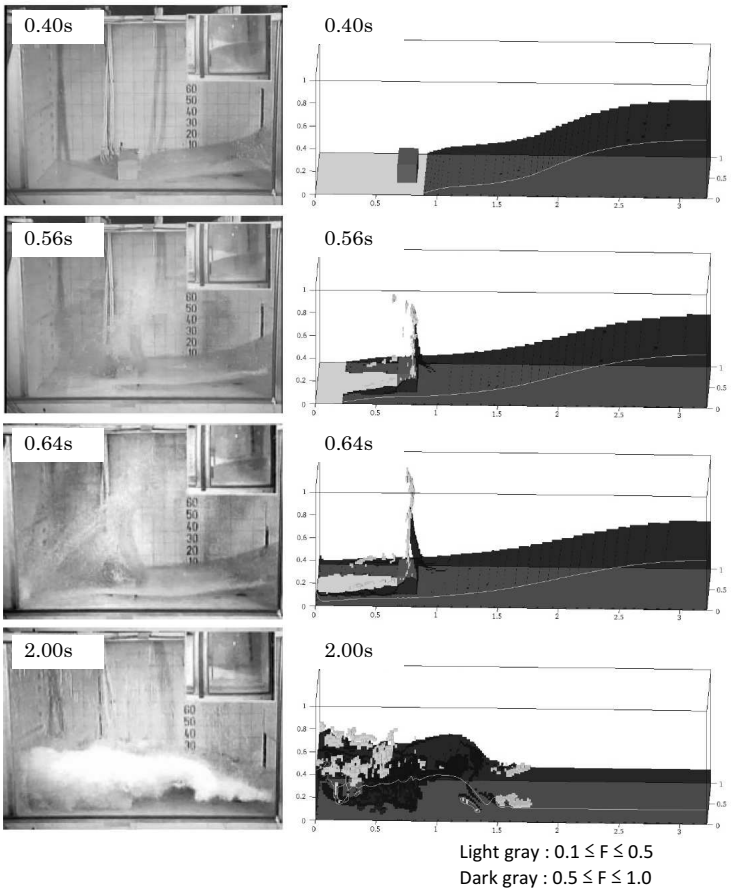

Figure 2.5 : Comparison of water surface profiles. (Left) : Experiment (Kleefsman et al., 2005). (Right) : Numerical result.

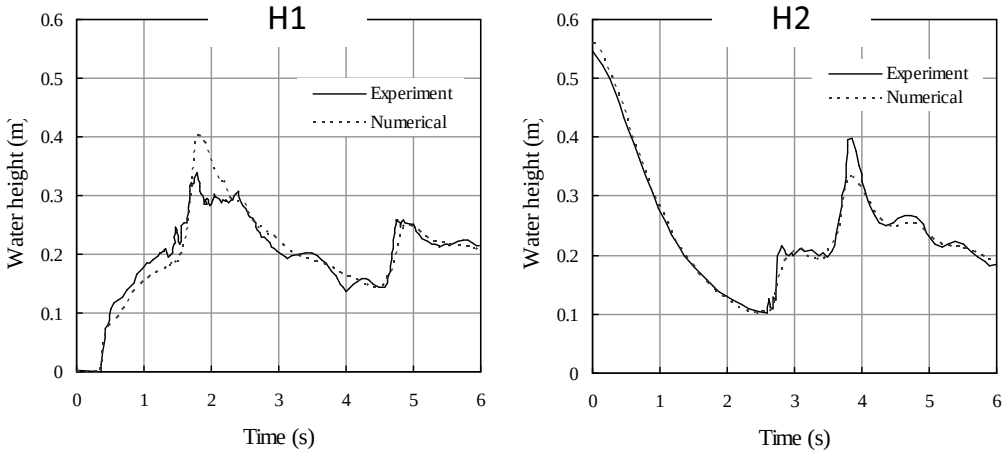

Figure 2.6 : Comparison of time series of water surface elevation.

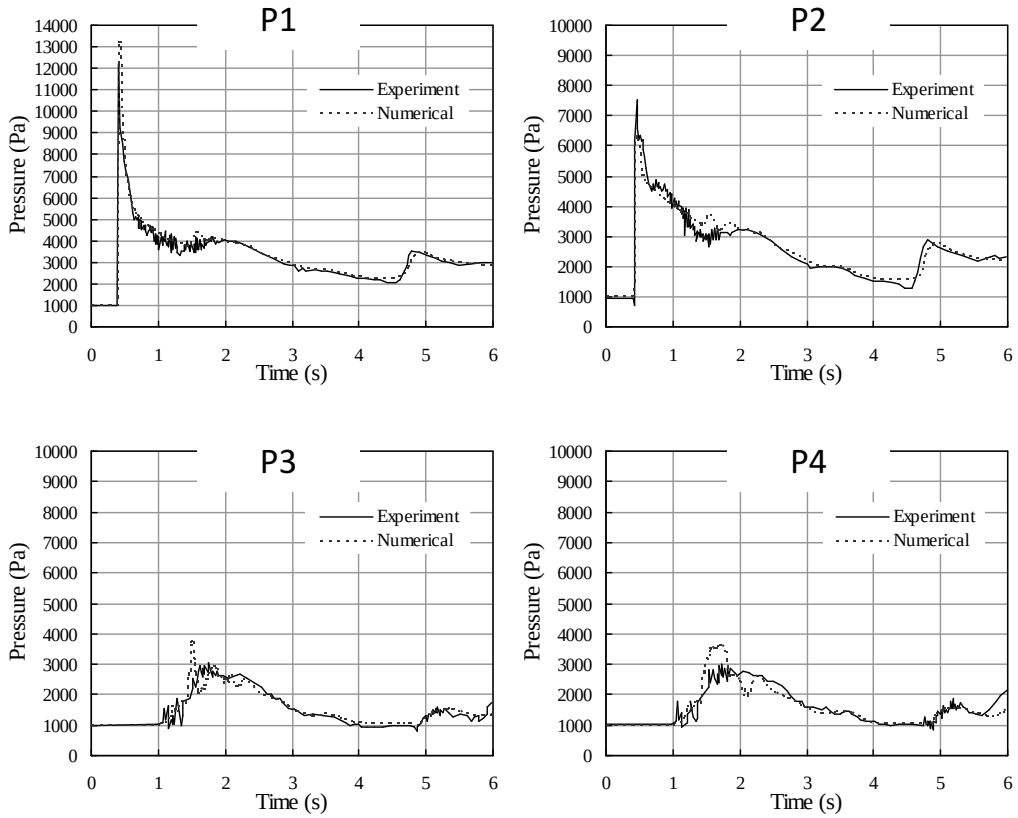

Figure 2.7 : Comparison of time series of pressure on the front and top surface of the rectangular structure.

2.4 Numerical Analysis of Wave Generation by Reproducing Motion of Wavemaker

The general methods for generating waves in the numerical wave flume include the following:

(1) A method to control the flow velocity and the water level at one end of the computational domain (wave-making boundary).
(2) A method to control the volume flux density of a vertical source distribution inside the computational domain (wave-making source).
(3) A method to control the vertically oscillating flow at the bottom of the wave flume.
(4) A method to control the wavemaker.

The first method is the simplest and easiest way to generate waves, but it is not suitable for long-time simulation because the computation sometimes becomes unstable

or re-reflected waves are generated when reflected waves reach the wave-making boundary.

The second method is proposed by Brorsen and Larsen (1987), which enables wave generation without re-reflection by combining with an energy dissipation zone. Since this method sometimes causes a problem in that the total volume of water in the computational domain gradually changes in the case of long-time simulation, the countermeasures are examined (e.g., Fujiwara et al., 2008).

The third method also enables wave generation without re-reflection. This method has been examined to avoid the re-reflection in the actual wave flume by Goda and Kikuya (1964) and Ohyama et al. (1997). The issue of this method is that the efficiency of wave generation is low in the case of generating deep-water waves.

The fourth method is mainly used in the numerical wave flumes based on the particle method (e.g., Gomez-Gasteira et al., 2005). There seem to be no studies which applied this method in the numerical wave flume based on the VOF method so far. This method has an advantage that direct comparison with experiment becomes possible. Thus, the physical phenomena observed in the experimental wave flumes can be analyzed in detail. Also, the total volume of water in the computational domain is generally preserved in this method.

In this study, a method to control the wavemaker is adopted into the numerical wave flume based on the VOF method. Fundamental validations on the wave generation and wave propagation are performed. In addition, application to a wave generation by using a flap-piston combined wavemaker is conducted.

2.4.1 Numerical Analysis Method

Numerical analysis on wave generation using wavemaker is conducted by applying the moving grid functionality included in the OpenFOAM model. Fig. 2.8 shows the schematic diagram of the computational method. A wall boundary corresponding to the wavemaker is moved at a prescribed speed and the computational grid around the wavemaker is also moved and deformed accordingly.

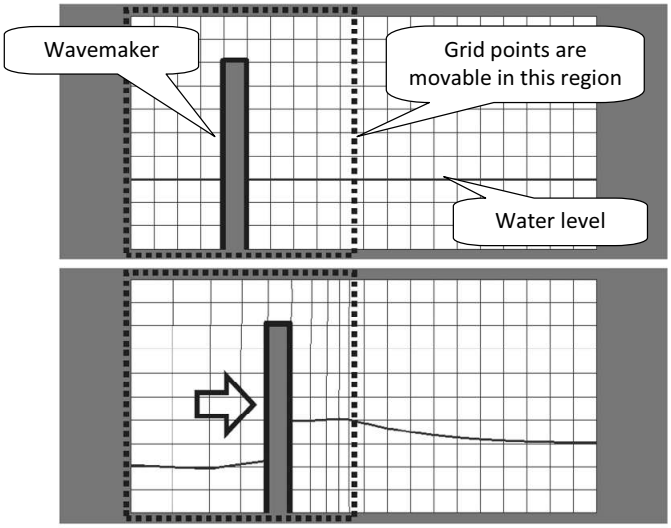

Figure 2.8 : Schematic diagram of the wave generation using wavemaker.

To move the boundary without destroying the computational grid, it is necessary that the grid points be moved smoothly along the motion of the moving boundary. The moving velocity of each grid point **u** is determined by solving the following Laplace equation:

$$\nabla \bullet \left(\gamma \nabla \mathbf{u} \right) = 0 , \tag{2.6}$$

where, γ is the diffusion coefficient. The moving velocity of the boundaries are given as the boundary conditions. The position of the grid point in the next time step is obtained by the following equation:

$$\mathbf{x}_{new} = \mathbf{x}_{old} + \mathbf{u}\Delta t , \tag{2.7}$$

where, $\mathbf{x}_{old}$, $\mathbf{x}_{new}$ are the grid points before and after the movement. Since the diffusion coefficient can be arbitrary set, it is possible to control the moving of the grid so as to keep the quality of the grid. The flux due to the movement of the grid is considered in the governing equations. Details of this method are mentioned in Jasak and Tukovic (2007).

2.4.2 Validation of Wave-making Function and Wave Propagation and Deformation on a Slope

A numerical computation was conducted to validate the wave generation method using a wavemaker and a wave propagation and deformation process. Regular waves and irregular waves are generated and they propagate on a slope. In the regular wave test,

spatial distribution of the wave height is obtained to validate the wave shoaling process and the wave breaking limit. In the irregular wave test, the frequency spectrum and wave statistics are obtained to confirm that the target waves are properly generated. In addition, the processes of wave shoaling and wave breaking are validated.

Fig. 2.9 shows the schematic layout of the wave flume. A piston-type wavemaker is located at x = 0 m. A uniform slope of 1/30 is installed between x = 5.0 m and x = 14.0 m. The onshore side from x = 14 m is a horizontal bed. The water depth at the wavemaker is set to 50 cm. Energy dissipation zones from Cruz et al. (1993) are placed both ends of the flume. The water surface elevation is measured at the 18 locations.

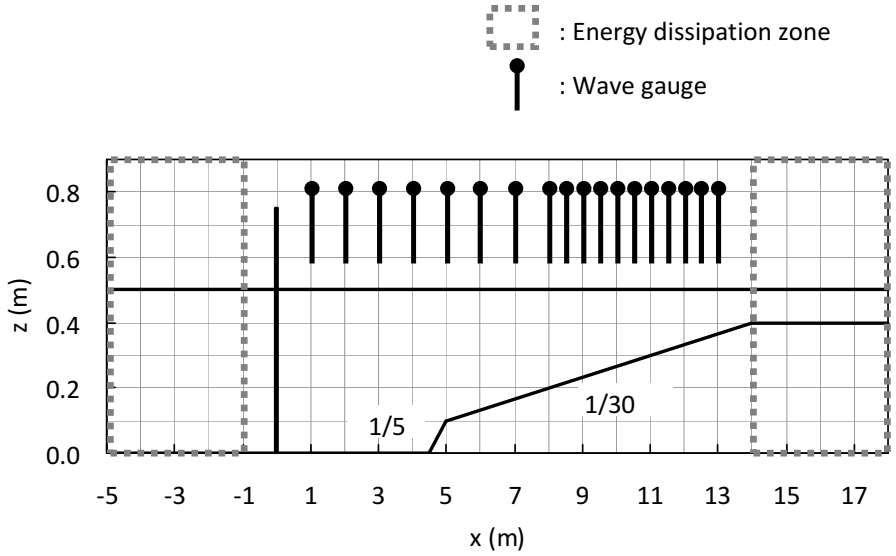

Figure 2.9 : Schematic layout of the wave flume.

The target wave conditions at the offshore are shown in Table 2.5. In the regular wave test, the target wave period is T = 1.5 s and the target wave heights are H = 6 cm, 10 cm, and 14 cm. In the irregular test, the Modified Bretschneider-Mitsuyasu spectrum with wave period $T_{1/3}$ = 1.5 s and wave height $H_{1/3}$ = 6 cm, 10 cm, and 14 cm are targeted. The signals for driving the wavemaker in the irregular wave test were obtained by combining the sinusoidal waves. First, the target spectrum of the wave was converted to the spectrum of the paddle motion by means of the transfer function. The frequency components are determined by equally dividing the frequency range of 0.25 – 4.0 Hz into 500 components. The phase of each component was determined by using a random number.

Table 2.5 : Target wave conditions at the offshore.

	Regular wave	Irregular wave
Spectrum	-	Modified Bretschneider-Mitsuyasu
Wave period	T = 1.5 s	$T_{1/3}$ = 1.5 s
Wave height	H = 6, 10, 14 cm	$H_{1/3}$ = 6, 10, 14 cm

In the computation, the water surface elevation was measured at intervals of 0.1 s. In the regular wave test, the wave height was obtained as the average value of 5 waves. The 6th wave from the beginning of wave generation and the following four waves were used since their wave heights were almost constant. In the irregular wave test, the frequency spectrum and the wave statistics were analyzed using a time series of water surface elevation. The data for 204.8 seconds from the time t = 90 s were used.

To examine the influence of the computational grid, the 3 kinds of grids shown in Table 2.6 were used. The grid size of Grid 1 is $\Delta x = \Delta z$ = 2 cm, and that of Grid 2 is Δx = 2 cm, Δz = 1 cm. Grid 3 is made by subdividing Grid 2 around the still-water level into $\Delta x = \Delta z$ = 1 cm. Table 2.7 shows the computation conditions and physical properties.

Table 2.6 : Computational grid.

	Grid size	Number of the cells
Grid 1	Δx = 2 cm, Δz = 2 cm	42,027
Grid 2	Δx = 2 cm, Δz = 1 cm	84,065
Grid 3	z = 0.4～0.7 m : Δx = 1 cm, Δz = 1 cm Otherwise : Δx = 1 cm, Δz = 2 cm	118,535

Table 2.7 : Computation conditions.

Parameters	Values
Time increment Δt	Automatic control (Maximum Courant number is 0.25)
Discrete scheme of transport term	TVD scheme of second-order accuracy
Boundary conditions	Bottom-side, offshore-side, and onshore-side : No-slip Upper-side : Free inlet/outlet with atmospheric pressure
Turbulence model	RNG k-ε model
Physical properties	Density of water : 1.0×10^{3} kg/m^{3} Kinematic viscosity of water : 1.0×10^{-6} m^{2}/s

The result of the regular wave test is shown below. Fig. 2.10 shows the spatial distribution of the wave height. The wave height distribution was calculated by using the nonlinear shoaling coefficient by Shuto (1974) and the breaking limit was calculated by using the breaker index by Goda (2010), both are also shown in the figure. The breaker index by Goda (2010) is expressed as follows:

$$\frac{H_b}{h_b}=\frac{A}{h_b/L_0}\left\{1-\exp\left[-1.5\frac{\pi h_b}{L_0}\left(1+11\tan^{4/3}\theta\right)\right]\right\} \quad : \quad A=0.17\,, \tag{2.8}$$

where, H_b is the limiting breaker height, h_b is the water depth, L_0 is the wave length in deep water, and θ is the bottom slope. In Grid 1 which is the coarsest grid, the numerical result favorably reproduces the situation that wave height becomes larger by shoaling as it propagates through the slope. The position of the wave breaking almost agrees with that from Goda (2010). In Grid 2, which is made by subdividing Grid 1 into half in the vertical direction, the wave distribution is in good agreement with the theory in the case of H = 6 cm which is a non-breaking wave. However, the timing of the wave breaking obviously earlier in the cases of H = 10 cm and 14 cm. Jacobsen et al. (2012) pointed out that the large aspect ratio of the grid causes a quickening of the wave breaking in the computation using the VOF method within the OpenFOAM model. This result shows the same tendency. The result of Grid 3 whose aspect ratio around the still-water level is 1:1 is slightly better than that of Grid 1.

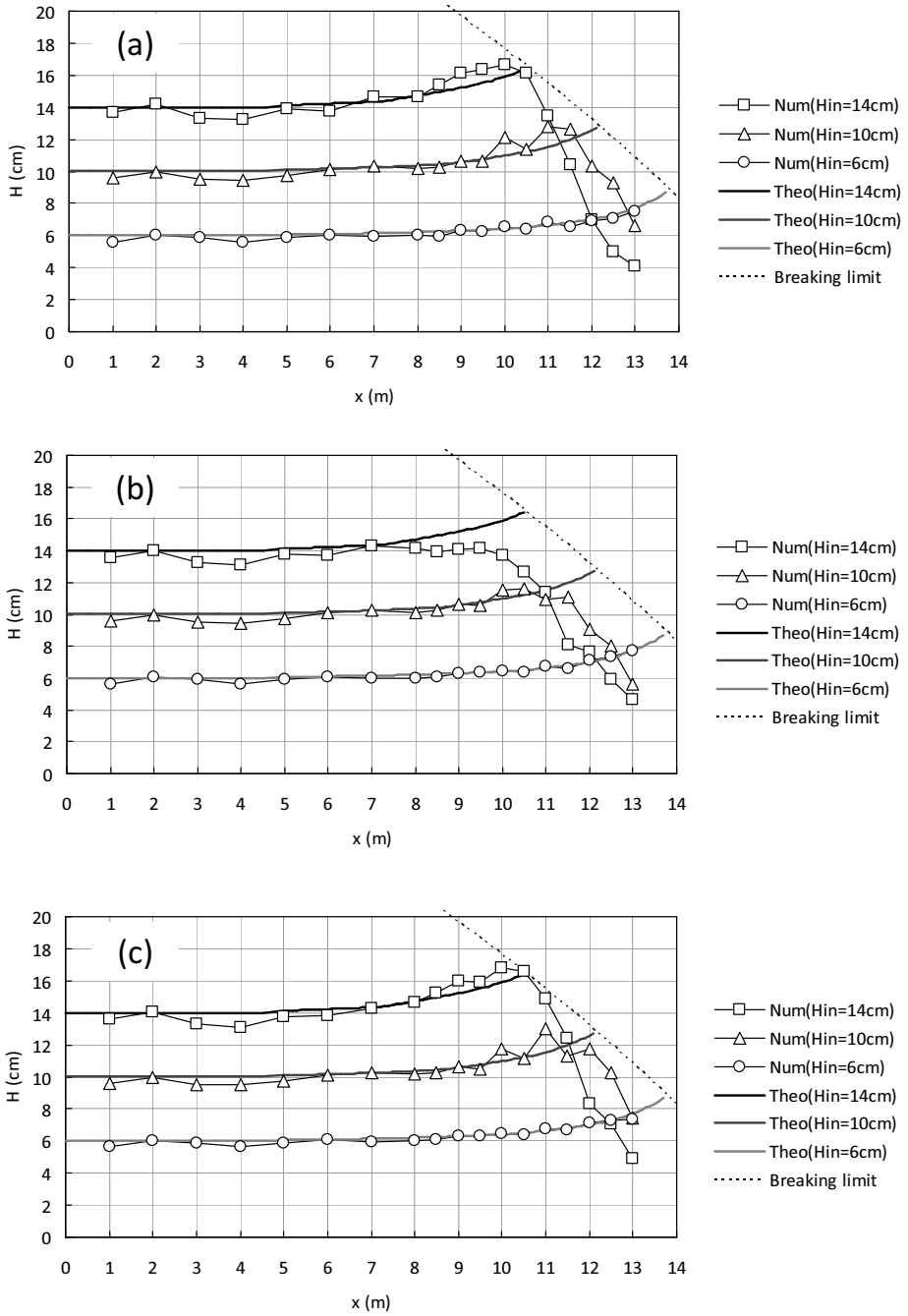

Figure 2.10 : Spatial distribution of wave height of regular wave. (a) : Grid 1, (b) : Grid2, (c) : Grid 3. “Theo” is the wave height calculated using the shoaling coefficient by Shuto (1974). “Breaking limit” is the wave height of the breaking limit by Goda (2010).

The result of the irregular wave test is shown below. In the irregular wave test, Grid 1 and Grid 2 were used. Fig. 2.11 shows the frequency spectrum in front of the wavemaker (x = 1.0 m). All numerical results agreed favorably with the target spectrum.

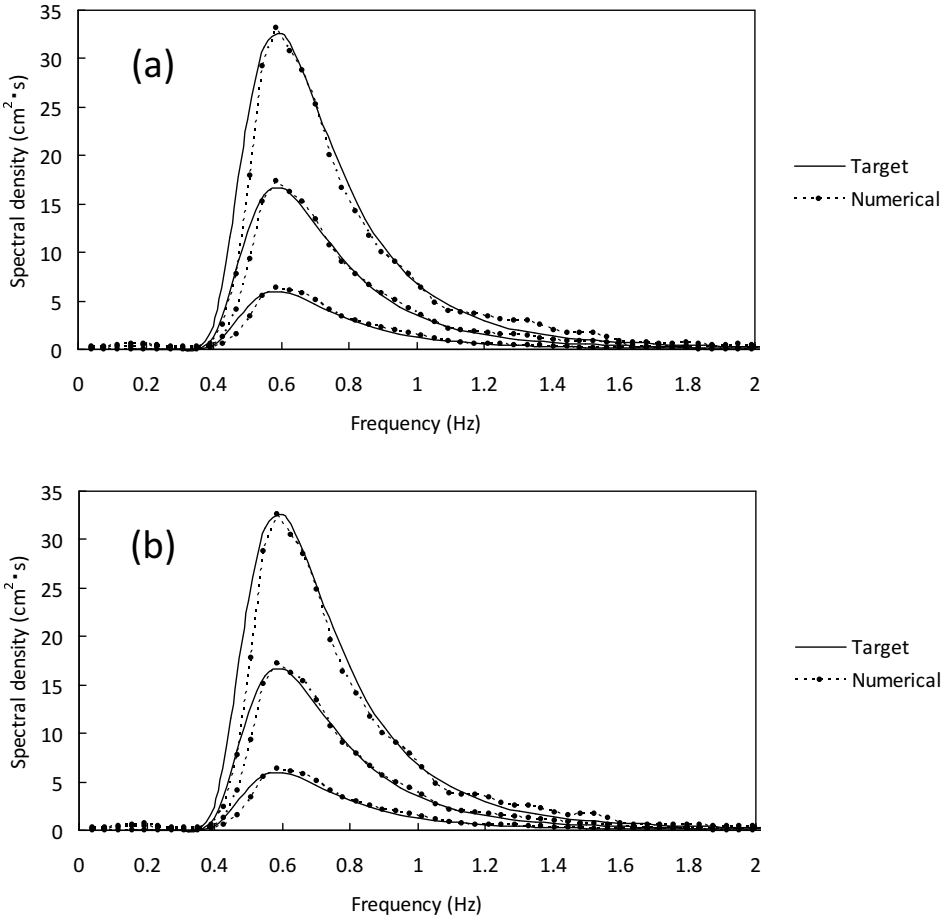

Figure 2.11 : Frequency spectrum of irregular wave. (a) : Grid 1, (b) : Grid 2.

Fig. 2.12 shows the spatial distribution of the significant wave height. The wave distribution calculated by means of the Goda's irregular wave model (Goda, 1975) is also shown in the figure. The result of Grid 1 reproduces the Goda's model acceptably well. However, in the cases of $H_{1/3}$ = 10 cm and 14 cm, the numerical result tends to underestimate the wave height by about 10% at the position where the wave breaking occurs. On the other hand, the numerical result agreed well with that by the Goda's model in the case of $H_{1/3}$ = 6 cm, where wave breaking does not occur. The results of Grid 2 are almost same as that of Grid 1, but the degree of underestimation of wave height is a little larger than that of Grid 1. This is the same as the trend that was seen in the regular wave test.

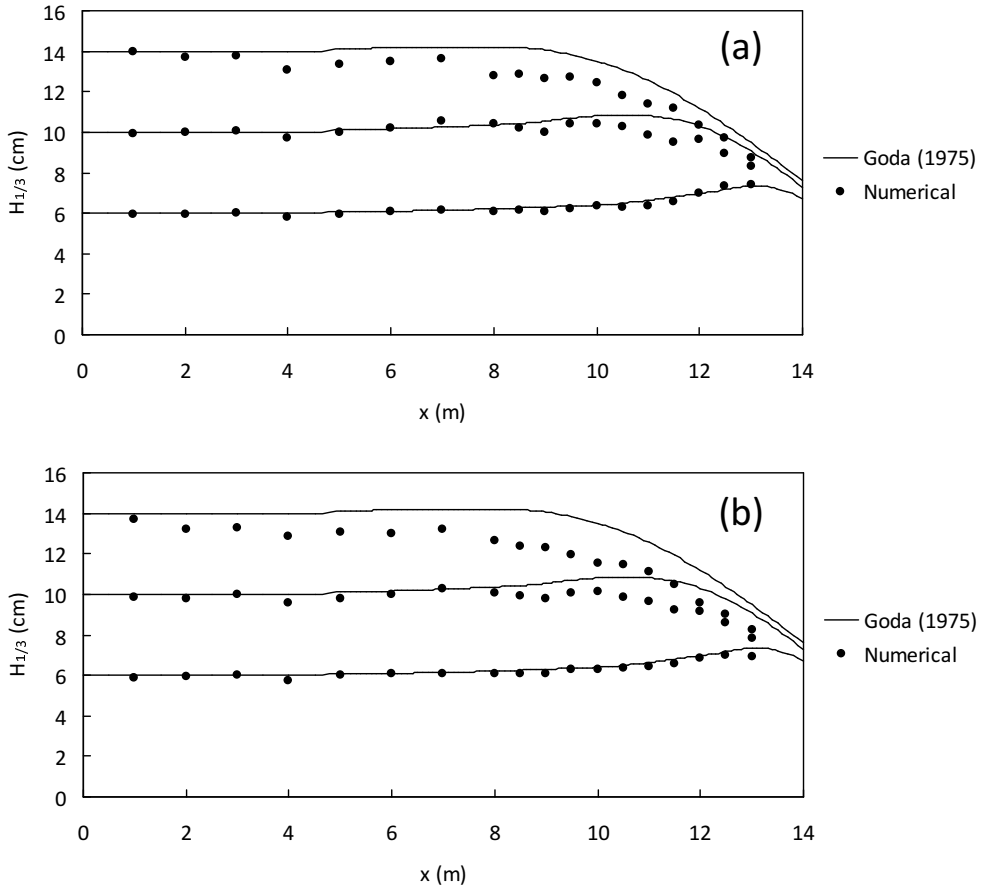

Figure 2.12 : Spatial distribution of wave height of irregular wave. (a) : Grid 1, (b) : Grid 2.

The time series of total volume of water in the computational domain is shown in Fig. 2.13. The time change rate of the total volume of water is largest in the case of $H_{1/3}$ = 14 cm. However, the change in the total volume in the computation time of 300 s (= 200 $T_{1/3}$) is less than 0.1%. Therefore, it was confirmed that the total volume of water is almost completely conserved.

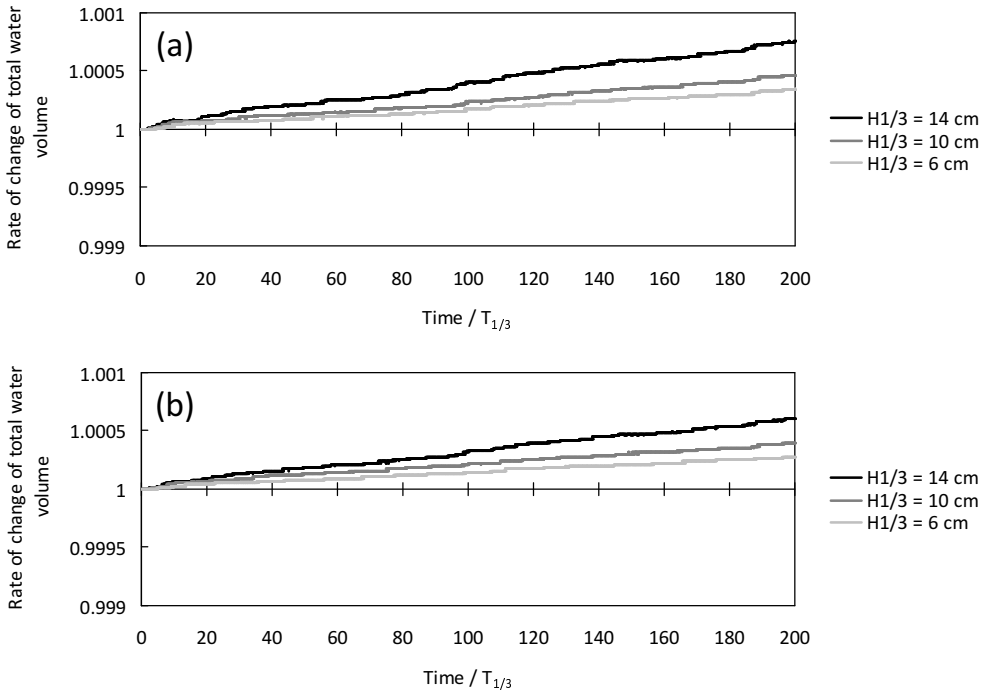

Figure 2.13 : Time series of total volume of water in the computational domain in the irregular wave test. (a) : Grid 1, (b) : Grid 2.

2.5 Modeling and Validation of Permeable Structures by Porous Model

Porous materials such as wave-dissipating concrete blocks and rubble mounds are frequently used in marine structures including breakwaters. Part of the wave energy is dissipated due to the complicated spaces formed by the blocks and stones. It is important to properly evaluate the effect of these porous structures in a numerical wave flume. However, reproducing the individual shape of the blocks and stones is impractical in terms of computation time. Accordingly, a porous model is used to reproduce these structures. In the following, numerical analysis on the wave transmission coefficient of a sloping breakwater and the effectiveness of a detached breakwater against tsunami are conducted to confirm the validity of the porous model by comparing with experimental results.

2.5.1 Numerical Analysis Method

In the porous model incorporated in the OpenFOAM, the hydraulic flow resistance in

the porous medium is expressed by a D-F relationship as shown below:

$$\mathbf{R} = -\left(\alpha \mathbf{U} + \beta |\mathbf{U}| \mathbf{U}\right), \tag{2.9}$$

where, **R** is the hydraulic flow resistance, **U** is the flow velocity, α is the laminar resistance coefficient, and β is the turbulent resistance coefficient. In this study, these coefficients were obtained by using the empirical formulae by Engelund (1953) as follows:

$$\alpha = \alpha_0 \frac{(1-n)^3}{n^2} \frac{\nu}{d^2}, \quad \beta = \beta_0 \frac{1-n}{n^3} \frac{1}{d}, \tag{2.10}$$

where, ν is the kinematic viscosity of water, d is the characteristic diameter of the porous material, n is the porosity, and α_0 and β_0 are the material constants.

The porous model originally incorporated in the OpenFOAM has a problem that it does not satisfy the mass conservation in the free surface flow with porous body as pointed out by Jansen et al. (2014). Thus, the code was modified to satisfy the mass conservation in reference to Jansen et al. (2014). The modified code was used in the following validation tests in this Chapter.

2.5.2 Validation of Wave Transmission Coefficient of a Sloping Breakwater

The validation of the porous model was examined by comparing the wave transmission coefficient of a sloping breakwater. Experiments were carried out using a 30 m long, 0.5 m wide and 1.0 m deep wave flume equipped with a piston type wavemaker. Fig. 2.14 shows the schematic layout of the wave flume. A breakwater was installed on a slope of 1/30. The water depth was 50 cm at the offshore-side horizontal bottom and 20 cm at the center of the breakwater.

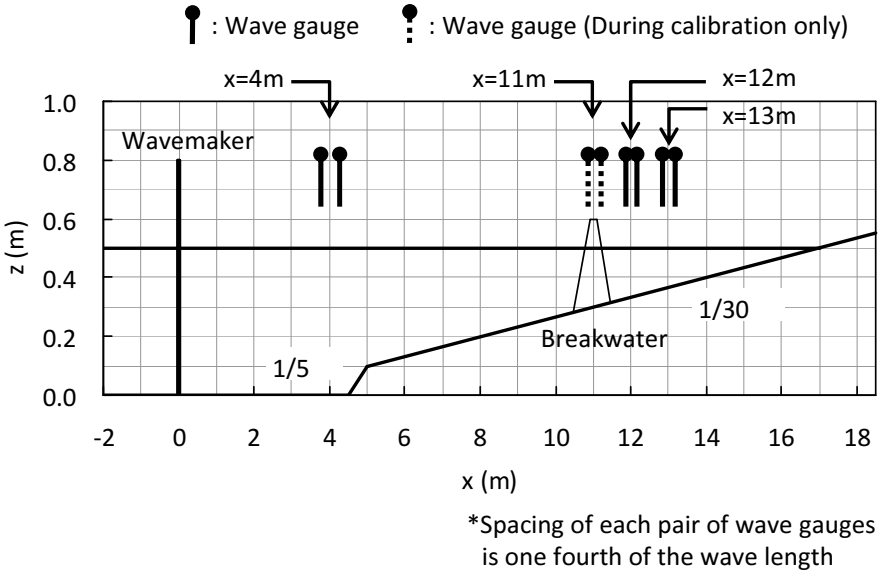

Figure 2.14 : Schematic layout of the wave flume.

The three shapes of breakwaters shown in Fig. 2.15 were used. Breakwater-A is a trapezoid shape with a crown width of 20 cm, a crown height of 10 cm, and a slope angle of 1:3/4. Breakwater-B is a trapezoid shape with a widened crown width of 30 cm. Breakwater-C is a rectangular shape with a crown width of 20 cm and a crown height of 15 cm.

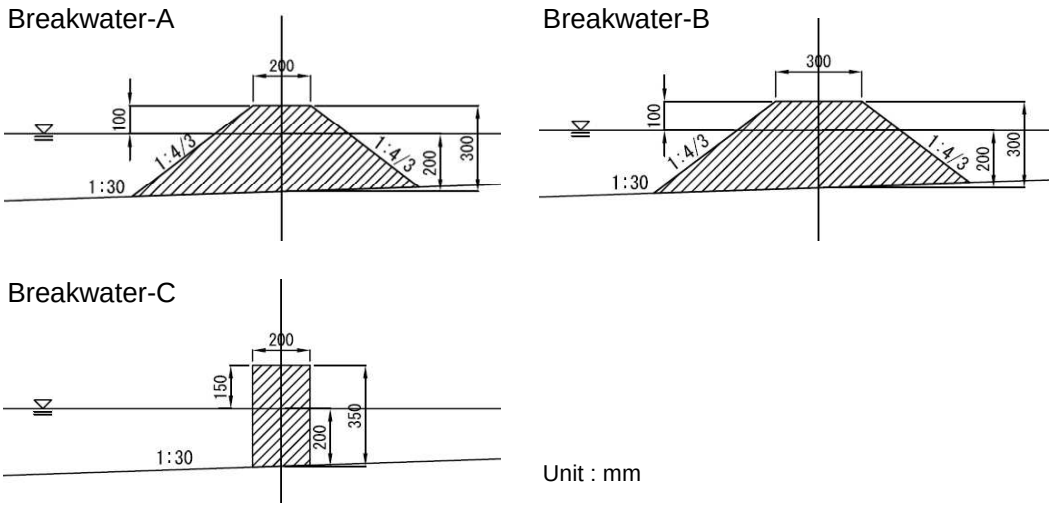

Figure 2.15 : Cross-section of the breakwaters.

Two different sizes of tetrapods (mass 118 g and 294 g) and stones (mass 8 g) were used as the component materials of the breakwaters. The specifications of these

materials are shown in Table 2.8.

Table 2.8 : Specifications of the component material of breakwaters.

	Tetrapods (Small)	Tetrapods (Large)	Stones
Mass	118 g	294 g	8.0 g
Volume	51.2 cm^3	128 cm^3	3.04 cm^3
Density	2.30 g/cm^3	2.30 g/cm^3	2.63 g/cm^3
Porosity	50%	50%	46%

Regular waves with two wave periods (T = 1.5 s and 2.0 s) and four wave heights (H = 3 cm, 5 cm, 7 cm, and 9 cm) were used. These conditions were set so that wave breaking and wave overtopping did not occur. Prior to installing the breakwater, the wave heights at the breakwater were calibrated. Two sets of two wave gauges were positioned on the offshore horizontal bottom (two gauges around x = 4.0 m) and at the center of the breakwater (two gauges around x = 11 m). The spacing of each pair of wave gauges was set to one fourth of the wave length L. The wave height and wave period were obtained as the average values of 5 waves. The 6th wave from the beginning of wave generation and the following four waves were used since their wave heights were almost constant. The incident wave height and wave period were obtained by averaging the wave heights and periods measured by the two wave gauges. A calibration curve which is the relationship between the wave heights at the offshore side and that at the position of the breakwater was obtained for each wave period. In the tests with a breakwater, the incident wave height at the breakwater was estimated from the offshore wave height using the calibration curve.

The breakwater was covered with wire mesh so that the blocks or stones did not move during wave action. The transmission waves were measured at the two locations behind the breakwater apart from the center of the breakwater with distances of 1.0 m and 2.0 m. Two wave gauges were positioned at each location with a spacing of one fourth of the wave length. The transmission wave height was obtained by averaging the incident wave heights measured at the two locations. The wave transmission coefficient K_T was obtained by the following equation:

$$K_T = \frac{H_T}{H_I}, \tag{2.11}$$

where, H_T is the transmission wave height and H_I is the incident wave height at the breakwater.

Tests were conducted by changing the shapes of the breakwater and the component materials as shown in Table 2.9.

Table 2.9 : Test cases.

Case	Component material	Shape of breakwater
Case 1	Tetrapods (Small)	Breakwater-A (Trapezoid)
Case 2	Tetrapods (Small)	Breakwater-B (Trapezoid)
Case 3	Tetrapods (Small)	Breakwater-C (Rectangle)
Case 4	Tetrapods (Large)	Breakwater-A (Trapezoid)
Case 5	Stones	Breakwater-A (Trapezoid)
Case 6	Stones	Breakwater-C (Rectangle)

Fig. 2.16 shows a schematic layout of the numerical wave flume. The computational domain is a 2 dimensional domain, 25 m in length and 0.8 m in height. Bathymetry and the water depth were the same conditions as in the hydraulic model experiment. Waves were generated by controlling the vertically oscillating flow at the bottom of the wave flume. An inlet of 1.0 m-long was provided on the offshore bottom. Waves were generated by giving a predetermined flow rate at this inlet. The flow rate was determined from the wave generating efficiency by Goda (1964). An energy dissipation zone was set at the offshore end of the flume to dissipate the reflected waves from the structure.

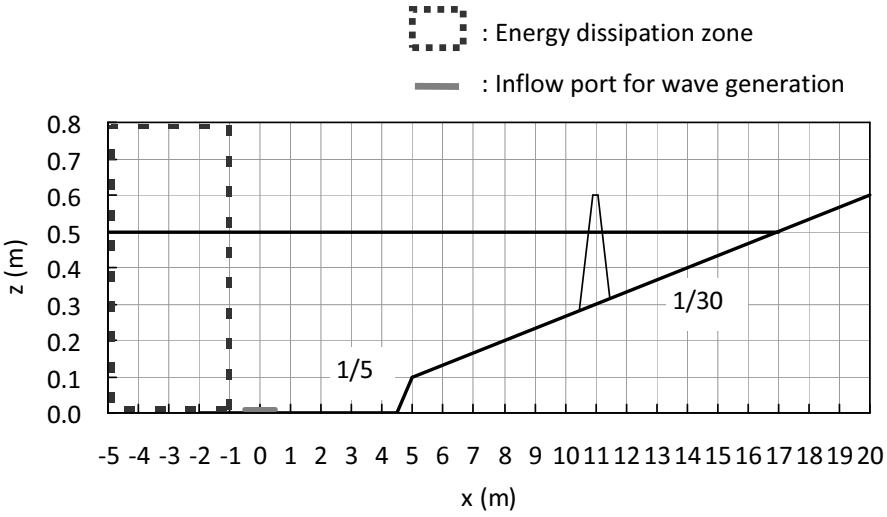

Figure 2.16 : Schematic layout of the numerical wave flume.

Table 2.10 shows the computation conditions and physical properties. Table 2.11 shows the specifications for the porous model. The material constants α_0 and β_0 were determined by referring to Kondo and Takeda (1983). Calibration of the wave height and measurement of the transmission coefficient were conducted in the same manner as in the experiment.

Table 2.10 : Computation conditions.

Parameter	Value
Grid size	Δx = 2 cm, Δz = 1 cm
Number of the cells	Nx = 1250, Nz = 90, Total number of cells ≈ 74,000
Time increment Δt	Automatic control (Maximum Courant number = 0.25)
Discrete scheme of the transport term	TVD scheme of second-order accuracy
Boundary conditions	Bottom-side, offshore-side, and onshore-side : No-slip Upper-side : Free inlet/outlet with atmospheric pressure
Turbulence model	RNG k-ε model
Physical properties	Density of water : 1.0×10^{3} kg/m^{3} Kinematic viscosity of water : 1.0×10^{-6} m^{2}/s

Table 2.11 : Specifications for the porous model.

	Tetrapods (Small)	Tetrapods (Large)	Stones
Characteristic diameter d	3.71 cm	5.04 cm	1.80 cm
Porosity n	50%	50%	46%
α_0	2100	2100	1500
β_0	2.2	2.2	3.6
Laminar resistance coefficient α	0.76	0.41	3.45
Turbulent resistance coefficient β	237.0	174.6	1111.0
Inertia coefficient C_M	1.2	1.2	1.2

A comparison of the wave transmission coefficients in the experiment and the computation is shown in Fig.2.17. Fig. 2.17(a) shows the results of the breakwater composed of tetrapods. The transmission coefficient K_T decreases as the wave steepness H/L increases. As for the influence of the width of the breakwater, the transmission coefficient in Case 2 of wider breakwater is smaller than that of Case 1 as a whole. As for the influence of the block size, the transmission coefficient in Case 4 of larger blocks is smaller than that of Case 1 as a whole. The transmission coefficient in Case 3 is the largest because the rectangle breakwater-C is the narrowest. Numerical results reproduce these trends favorably in the experiments. When compared in detail, the transmission coefficients in the numerical results are slightly smaller than those in the experiments. In addition, the degree of change in the transmission coefficients with respect to change in the wave steepness is larger in the numerical computation.

Fig. 2.17(b) shows the results of the breakwater composed of stones. As in the case of the tetrapods, the transmission coefficient decreases as the wave steepness increases. The transmission coefficient in Case 6 of the rectangle breakwater is larger than that in Case 5 of the trapezoidal breakwater. The transmission coefficients in the cases of stones are smaller than those of tetrapods. This is because that the stones have a smaller

diameter and smaller porosity than tetrapods. Numerical results agree well with the experimental ones in the cases of stones.

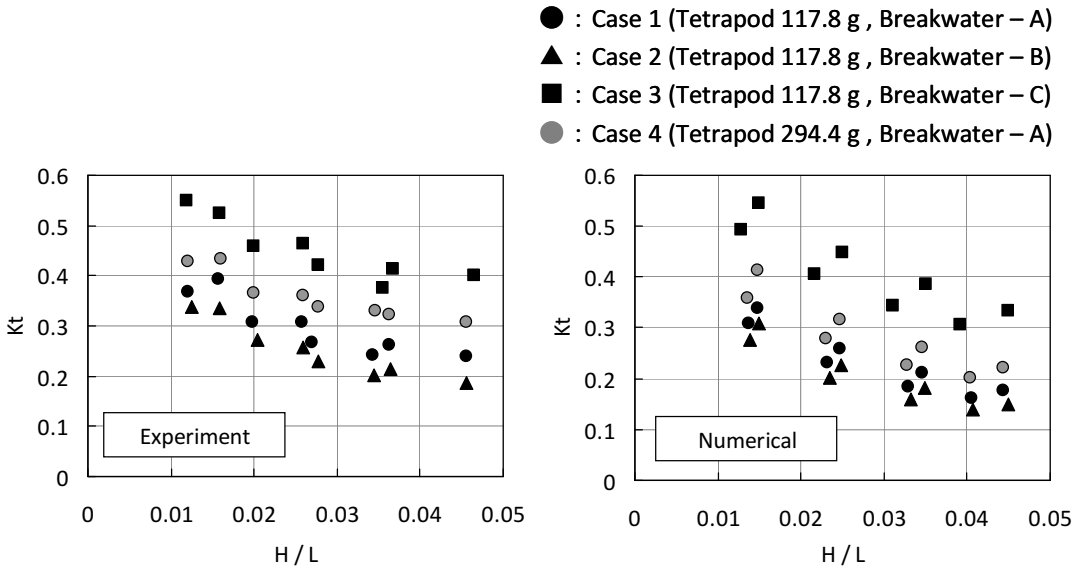

(a) : Tetrapods

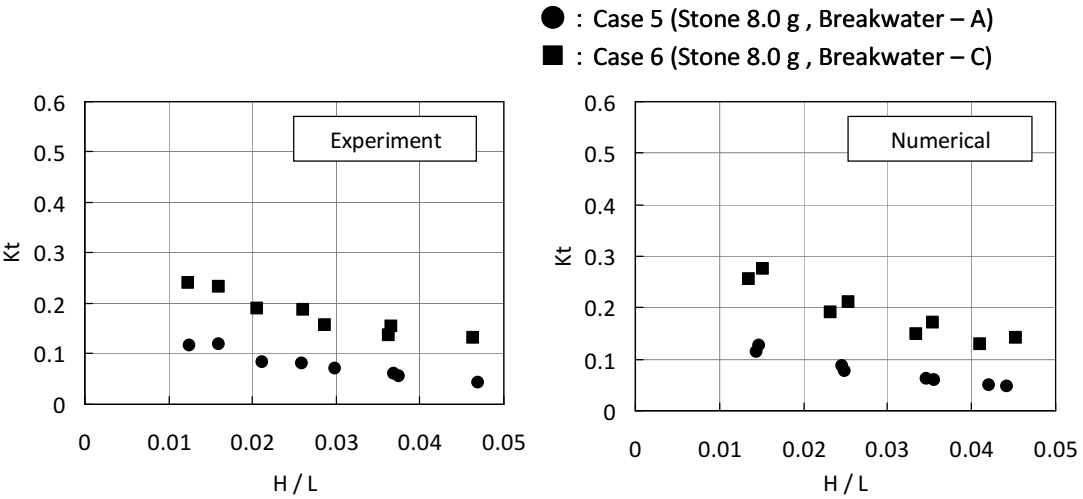

(b) : Stones

Figure 2.17 : Comparison of wave transmission coefficient. Horizontal axis *H*/*L* represents the wave steepness at the breakwater.

The overall underestimate of the transmission coefficient in the case of the tetrapods is considered to be solved by tuning the material constants α_0 and β_0 in the porous model. As for the overestimate of the influence of the wave steepness, it is considered that there is still room for consideration in the calculation formula for the resistance coefficients α and β. As another formulation for the α and β, van Gent (1995) proposed the following formulae using the *KC* number:

$$\alpha = \alpha_0 \frac{(1-n)^2}{n^3} \frac{\nu}{d^2}, \quad \beta = \beta_0 \left(1 + \frac{7.5}{KC}\right) \frac{1-n}{n^3} \frac{1}{d}, \tag{2.12}$$

where, $KC = u_m T / (nd)$, u_m is the maximum oscillating flow velocity, and T is the period of the oscillation. According to this formulae, the resistance coefficient decreases as the wave steepness increases since the KC number increases as the wave steepness increases. Therefore, using this expression is considered to qualitatively improve the computation results. It is necessary to further study for the value of the material constants and the formulation of the resistance coefficients.

2.5.3 Validation of Effectiveness of a Detached Breakwater against Tsunami

The hydraulic model experiment on the effectiveness of a detached breakwater against tsunami performed by Hanzawa et al. (2012) is reproduced by numerical computation. Fig.2.18 shows the schematic layout of the wave flume. A piston type wavemaker was used to generate a solitary wave. A vertical distribution of the wave pressure acting on a seawall was measured. They investigated the effectiveness of a detached breakwater installed in front of the seawall by comparing the wave pressure on the seawall in the presence or absence of the breakwater.

Fig. 2.19 shows the cross-section of the detached breakwater and the measurement position of wave pressure on the seawall. The detached breakwater was composed of tetrapods of mass 59 g. The crown height was set to 4 cm above the still-water level. Two water levels with an offshore water depth h_0 of 43 cm and 40 cm were used. A solitary wave was generated whose wave height was 5.3 cm at St.1.

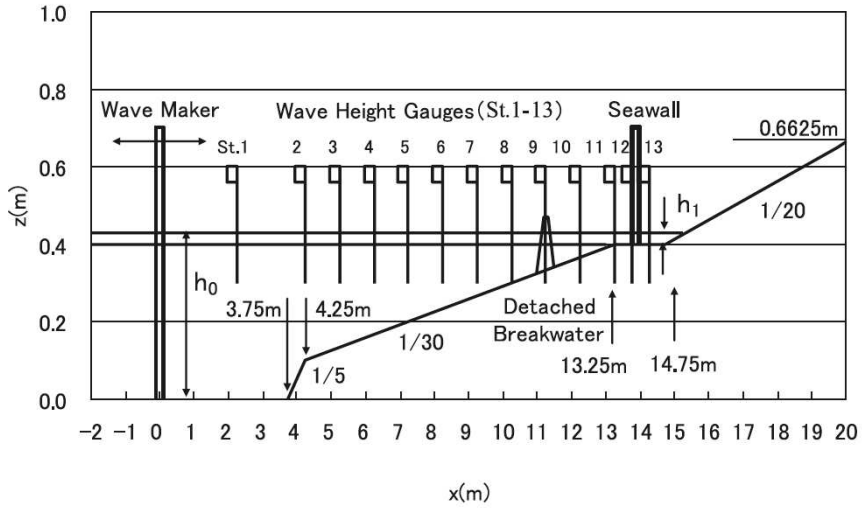

Figure 2.18 : Schematic layout of the wave flume. (from Hanzawa et al., 2012)

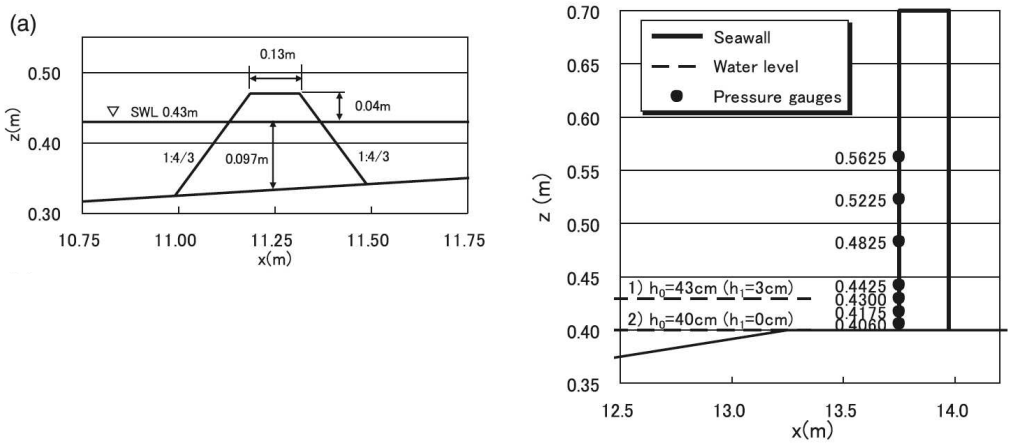

Figure 2.19 : (Left) : Cross-section of the detached breakwater. (Right) : Measurement position of wave pressure. (from Hanzawa et al., 2012)

In the numerical computation, the layout of the wave flume was the same as the hydraulic model experiment. In this validation, the high-tide case of h_0 = 43 cm was selected for comparison. A solitary wave was generated by the method of controlling the wavemaker. The drive signal of the paddle was determined by means of the method by Goring and Raichlen (1981). However, since the computed wave height using the stroke determined by this method was about 0.5 cm smaller than the target value, the stroke was adjusted so that the computed wave height agreed with the target value.

Table 2.12 shows the computation conditions. The computational grid size was basically set to 1 cm. It was subdivided into 0.5 cm around the detached breakwater and the seawall as shown in Fig. 2.20. The material constants α_0 and β_0 for the porous model were determined by referring to Kondo and Takeda (1983).

Table 2.12 : Computation conditions.

Parameter	Value
Grid size	Around breakwater and seawall : Δx = 0.5 cm, Δz = 0.5 cm Otherwise : Δx = 1 cm, Δz = 1 cm
Time increment Δt	Automatic control (Maximum Courant number = 0.25)
Discrete scheme of the transport term	TVD scheme of second-order accuracy
Boundary conditions	Bottom-side, offshore-side, and onshore-side : No-slip Upper-side : Free inlet/outlet with atmospheric pressure
Turbulence model	RNG k-ε model
Physical properties	Density of water : 1.0×10^{3} kg/m^{3} Kinematic viscosity of water : 1.0×10^{-6} m^{2}/s
Specifications of tetrapods	Mass = 59 g, Characteristic diameter d = 2.95 cm, Porosity n = 50%
Material constants	α_0=2100, β_0=2.2
Resistance coefficients	Laminar resistance coefficient α = 1.21 Turbulent resistance coefficient β = 298.3
Inertia coefficient	C_M = 1.2

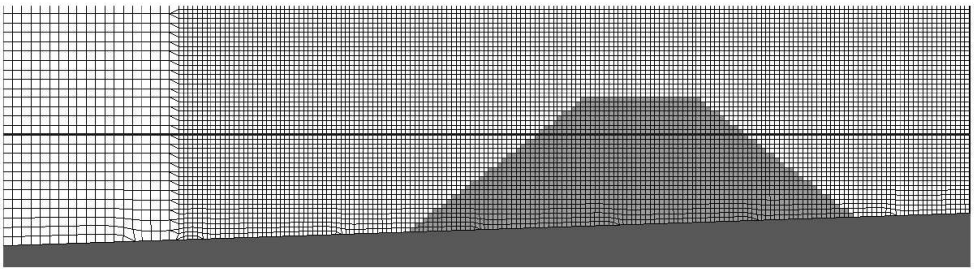

Figure 2.20 : Computational grid around the detached breakwater.

Fig. 2.21 shows a comparison of measured and computed time series of water surface elevation without seawall and detached breakwater. The numerical result well reproduces the increase in the wave height by shoaling. The wave height at the x = 12.25 m around the wave breaking limit is about 1 cm larger in the computation than that in the experiment. The reduction of the wave height due to the wave breaking is reproduced well. Fig. 2.22 shows the water surface elevation with detached breakwater. The overall trend is reasonably reproduced. However, the computed wave height behind the breakwater at x = 12.15 m underestimates compared to the experimental result. Also, the computed reflected wave from the detached breakwater overestimates compared to the experimental result. As for the cause of these discrepancies, it is considered that the resistance coefficients in the porous model are too large. Further investigation is needed for the improvement of the accuracy of the numerical computation.

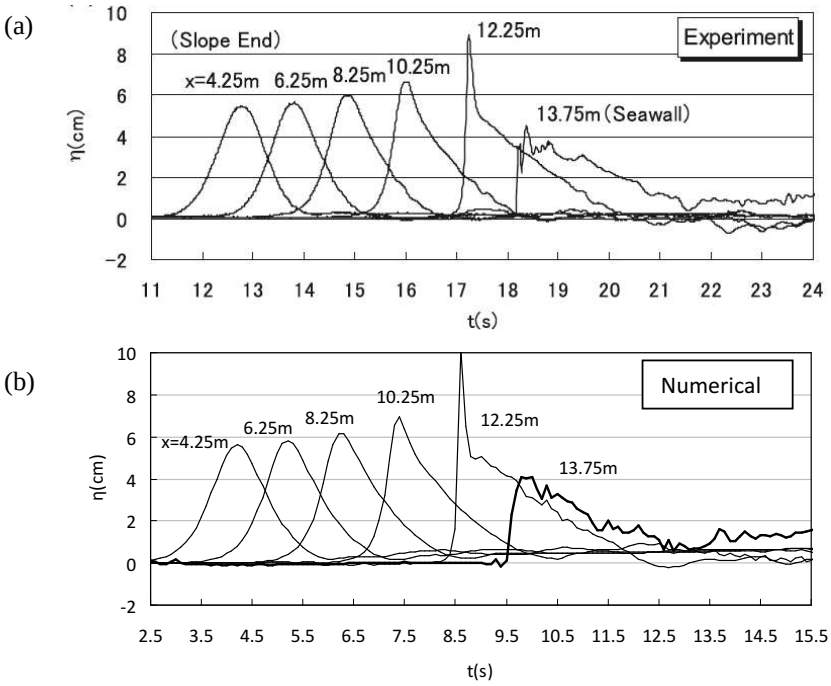

Figure 2.21 : Comparison of time series of water surface elevation (without seawall, without detached breakwater, h_0 = 43 cm). (a) : Experiment (Hanzawa et al., 2012). (b) : Numerical result.

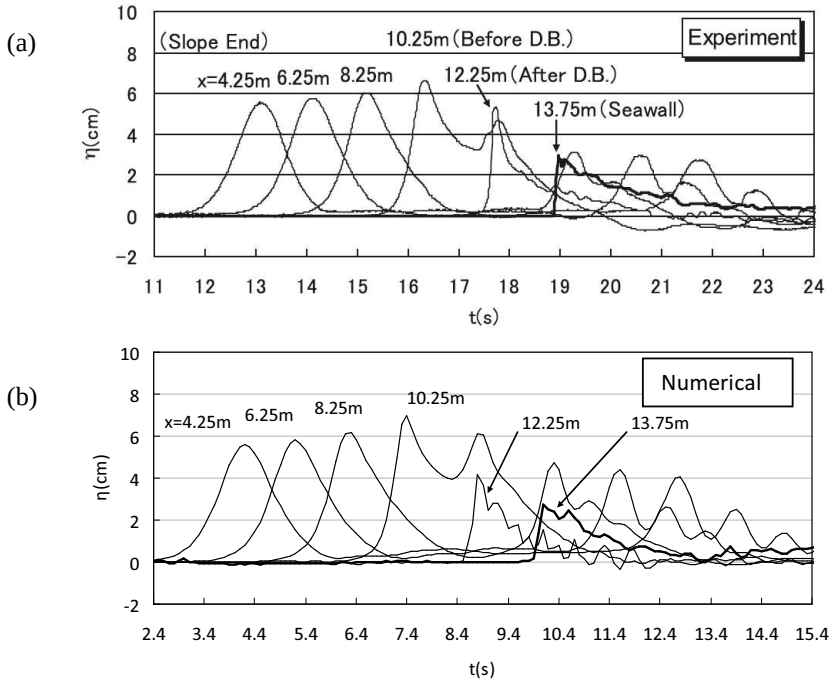

Figure 2.22 : Comparison of time series of water surface elevation (without seawall, with detached breakwater, h_0 = 43 cm). (a) : Experiment (Hanzawa et al., 2012). (b) : Numerical result.

Fig. 2.23 shows a comparison of the measured and computed maximum wave pressure p_{max} on the seawall. The value p_{max} is defined as the maximum wave pressure of the time series for each point. The numerical result agrees well with the experimental one in the case without breakwater. On the other hand, the numerical result underestimates the wave pressure when there is a breakwater. This is presumed to be the result of the overestimate of the resistance due to the detached breakwater in the porous model as mentioned above.

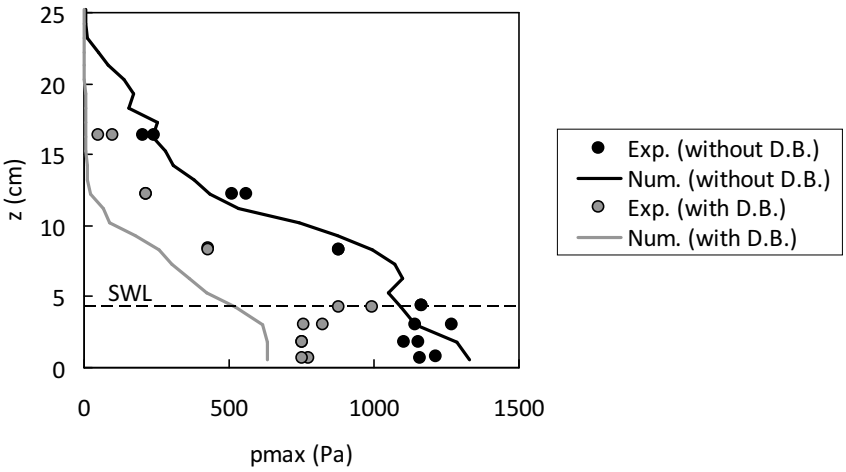

Figure 2.23 : Comparison of wave pressure acting on the seawall.

2.6 Closure

This Chapter developed and validated a versatile numerical wave flume using an OpenFOAM model which is based on an unstructured grid. The main conclusions are shown below:

1. The validation of the water surface profile and wave forces acting on a structure were confirmed through dam-break tests.
2. Wave generation methods by reproducing a wavemaker were presented. Regular waves and irregular waves were generated accurately by this method. Numerical results well reproduced wave shoaling. The position of the wave breaking of the regular wave almost agreed with that from Goda (2010). The aspect ratio of the computational grid should be 1:1 when wave breaking occurs. The deformation

process of irregular wave on the slope was reproduced acceptably. The computed wave height in the surf zone was underestimated by about 10% compared with that by the Goda's model (Goda, 1975).

3. One feature of the wave generation method using the wavemaker is that the total volume of water in the computational domain was conserved well. This is an advantage in performing a long-time simulation. A future challenge will be to introduce a function of active generating-absorbing for long-time simulation.
4. The validation of the porous model was examined by comparing the wave transmission coefficient of a sloping breakwater. The overall trend of the wave transmission coefficient was reproduced by numerical computation. Further study is required on the value of the material constants in the porous model and the formulation of resistance coefficients for the improvement in accuracy.
5. As for the porous model, the validation of effectiveness of a detached breakwater against tsunami was also examined. The propagation of a solitary wave and the pressure acting on the seawall were reproduced well. However, the resistance due to the detached breakwater in the porous model tended to be overestimated. The need for further investigation on the material constants was also shown in this test.

References

Arimitsu, T., Yasuoka, T., Kawasaki, K. (2007) : Applicability of numerical wave flume for wave overtopping phenomenon on steeped seawall with drainage, *Annual Journal of Coastal Engineering, JSCE*, **54**, 726-730 (*in Japanese*).

Arimitsu, T., Yasuoka, T., Kawasaki, K. (2008) : Damage mechanism of armor blocks at toe of rubble mound foundation of composite breakwater, *Annual Journal of Coastal Engineering, JSCE*, **55**, 946-950 (*in Japanese*).

Brackbill, J.U., Kothe, D.B., Zemach, C. (1992) : A continuum method for modeling surface tension, *Journal of Computational Physics*, **100**, 335-354.

Brorsen, M., Larsen, J. (1987) : Source generation of nonlinear gravity waves with boundary integral equation method, *Coastal Engineering*, **11**, 93-113.

Coastal Development Institute of Technology (2001) : Research and development of numerical wave flume (CADMAS-SURF), CDIT Library, No. 12, 296p (*in Japanese*).

Cruz, E., Yokoki, H., Isobe, M., Watanabe, A. (1993) : Nonreflecting boundary

condition for nonlinear wave equation, *Proceedings of Coastal Engineering, JSCE,* **40**, 46-50 (*in Japanese*).

Engelund, F. (1953) : On the laminar and turbulent flows of ground water through homogeneous sand, *Transactions of the Danish Academy of Technical Sciences*, Vol. 3, No. 4.

Fujiwara, R. (2008) : A method for modifying a horizontal velocity of irregular wave generation by a linear theory, *Annual Journal of Civil Engineering in the Ocean, JSCE*, **24**, 873-878 (*in Japanese*).

Goda, Y. (1975) : Irregular wave deformation in the surf zone, *Coastal Engineering in Japan*, **18**, 13-26.

Goda, Y. (2010) : Reanalysis of regular and random breaking wave statistics, *Coastal Engineering Journal*, **52** (1), 71-106.

Goda, Y., Kikuya, T. (1964) : The generation of water waves with a vertically oscillating flow at a channel bottom, *Report of Port and Harbour Research Institute*, **9**, 1-24.

Gomez-Gesteira, M., Cerqueiro, D., Crespo, C., Dalrymple, R.A. (2005) : Green water overtopping analyzed with a SPH model, *Ocean Engineering*, **32**, 223-238.

Goring, D., Raichlen, F. (1980) : The generation of long waves in the laboratory, *Proceedings of 17th International Conference on Coastal Engineering*, Sydney, Australia, 763-783.

Hamaguchi, M., Kubota, S., Matsumoto, A., Hanzawa, M., Yamamoto, M., Moritaka, H., Shimosako, K. (2007) : Hydraulic stability of new flat type armor block with very large openings for use in composite breakwater rubble mound protection, *Proceedings of Coastal Structures 2007*, Venice, Italy, 116-127.

Hanzawa, M., Matsumoto, A., Tanaka, H. (2012) : Applicability of CADMAS-SURF to evaluate detached breakwater effects on solitary tsunami wave reduction, *Earth Planets Space*, **64**, 955-964.

Higuera, P., Lara, J.L., Losada, I.J. (2013) : Simulating coastal engineering process with OpenFOAM®, *Coastal Engineering*, **71**, 119-134.

Jacobsen, N.G., Fuhrman, D.R., Fredsoe, J. (2012) : A wave generation toolbox for the open-source CFD library : OpenFoam®, *International Journal for Numerical Methods in Fluids 2012*, **70**, 1073-1088.

Janosi, I.M., Jan, D., Szabo, K.G., Tel, T. (2004) : Turbulent drag reduction in dam-break flows, *Experiments in Fluids*, **37**, 219-229.

Jansen, B., Jacobsen, N.G., Christensen, E.D. (2014) : Investigations on the porous media equations and resistance coefficients, *Coastal Engineering*, **84**, 56-72.

Jasak, H., Tukovic, Z. (2007) : Automatic meth motion for the unstructured finite

volume method, *Transactions of FAMENA*, **30 (2)**, 1-18.

Kawasaki, K., Kiku, M., Sasada, Y. (2008) : Numerical and experimental study on wave deformation and overtopping around vertical seawall in coral reef sea area, *Proceedings of the 18th International Offshore and Polar Engineering Conference*, Vancouver, Canada, 698-705.

Kleefsman, K.M.T., Fekken, G., Veldman, A.E.P., Iwanowski, B., Buchner, B. (2005) : A Volume-of-Fluid based simulation method for wave impact problems, *Journal of Computational Physics*, **206**, 363-393.

Kondo, H., Takeda, H. (1983) : Wave dissipating structures, Morikita Publishing Co. Ltd., 275p (*in Japanese*).

Kondou, M., Arikawa, T., Seki, K., Murakawa, H. (2009) : Damage mechanism of armor units at the breakwater head using the 3D numerical wave tank, *Journal of JSCE, Ser. B2* (*Coastal Engineering*), **65**, 861-865 (*in Japanese*).

Kotake, Y., Obuchi, Y., Takahashi, S. (2007) : Application of the numerical wave flume to the analysis of wave pressures upon wave absorbing caisson, *Annual Journal of Coastal Engineering, JSCE*, **54**, 816-820 (*in Japanese*).

Kubota, S., Hamaguchi, M., Matsumoto, A., Hanzawa, M., Yamamoto, M. (2008) : Wave force and stability of new flat type concrete block with large openings for submerged breakwaters, *Proceedings of 31st International Conference on Coastal Engineering*, Hamburg, Germany, 3423-3435.

Matsumoto, A. (2009) : Numerical analysis on wave transmission over breakwaters using VOF-type numerical wave flume, *Journal of JSCE, Ser. B2* (*Coastal Engineering*), **65**, 781-785 (*in Japanese*).

Matsumoto, A., Yamamoto, M., Mano, A. (2011) : Evaluation of the critical condition on armor block stability for submerged breakwaters, *Proceedings of Coastal Structures 2011*, Yokohama, Japan, 834-845.

Nakano, O., Kyono, T., Yasuda, K., Fujii, N. (2002) : Application of a numerical wave flume for wave forces, overtopping, and transmitted waves on sloping breakwater by regular and irregular waves, *Proceedings of Coastal Engineering, JSCE*, **49**, 726-730 (*in Japanese*).

Ohyama, T., Tsuchida, M., Kawaguchi, T., Suzuki, Y. (1997) : Nonreflective generation of nonlinear waves in laboratory wave tank, *Proceedings of Coastal Engineering, JSCE*, **44**, 11-15 (*in Japanese*).

Okuma, Y., Kyono, T., Shibasaki, N., Yasuda, K., Nakano, O. (2003) : Study on cover block stability of caisson considered difference of damaged degree based on wave velocity, *Proceedings of Coastal Engineering, JSCE*, **50**, 751-755 (*in Japanese*).

OpenFOAM, http://www.openfoam.com/

Rusche, H. (2002) : Computational fluid dynamics of dispersed two-phase flows at high phase fractions, Ph.D. thesis, Imperial College, University of London.

Shuto, N. (1974) : Nonlinear long waves in a channel of variable section, *Coastal Engineering in Japan*, **17**, 1-12.

van Gent, M.R.A. (1995) : Wave interaction with permeable coastal structures, Ph.D. thesis, Delft University of Technology.

Chapter 3

Stability of Armor Units Covering Rubble Mound of Composite Breakwaters against Overtopping Jet Caused by Tsunami with Rapid Water Level Rise

3.1 Introduction

The 2011 Off the Pacific Coast of Tohoku Earthquake Tsunami which occurred on 11 March 2011 took a heavy toll of human lives. Marine structures including breakwaters were also severely damaged. One of the causes of breakwater failure was scouring of the rubble foundation and subsoil on the harbor-side of the breakwaters due to overflow. This was a formerly inconceivable type of failure. Therefore, it became necessary to completely reconsider the design method for breakwaters (Ministry of Land, Infrastructure, Transport and Tourism of Japan [MLIT], 2013).

As a countermeasure against a large tsunami in the future, a resilient breakwater against tsunami is requested. One possible method is the placement of a widened protection mound using additional rubble stones behind the breakwater to prevent sliding of the caisson (MLIT, 2013; Fisheries Agency of Japan, Fisheries Infrastructure Department, 2014). Installing armor units on the rubble mound on the harbor-side would also be required to prevent scouring around the rubble mound (Fig. 3.1).

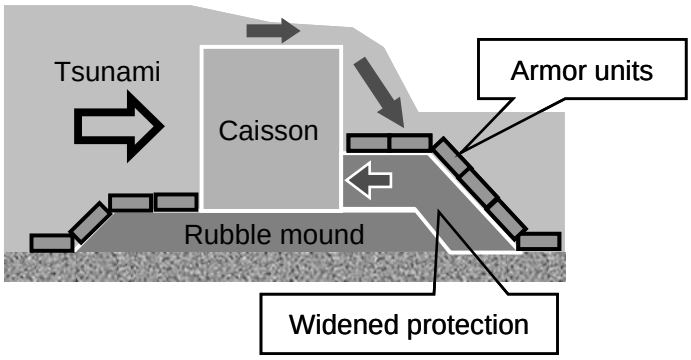

Figure 3.1 : Schematic diagram of the resilient breakwater.

In the design work, it is required to determine the mass of the armor units which is needed to ensure the stability against tsunami overflow. In past studies on the stability of armor units against tsunami, Iwasaki et al. (1984) and Tanimoto et al. (1988) experimentally investigated the stability of armor units installed on submerged mounds in the open sections of a tsunami breakwater against flow. In addition, Sakakiyama and Matsuyama (2011), Hanzawa et al. (2012) conducted experiments on the stability of wave-dissipating blocks of sloping breakwaters and detached breakwaters. However, the stability of armor units in composite breakwaters against tsunami overflow is not clear since this phenomenon was inconceivable before the Tohoku tsunami in 2011.

Guidelines for Tsunami-Resistant Design of Breakwaters (MLIT, 2013) mentioned the Isbash formula (Coastal Engineering Research Center [CERC], 1977) as the calculation method for the required mass of the armor units against tsunami overflow. However, there are practical issues that the required mass is too sensitive to variations in the estimated flow velocity and that the applicability of the Isbash formula to the tsunami overflow is not validated enough. This study aims to clarify the stability of the armor units against tsunami overflow and propose a practical design method.

Two types of tsunami are considered in this study when investigating the stability of armor units against tsunami overflow. One is a tsunami with a rapid water level rise, the other is a steady overflow. As an example of the former: It was reported that soliton fission was generated in Kuji bay during the Tohoku tsunami in 2011, and the crest of the wave broke on the offshore side of the breakwater at the Port of Kuji where it flowed over the breakwater as a breaking bore (Takahashi et al., 2011; Kashima and Hirayama, 2013). Also, it was reported that the water level rose rapidly at the offshore breakwaters of the Port of Sendai-Shiogama and the Port of Soma during the same tsunami according to the numerical simulation (Higashiyama et al., 2013). According to this simulation, the speed of the water level rise was about 1 m/s as an order. When a

breaking bore or a tsunami with a steep front attacks breakwaters, the water level in front of the caisson rises rapidly and the overtopped water rigorously impinges into the harbor-side.

On the other hand, the speed of the water level rise at the North Hattaro Breakwater (middle section) at the Port of Hachinohe was 0.01 m/s as an order according to Higashiyama et al. (2013). In such a case, it can be treated as a steady phenomenon.

In this Chapter, the armor stability is examined against overtopping jets caused by a tsunami with rapid water level rise. Hydraulic model experiments are conducted to examine the appropriate shapes of armor units against the initial impact of the impingement of the water jets. An improvement method for the structure for enhancing the stability is also proposed. A numerical analysis is also performed. The stability of the armor blocks is predicted by computing the fluid force acting on each block.

3.2 Hydraulic Model Experiment on Armor Stability

3.2.1 Experimental Method

Experiments were carried out using a 40 m long, 1 m wide and 1.2 m deep wave flume. The model scale was set to 1/50. Fig. 3.2 shows the schematic layout of the wave flume. The breakwater model was placed on the 1/30 bottom slope. An example of the cross section of the breakwater is shown in Fig. 3.3. The experiments were conducted by changing the shape, mass, and arrangement method of the armor units at the harbor-side of the breakwater as shown in Table 3.1. Armor stones of weight 8 g, two kinds of flat-type armor blocks, and wave-dissipating blocks with various weights were used.

Since the experiments are concentrated on the understanding of the stability of the armor units against initial impact by the overtopped jet, the tsunami was generated with a piston type wavemaker to reproduce a single hump of water. The wave paddle was pushed forward for 5 s with a half cycle of sinusoidal motion. Four tsunami waves with different heights were prepared by varying the stroke of the wave paddle. The strokes for the four tsunami waves were 39.0 cm, 58.5 cm, 66.3 cm, and 78.0 cm, respectively (hereafter referred to as Tsunamis A, B, C, and D, respectively). In the stability tests, four tsunami wave were generated in this order. The armor units and rubble mound were not rebuilt after tsunami attack with each height. The cross-sectional shape before and after each tsunami attack was measured by using a topography profiler in the case of the armor stones. In the case of the concrete blocks, the number of moved blocks was

counted as an accumulated number.

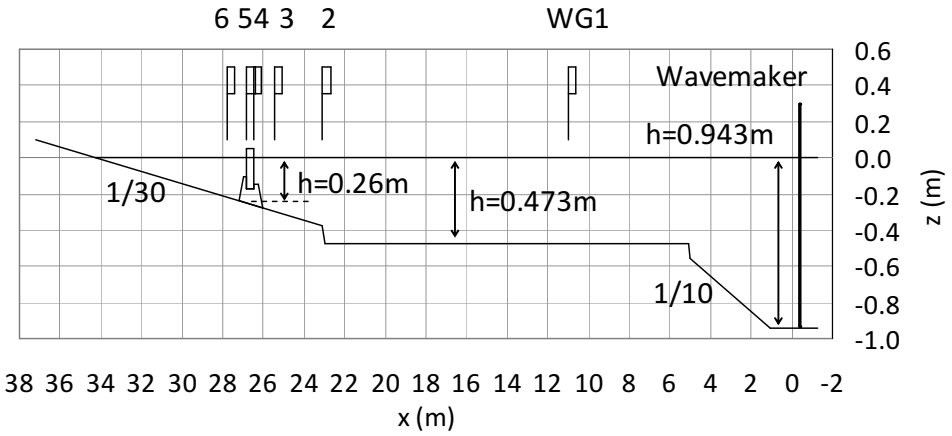

Figure 3.2 : Schematic layout of the wave flume.

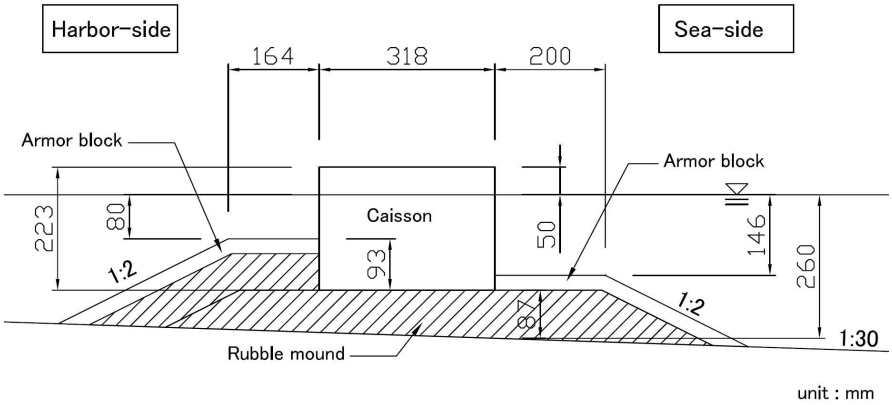

Figure 3.3 : Example of the cross-section of the breakwater.

Table 3.1 : Experimental conditions of harbor-side armor layers. Values in brackets represent the converted values to the prototype scale.

Armor unit	Mass	Arrangement method
Armor stone	8 g (1 t)	2 layers
Flat-type armor block A 	130 g (16.2 t)	2 units in the crown section
		4 units in the crown section
	244 g (30.5 t)	2 units in the crown section
Flat-type armor block B 	33 g（4.1 t）	3 units in the crown section
	65 g (8.1 t)	2 units in the crown section
	129 g (16.2 t)	2 units in the crown section
Wave-dissipating block 	116 g (14.5 t)	2 layers
		2 layers, Reinforced at the toe
	230 g (28.8 t)	2 layers

3.2.2 Experimental Result

3.2.2.1 Characteristics of the tsunami

Fig. 3.4 shows a time series of water surface elevations in the case of Tsunami D before installing the breakwater model. As the tsunami progresses, the front of the wave becomes steep and the wave begins to split. The maximum water level at WG4 is 12.3 cm (6.15 m in the prototype scale). A time series of water surface elevations after installing the breakwater in the case of Tsunami D is shown in Fig. 3.5. The duration of the overflow of tsunami is about 4 s (28 s in the prototype scale) and the maximum overflow depth is 14.0 cm (7.0 m in the prototype scale). A time series of water surface elevation for each tsunami measured at WG4 is shown in Fig. 3.6. The maximum overflow depth of each tsunami is shown in Table 3.2.

A snapshot of the overflow jet impinging on to the harbor-side is shown in Fig. 3.7. The water jet inflows from near the shoulder of the slope, and then flows into the seabed along the slope.

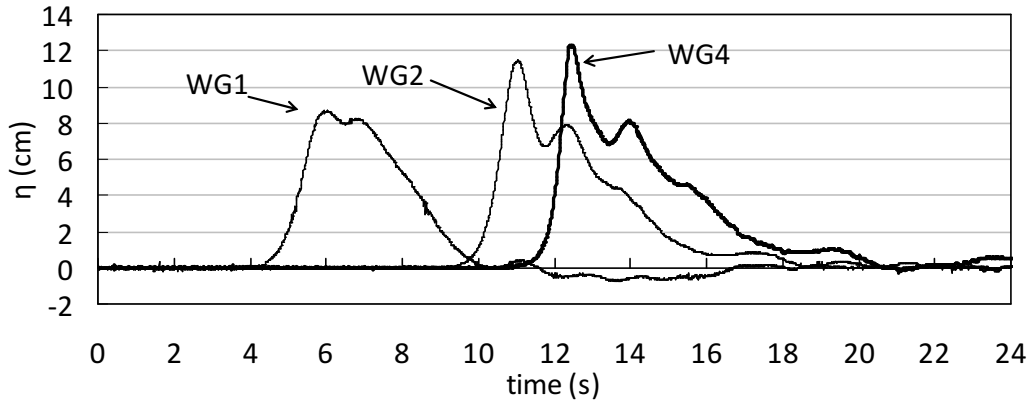

Figure 3.4 : Time series of water surface elevation before installing the breakwater. Stroke of the wavemaker is 78 cm (Tsunami D).

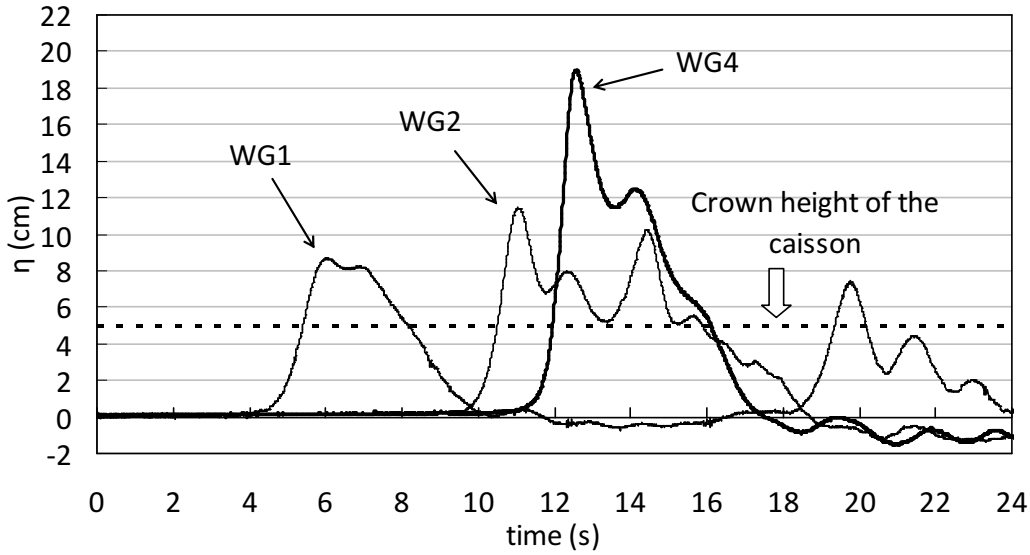

Figure 3.5 : Time series of water surface elevation after installing the breakwater. Stroke of the wavemaker is 78 cm (Tsunami D).

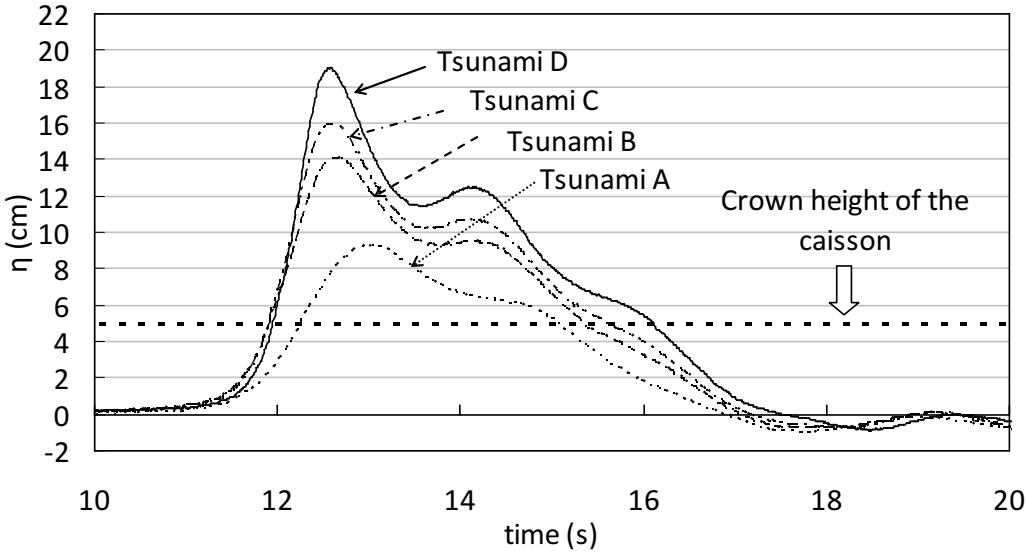

Figure 3.6 : Time series of water surface elevation of each tsunami wave after installing the breakwater measured at WG4.

Table 3.2 : Maximum overflow depth of each tsunami. Values in brackets represent the converted values to the prototype scale.

Tsunami	Stroke	Maximum overflow depth
Tsunami A	39.0 cm	4.2 cm (2.12 m)
Tsunami B	58.5 cm	8.9 cm (4.47 m)
Tsunami C	66.3 cm	11.0 cm (5.52 m)
Tsunami D	78.0 cm	14.1 cm (7.05 m)

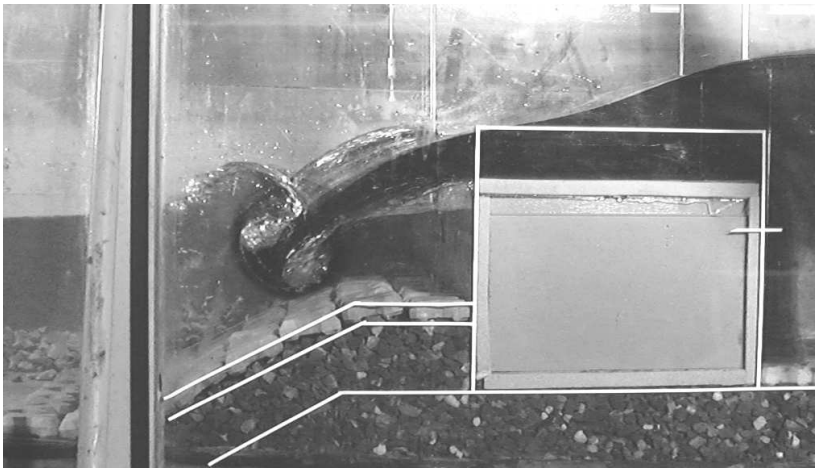

Fig. 3.7 : Snapshot of the overflow jet (Tsunami D).

3.2.2.2 Stability of the armor stones

Fig. 3.8 shows the cross sectional change in the harbor-side mound covered with armor stones. The damage began after Tsunami B. After Tsunami D, the armor stones at the

slope section were largely scattered and the rubble stones under the armor stones were also scoured out in this case as shown in Fig. 3.9.

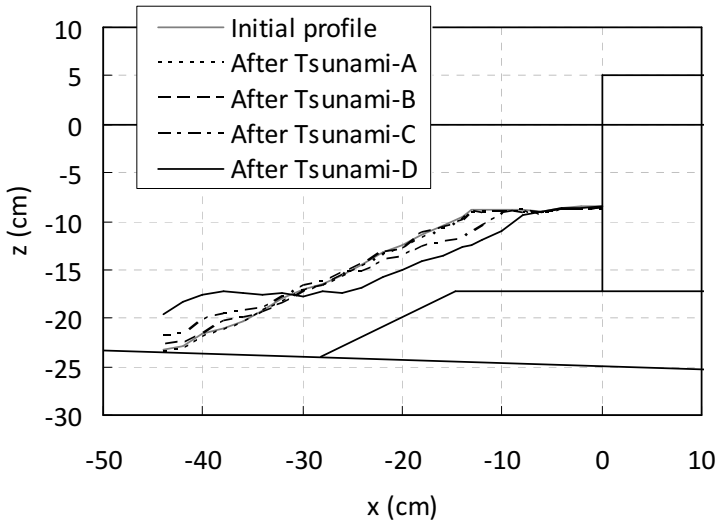

Figure 3.8 : Cross sectional change in the harbor-side mound covered with the armor stones.

Figure 3.9 : Damage to the armor stones after Tsunami D.

3.2.2.3 Stability of the flat-type armor blocks

In the case of the concrete blocks, almost no damage occurred from Tsunamis A, B, and C. The following describes the results of Tsunami D unless otherwise stated.

The results of armor block A are shown in Fig. 3.10. In the cases of armor block A with 2 blocks in the crown section (Fig. 3.10(a) and 3.10(b)), serious damage was seen to concentrate at the shoulder of the slope for both sizes of blocks (130 g and 244 g). In the case of the blocks of mass 130 g, the toe of the slope was also damaged. As the failure situation of the blocks, when a vortex, which was generated by the impingement

of water jet onto the harbor-side water surface, passed through above the block, the blocks on the slope section lifted and washed away. Since this phenomenon was not observed in the experiments using the steady overflow of tsunami, it is a phenomenon specific to the case of a tsunami with rapid water level rise.

In the case of armor block A with a wider crown section (4 units in the crown section), overtopped water impinged on to the crown section. Many blocks on the crown section were damaged, whereas the blocks around the toe were stable (Fig. 3.10(c)). This results shows that the impingement position of the overtopped water is important for the armor stability.

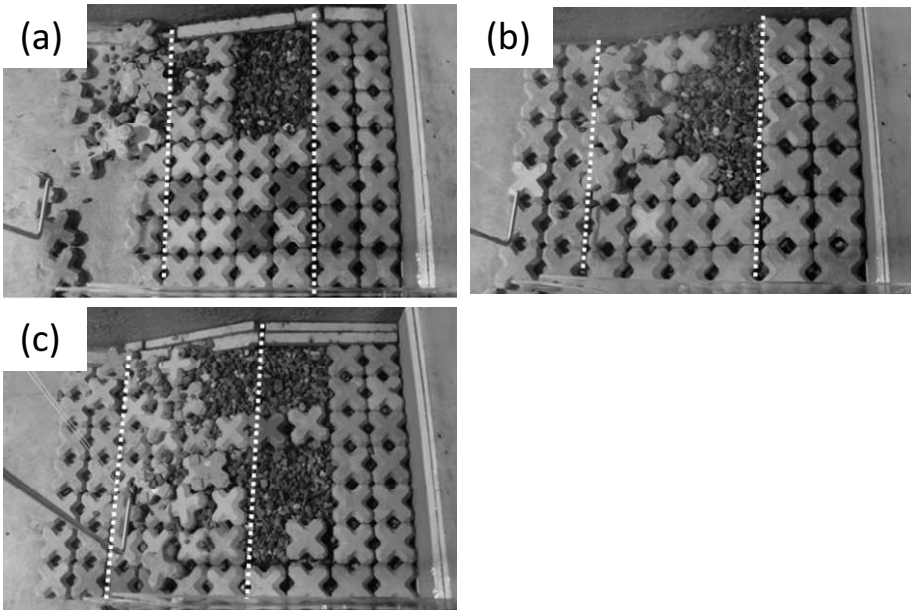

Figure 3.10 : Experimental results of the armor block A. (a) : Mass 130 g, 2 units in the crown section. (b) : Mass 244 g, 2 units in the crown section. (c) : Mass 130 g, 4 units in the crown section.

The results of armor block B are shown in Fig. 3.11. Block B of mass 129 g was stable. The armor blocks B of mass 65 g and 33 g also stayed stable on the main part of the mound, although the toe of the slope was damaged through sliding. Comparing to armor block A, the stability of armor block B was obviously higher. The main feature of armor block B is the five large holes as shown in Table 3.1. The large holes in the block contribute to a higher stability against wave action due to the reduction of the uplift force (Hamaguchi et al., 2007; Kubota et al., 2008). The experimental results proved that the large holes are also effective in an impinging tsunami as well as wind waves. The mechanism of stabilization due to the holes will be investigated by numerical analysis in the next section.

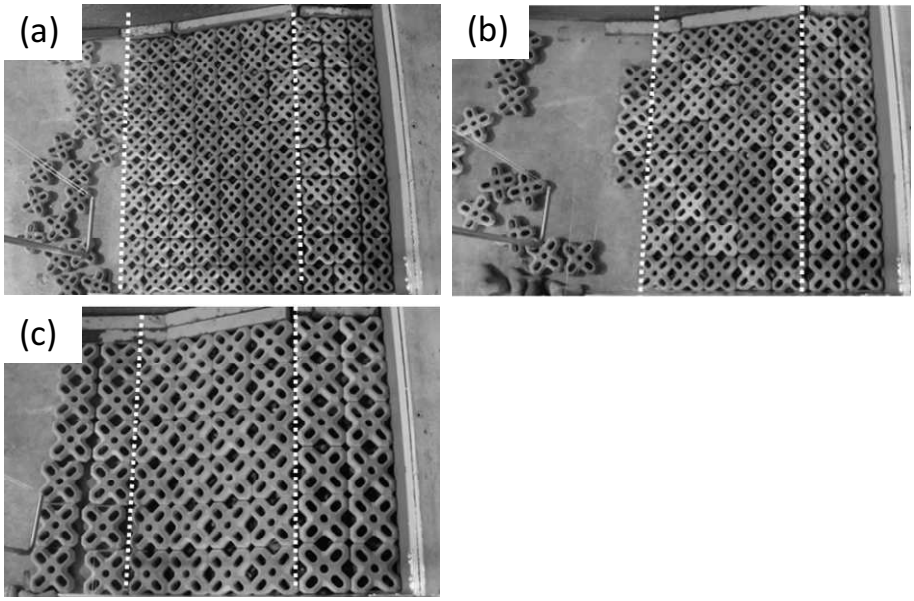

Figure 3.11 : Experimental results of the armor block B. (a) : Mass 33 g, 3 units in the crown section. (b) : Mass 65 g, 2 units in the crown section. (c) : Mass 129 g, 2 units in the crown section.

3.2.2.4 Stability of the wave-dissipating blocks

The results of the wave-dissipating blocks are shown in Fig. 3.12. The wave-dissipating blocks of mass 230 g were stable. In the case of the blocks of mass 116 g, the main part of the mound stayed stable though the toe of the slope was damaged. When the vortex passed through above the blocks at the slope section, a slight lifting-up was observed.

In the cases of the wave-dissipating blocks, it is considered that the blocks on the slope section are resistant due to their interlocking, whereas the blocks at the toe are relatively unstable since there is no support behind them. Therefore, to enhance the stability, armor blocks A of mass 244 g were additionally placed at the toe of the slope as reinforcement to the wave-dissipating blocks of mass 116 g. As the result, the whole unit kept stable as shown in Fig. 3.13.

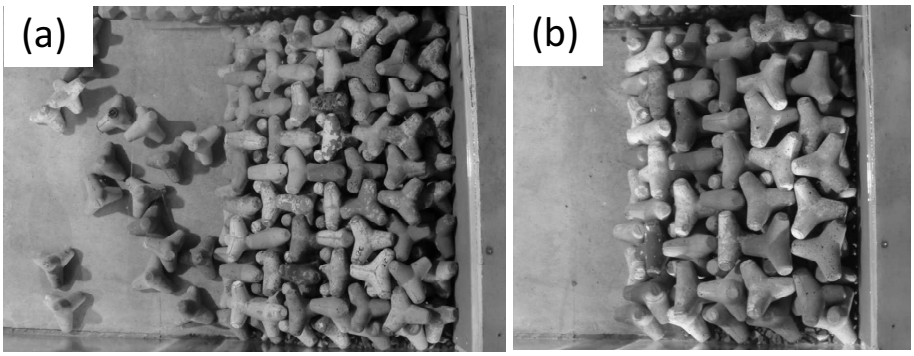

Figure 3.12 : Experimental results of the wave-dissipating blocks. (a) : Mass 116 g. (b) : Mass 230 g. Placed in two layers.

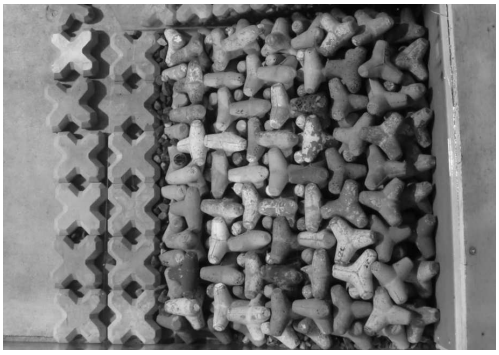

Figure 3.13 : Experimental results of the wave-dissipating blocks of mass 116 g reinforced by the armor block A of mass 244 g at the toe.

3.3 Numerical Analysis on Tsunami Overtopping Caisson

3.3.1 Numerical Analysis Method

A multiphase flow solver using the VOF method within the OpenFOAM CFD model was used to reproduce the tsunami overtopping the caisson. The governing equations were the Navier-Stokes equation, the continuity equation, and the transport equation of VOF function. This VOF method within the OpenFOAM solved both the air and water phases. The density of fluid and the viscosity coefficient of fluid were used as the values averaged for each cell.

The finite Volume Method with an unstructured grid was used. The PISO method was used for the calculation of the Navier-Stokes equation. The TVD scheme of second-order accuracy was used for the discretization of the transport term. The Euler implicit method was used for the time integration method, and time increment was

automatically controlled so that the maximum Courant number might be kept less than 0.25. The RNG k-ε turbulence model was used. The rubble mound was modeled as a porous structure. The hydraulic flow resistance **R** in the porous medium was expressed by a D-F relationship as shown below:

$$\mathbf{R} = -\left(\alpha\mathbf{u} + \beta|\mathbf{u}|\mathbf{u}\right), \tag{3.1}$$

where, α is the laminar resistance coefficient and β is the turbulent resistance coefficient. These coefficients were obtained by using the empirical formulae from Engelund (1953) as follows:

$$\alpha = \alpha_0 \frac{(1-n)^3}{n^2}\frac{\nu}{d^2}, \quad \beta = \beta_0 \frac{1-n}{n^3}\frac{1}{d}, \tag{3.2}$$

where, ν is the kinematic viscosity of water, d is a nominal diameter of the stone, n is the porosity, and α_0 and β_0 are the material constants. The porosity of the stone structure n was set to 0.4 and the nominal diameter of the stone d was set to 14.3 mm. The material constants α_0 and β_0 were set to 1500 and 3.6, respectively, referring to Kondo and Takeda (1983).

A tsunami was generated by extruding a wall boundary corresponding to the wavemaker at a prescribed speed as well as in the experiments. The computational grid around the wavemaker was moved along with the movement of the wavemaker. This was done by using a dynamic mesh functionality (Jasak and Tukovic, 2007) implemented in the OpenFOAM.

A bird's-eye view of the computational grid around the breakwater is shown in Fig. 3.14. The grid was subdivided into four stages. A two-dimensional calculation was done in Regions 1 and 2, a three-dimensional calculation was done in Regions 3 and 4 around the blocks. The grid size in the *z* direction and the *x* direction of Region 1 were set to 1 cm (50 cm in the prototype scale). The grid of Region 2 was subdivided into one-eighth. This was subdivided in the *y* direction in Region 3 so that the grid size in the *y* direction became about 1 cm, and further subdivided in the *y* direction into one-eighth in Region 4.

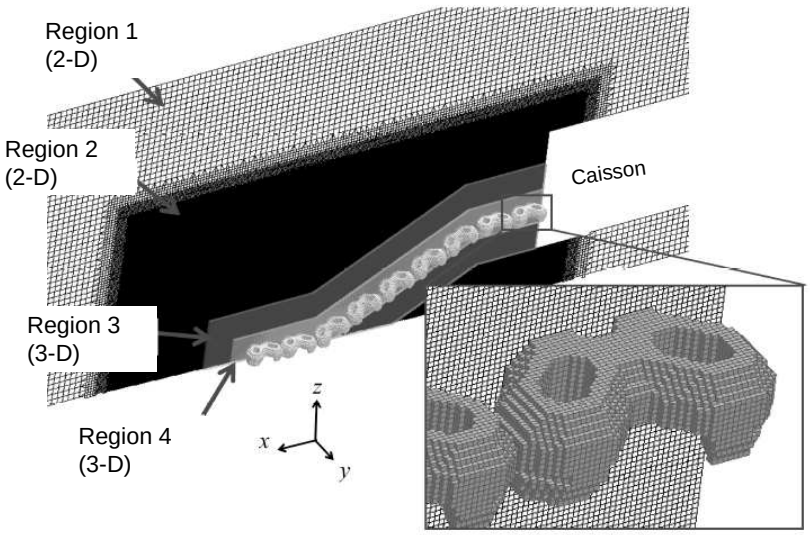

Figure 3.14 : Bird's-eye view of computational grid around the breakwater.

3.3.2 Numerical Result of Water Surface Profile

Fig. 3.15 shows a comparison of the computed time series of water surface elevations with the measured ones. The numerical results accurately reproduced the measured ones. A comparison of the impinging water jet is shown in Fig. 3.16. The numerical result reproduced the situation that the overtopped water impinged onto the harbor-side water surface while involving air and that vortices were generated on both sides of the water jet.

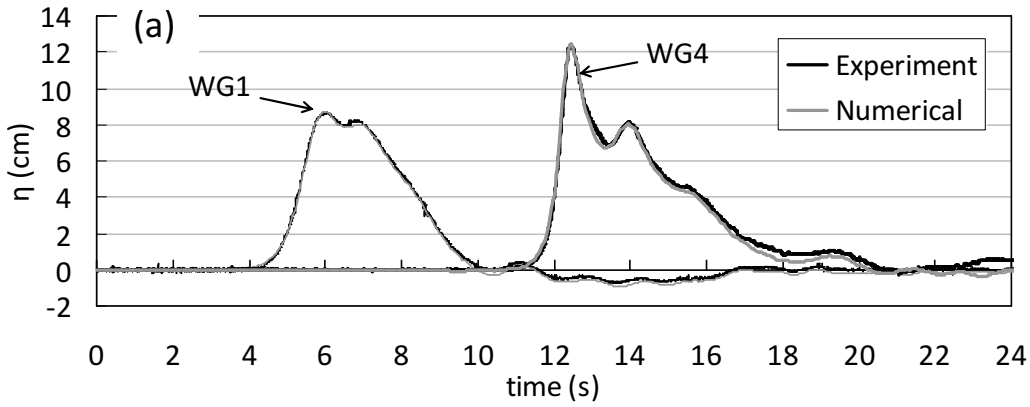

Figure 3.15(a) : Comparison of the computed and measured time series of water surface elevation before installing the breakwater.

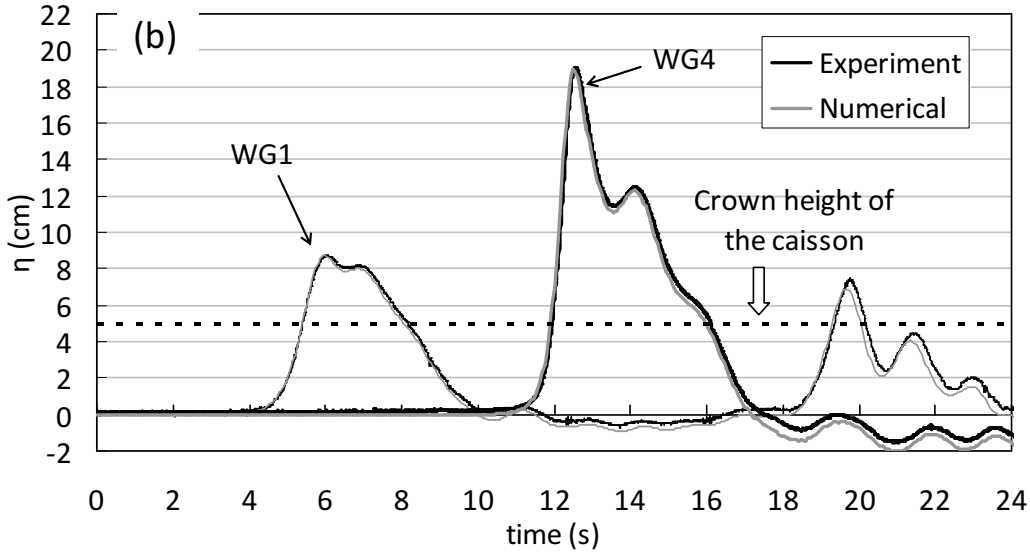

Figure 3.15(b) : Comparison of the computed and measured time series of water surface elevation after installing the breakwater.

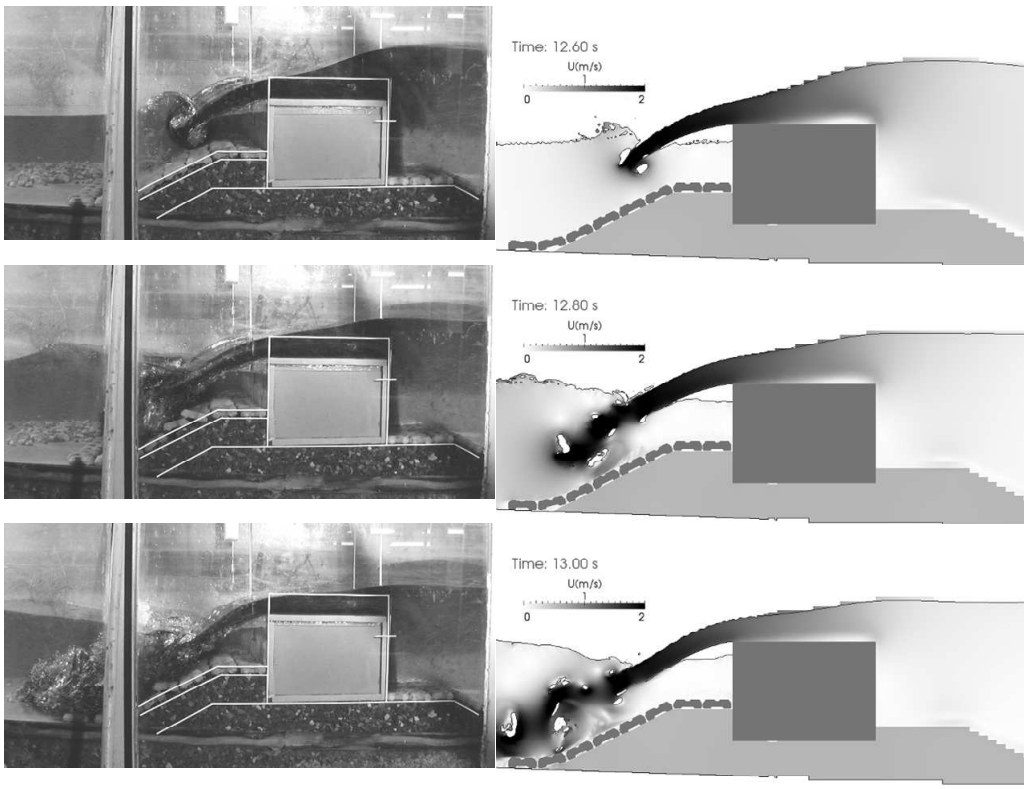

Figure 3.16 : Comparison of the impinging jet. (Left) : Experiment. (Right) : Numerical result.

3.4 Numerical Analysis on Stability of Armor Blocks

3.4.1 Effect of Holes in Armor Blocks

The effect of the holes in the armor blocks was numerically examined by comparing the fluid force acting on armor block B and the block without holes. The fluid force was obtained by integrating the pressure around the block surface. The armor block B of mass 65 g was used. The block without holes used for the comparison has the same outer dimensions as block B. Fig. 3.17 shows a hodograph of fluid forces when a counterclockwise vortex was passing through above the block. The direction of the fluid force changed counterclockwise along with the passage of the vortex. This corresponds to the behavior of the blocks observed in the experiments. Comparing the results of the block without holes, the fluid force in the direction away from the slope was reduced to about a half by providing the holes.

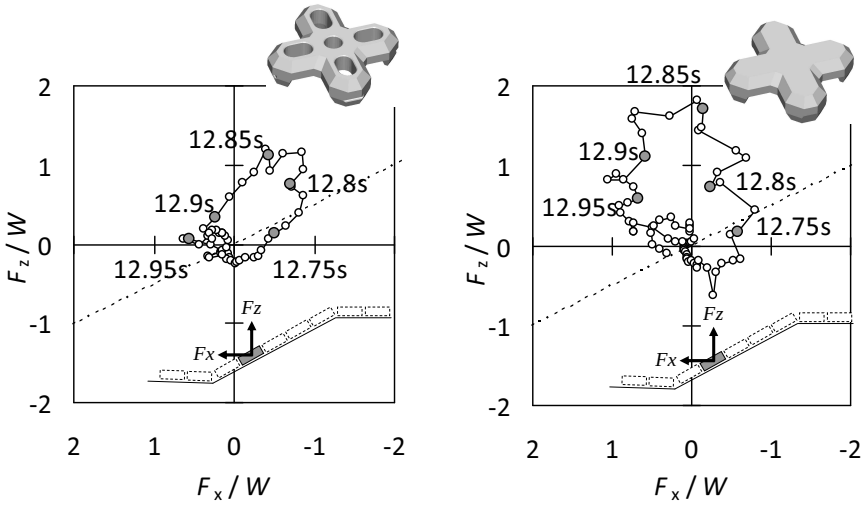

Figure 3.17 : Hodograph of fluid forces acting on the block. (Left) : Armor block B. (Right) : Armor block without holes. *W* : Underwater weight of the block.

Fig. 3.18 shows the iso-pressure lines around the blocks when the fluid forces take their maximum value in the direction away from the slope. The pressure difference between the top and bottom surfaces of block B is smaller than that of the block without holes. These results clarify the reason why block B showed high stability against the water jet in the experiments.

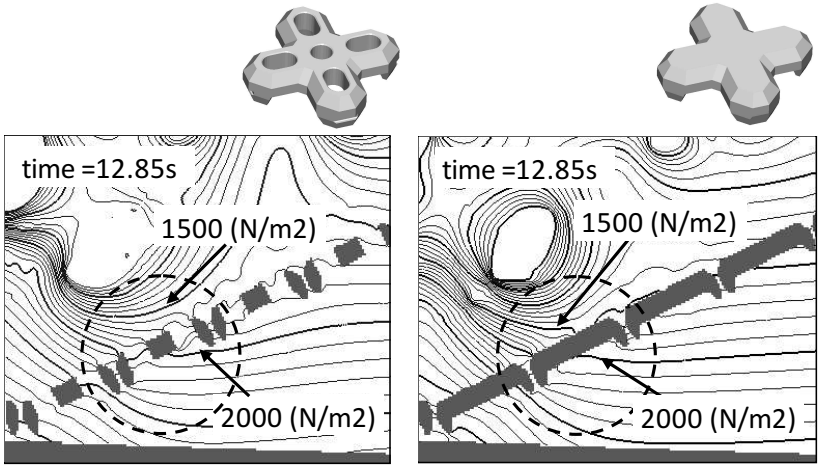

Figure 3.18 : Iso-pressure line around the block. (Left) : Armor block B. (Right) : Armor block without holes.

3.4.2 Estimation of Amount of Lifting-up of Armor Blocks

The amount of lifting-up of the block was estimated by using the time series of fluid force acting on the block obtained from the numerical computation. In this analysis, only the fluid force, the buoyant force, and the self-weight were considered. Other forces such as the friction force between the blocks were disregarded. The definition of the coordinate system is shown in Fig. 3.19. *X*-axis and *Z*-axis are set to the tangential and normal direction of the slope, respectively. The acceleration, velocity, and position in the normal direction of the slope can be written as d^2Z/dt^2, dZ/dt, Z, respectively.

The following equation of motion was solved to calculate the displacement of the block:

$$m\frac{d^2Z}{dt^2} = F_Z \ , \tag{3.3}$$

where, m is the mass of the block, F_z is the sum of the fluid force, buoyancy, and the gravitational force in the Z direction. The acceleration, velocity, and position of the block at the time $t + \Delta t$ are expressed as Eq. (3.4), Eq. (3.5), and Eq. (3.6), respectively by using the values at the time t. Here, the fact that the block does not move below the initial position is taken into account.

$$\frac{d^2Z}{dt^2}_{(t+\Delta t)} = \begin{cases} \dfrac{F_{Z(t+\Delta t)}}{m} & \text{if } Z_{(t)} \neq 0 \\ \max\left(\dfrac{F_{Z(t+\Delta t)}}{m}, 0\right) & \text{if } Z_{(t)} = 0 \end{cases}, \tag{3.4}$$

$$\frac{dZ}{dt}_{(t+\Delta t)} = \begin{cases} \frac{dZ}{dt}_{(t)} + \frac{d^2Z}{dt^2}_{(t)} \Delta t & \text{if } Z_{(t)} \neq 0 \\ \max\left(\frac{dZ}{dt}_{(t)} + \frac{d^2Z}{dt^2}_{(t)} \Delta t, 0 \right) & \text{if } Z_{(t)} = 0 \end{cases}, \tag{3.5}$$

$$Z_{(t+\Delta t)} = \max\left(Z_{(t)} + \frac{dZ}{dt}_{(t)} \Delta t, 0 \right). \tag{3.6}$$

The initial conditions are given as follows:

$$\frac{d^2Z}{dt^2}_{(t=0)} = 0, \quad \frac{dZ}{dt}_{(t=0)} = 0, \quad Z_{(t=0)} = 0. \tag{3.7}$$

The position of the block in the normal direction of the slope is obtained by solving the above equations sequentially from t = 0. Fig. 3.20 shows an example of calculated results. In this case, no lifting-up was observed for armor block B because the total force F_Z did not exceed 0. On the other hand, the block without holes was lifted 61 mm.

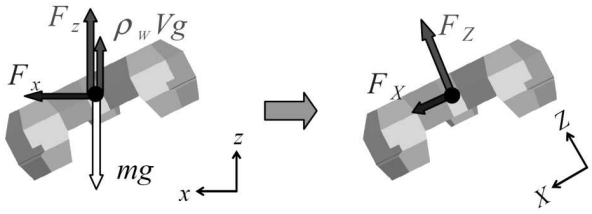

Figure 3.19 : Coordinate system used for the estimation of the amount of lifting-up.

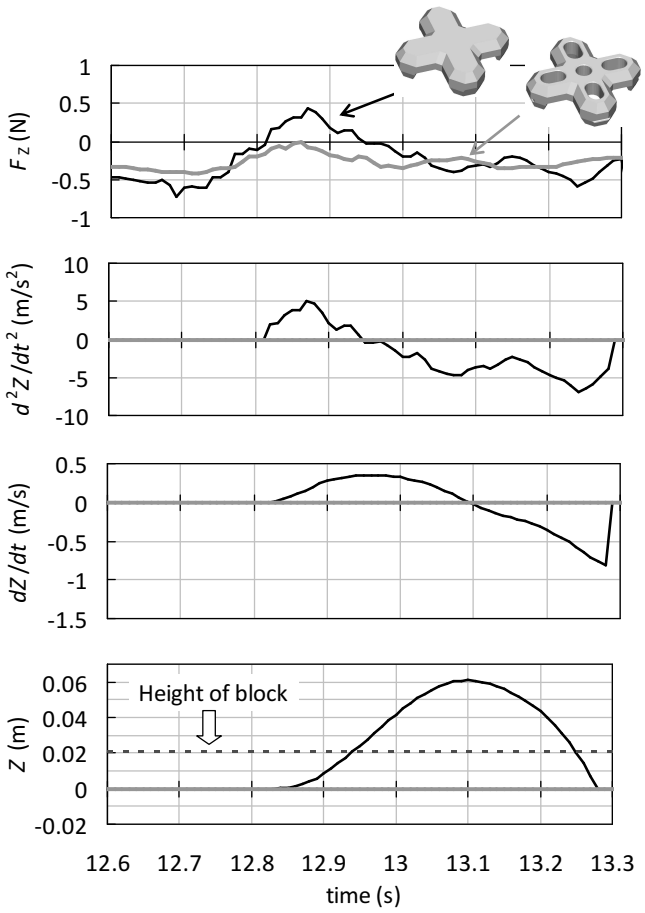

Figure 3.20 : Example of the calculation result of the lifting-up of the block.

By using this method, the stability of armor units was predicted. The amount of lifting-up was analyzed in the cases shown in Table 3.3 and compared to the experimental results. Armor block A was used in Cases 1 and 2, while armor block B was used in Case 3. The results are shown in Fig. 3.21. In the experiments, the damage occurred at the slope section in Cases 1 and 2. Also in the calculations, lifting-up above the height of the block occurred in these cases. On the other hand, in Case 3, damage did not occur in the experiment. Similarly, lifting-up of the block did not occur in the calculation. It can be said that the numerical computation agreed with the experimental results qualitatively. However, the position of the damage obtained by the numerical computation was different from the experimental results. Therefore in the future, the applicability of this model will have to be improved.

Table 3.3 : Analyzed cases of the lifting-up of blocks.

	Armor unit	Mass	Arrangement method
Case 1	Armor block A	244 g	2 units in the crown section
Case 2	Armor block A	130 g	2 units in the crown section
Case 3	Armor block B	65 g	2 units in the crown section

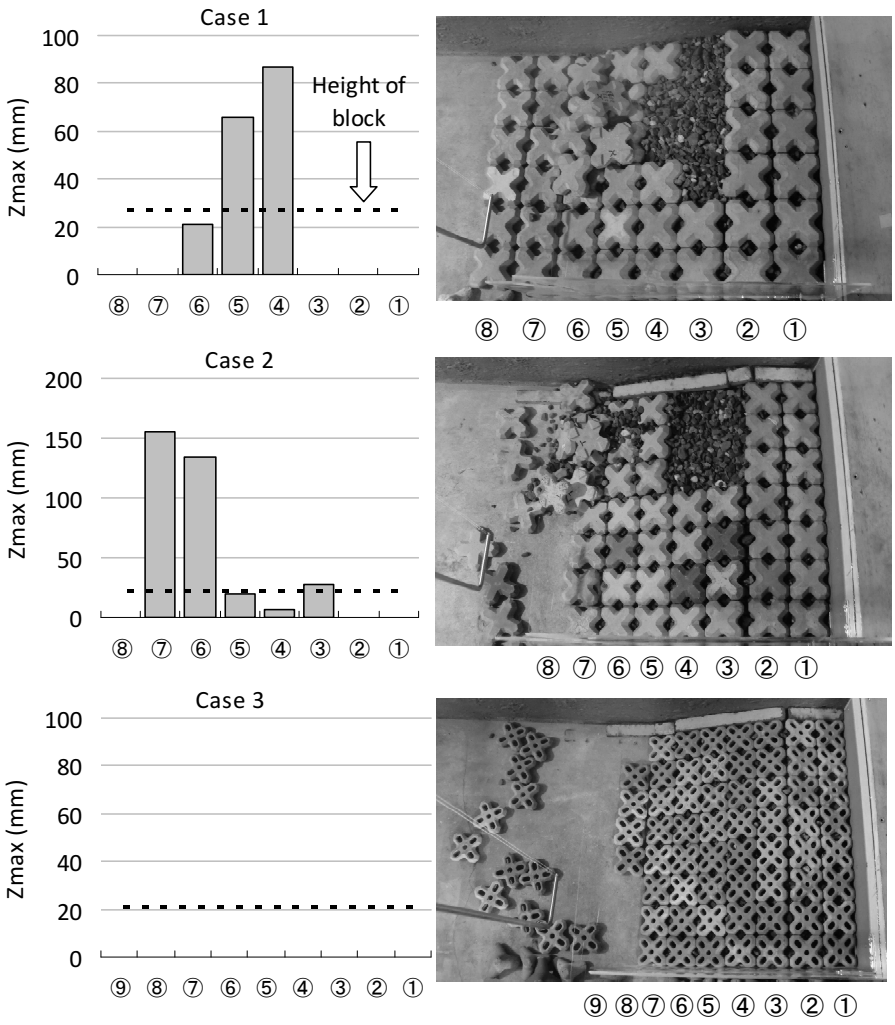

Figure 3.21 : Comparison of experimental and numerical damage to the armor blocks.

3.5 Closure

This chapter presented the findings of the hydraulic model experiments and numerical analysis on the stability of various types of armor units against overtopping jet caused by a tsunami with rapid water level rise. The main conclusions are shown below:

1. When the tsunami with rapid water level rise overtopped the breakwater and

impinged onto the harbor-side water surface, the water jet generated vortices. The armor units received uplift forces when the vortex passed through above the armor units.

2. Armor stones were easily removed by the overtopping jet of tsunami.
3. Damage to armor units was dependent on the position of jet impact.
4. The flat-type armor block with large holes showed high stability against the water jet in the experiments. Numerical analysis revealed that the holes in the blocks reduce the uplift force acting on the block and improve the stability against an impinging water jet.
5. Reinforcement by placing the heavier blocks along the toe of the slope enhanced the total stability of the armor layer.
6. The wave profile of the tsunami and the impinging jet were accurately reproduced by numerical computation based on the VOF method.
7. The stability of the armor blocks was predicted qualitatively by numerical analysis which took the 3-dimensional shape of the block into account.

Since the present study in this chapter is a first step in the understanding of armor stability against tsunami overflow, the results may be limited to particular cases. Therefore, further studies should be conducted especially with respect to the following points. Firstly, the influence of the period of the tsunami (or duration of the overflow) on stability should be investigated. The period of the tsunami was not varied in this study partly because of the limitation of the stroke of the wavemaker. Also, the influence of the shape of tsunami, for example, the breaking bore, or a tsunami with soliton fission, should be examined. The influence of the dimensions of the harbor-side mound and the harbor-side water level will also be important for armor stability.

References

Coastal Engineering Research Center (1977) : Shore Protection Manual, U.S.Army Corps of Engrs., U.S.Govt. Printing Office, Vol. II, 7_213-7_216.

Engelund, F. (1953) : On the laminar and turbulent flows of ground water through homogeneous sand, *Transactions of the Danish Academy of Technical Sciences*, Vol. 3, No. 4.

Fisheries Agency of Japan, Fisheries Infrastructure Department (2014) : Basic co

ncept of the countermeasures against earthquakes and tsunamis in the fishery port facilities after the 2011 Great East Japan Earthquake, Jan. 2014, http://www.jfa.maff.go.jp/j/seibi/gyokogyojo/pdf/pdf/gyo-jishintsunami-kangaekata140123.pdf (*in Japanese*), (accessed 2014-12-18).

Hamaguchi, M., Kubota, S., Matsumoto, A., Hanzawa, M., Yamamoto, M., Moritaka, H., Shimosako, K. (2007) : Hydraulic stability of new flat type armor block with very large openings for use in composite breakwater rubble mound protection, *Proceedings of Coastal Structures 2007*, Venice, Italy, 116-127.

Hanzawa, M., Matsumoto, A., Tanaka, H. (2012) : Stability of wave-dissipating c oncrete blocks of detached breakwaters against tsunami, *Proceedings of 33rd International Conference on Coastal Engineering*, Santander, Spain.

Higashiyama, K., Hasegawa, I., Inagaki, S. (2013) : Study of harbor side mound scouring by tsunami overflow, *Journal of JSCE, Ser. B3* (*Ocean Engineering*), **69** (2), I_377-I_382 (*in Japanese*).

Iwasaki, T., Mano, A., Nakamura, T., Horikoshi, N. (1984) : Experimental study on hydraulic force acting on mound and pre-packed caisson of submerged breakwater under steady flows, *Proceedings of the 31st Japanese Conference on Coastal Enginiiring*, 527-531 (*in Japanese*).

Jasak, H., Tukovic, Z. (2007) : Automatic meth motion for the unstructured finite volume method, *Transactions of FAMENA*, **30 (2)**, 1-18.

Kashima, H., Hirayama, K. (2013) : Model experiments and numerical simulations on tsunami with soliton fission in Kuji harbor, *Journal of JSCE, Ser. B3* (*Ocean Engineering*), **69** (2), I_694-I_699 (*in Japanese*).

Kondo, H., Takeda, H. (1983) : Wave dissipating structures, Morikita Publishing Co. Ltd., 275p (*in Japanese*).

Kubota, S., Hamaguchi, M., Matsumoto, A., Hanzawa, M., Yamamoto, M. (2008) : Wave force and stability of new flat type concrete block with large openings for submerged breakwaters, *Proceedings of 31st International Conference on Coastal Engineering*, Hamburg, Germany, 3423-3435.

Ministry of Land, Infrastructure, Transport and Tourism of Japan, Ports and Harb ours Bureau (2013) : Guidelines for Tsunami-Resistant Design of Breakwaters, Sept. 2013, http://www.mlit.go.jp/common/001012142.pdf (*in Japanese*), (acce ssed 2014-12-18).

OpenFOAM, http://www.openfoam.com/

Sakakiyama, T., Matsuyama, M. (2011) : Experimental study on stability of armor units of rubble mound breakwater against tsunamis, *Journal of JSCE, Ser. B2* (*Coastal*

Engineering), **67**, 791-795.

Takahashi, S., et al. (2011) : Urgent survey for 2011 Great East Japan Earthquake and Tsunami disaster in ports and coasts, *Technical Note of Port and Airport Research Institute*, No. 1231, 200p (*in Japanese*).

Tanimoto, K., Kimura, K., Miyazaki, K. (1988) : Study on stability of submerged dike at the opening section of tsunami protection breakwaters, *Report of Port and Harbour Research Institute*, **27** (4), 93-121 (*in Japanese*).

Chapter 4

Stability of Armor Units Covering Rubble Mound of Composite Breakwaters against Steady Overflow of Tsunami

4.1 Introduction

In the previous chapter, the armor stability was examined focusing on the initial impact of an overtopping jet caused by a tsunami with rapid water level rise. The appropriate shape of armor units against the impinging jet was presented and an improvement method of the structure for enhancing the stability was also presented.

It is required to clarify the stability of armor units for a wide range of conditions when developing a design method for armor units against tsunami overflow. As the conditions of the tsunami, it is necessary to consider the situation where the overflow continues for the long time of several minutes to several tens of minutes, which was observed during the Great East Japan Earthquake in 2011.

In this chapter, the armor stability is examined against a steady overflow of tsunami. A wide range of conditions of hydraulic model experiments are conducted to clarify the key factors affecting the armor stability. A numerical computation method is investigated to reproduce the flow field behind the breakwater during the steady overflow. The failure mechanism of armor units is then investigated by numerical analysis.

4.2 Hydraulic Model Experiment on Armor Stability

4.2.1 Experimental Method

4.2.1.1 Experimental equipment

Experiments were conducted in a 50 m long, 1.0 m wide, and 1.5 m deep wave flume. Fig. 4.1 shows the schematic layout of the flume. A horizontal mortar seabed was partitioned into two sections along the length, and a breakwater model was installed in one 50 cm wide waterway. A submersible pump and discharge port were located on the harbor-side and sea-side of the breakwater model respectively to generate a steady overflow. The capacity of the pump was 4 m^3/min. A water level difference was generated between the inside and outside of the breakwater by operating the pump. The height of the sea-side water level could be changed by varying the height of the overflow weir installed on the sea-side of the breakwater model. The height of the overflow weir could be varied in a range of 0 to 50 cm. A vent hole with a diameter of about 25 mm was provided in the partition wall close behind the caisson as shown in Fig. 4.2 to maintain the space between the caisson and the overflow nappe in ambient atmospheric pressure conditions.

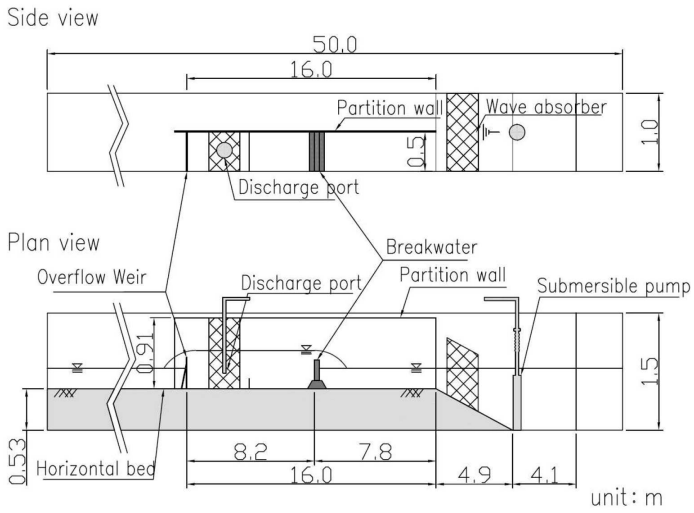

Figure 4.1 : Schematic layout of the wave flume.

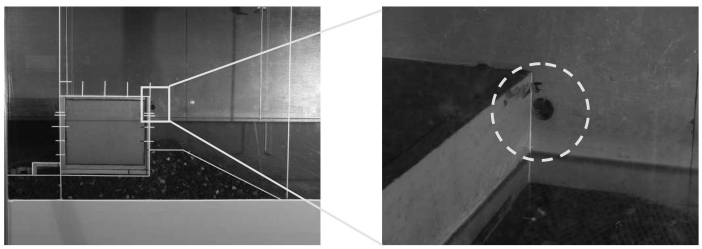

Figure 4.2 : Vent hole provided in the partition wall.

4.2.1.2 Breakwater cross section

An example of the cross section of the breakwater is shown in Fig. 4.3. The model scale was 1/50. Experiments were conducted by changing the shape of the harbor-side rubble mound, the harbor-side water level, and the shape and mass of the armor units. Two kinds of flat-type armor blocks and wave-dissipating blocks as shown in Table 4.1 were used. The caisson model was made of wood and was fixed with a weight so that it would not move through tsunami action since this study was focused on the stability of the armor units.

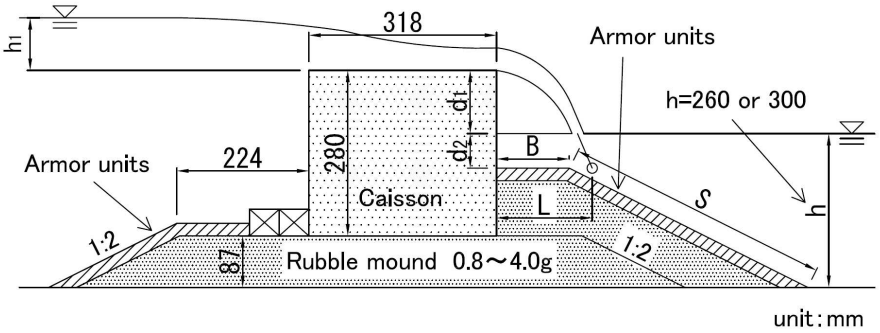

Figure 4.3 : Example of the cross-section of the breakwater.

Table 4.1 : Armor units used in the experiments. Values in brackets represent the converted values to the prototype scale.

Armor unit	Mass
Flat-type armor block A 	17 g (2.2 t)
	35 g (4.4 t)
	64 g (7.6 t)
	136 g (16.9 t)
	254 g (31.7 t)
Flat-type armor block B 	16 g (2.0 t)
	33 g (4.1 t)
	64 g (8.0 t)
	123 g (15.4 t)
Wave-dissipating block 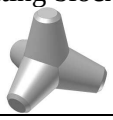	61 g (7.6 t)
	122 g (15.3 t)
	235 g (29.4 t)
	637 g (79.7 t)

4.2.1.3 Tsunami conditions

The duration time of the steady overflow of tsunami was set to 127 s (15 minutes in the prototype scale). The duration times at the typical breakwaters during the Tohoku tsunami on March, 11th in 2011 computed by the STOC model (Tomita and Kakinuma, 2005) were 716 s at the North Breakwater at the Port of Hachinohe, 123 s at the

Offshore Breakwater at the Port of Sendai-Shiogama, and 328 s at the Offshore Breakwater at the Port of Soma, according to Higashiyama et al. (2013). Compared to these, the duration time of this study is rather long setting.

4.2.1.4 Calibration method for tsunami

Prior to conducting the stability tests, the water levels inside and outside of the breakwater in steady state were examined. The water levels were measured at the 3 locations on the sea-side and the 3 locations on the harbor-side as shown in Figure 4.4. The height of the overflow weir and the initial water level were determined so that the sea-side and harbor-side water levels in steady state coincided with the target values. The water levels at WG1 (2 m on the offshore side from the front of the caisson) and WG5 (2 m on the onshore side from the rear end of the caisson) were used for matching by considering the spatial uniformity. As it took about 60 s until the water level achieved a steady state from the start of operating the pump, the total operation time of the pump was set to 187 s (= 127 s + 60 s).

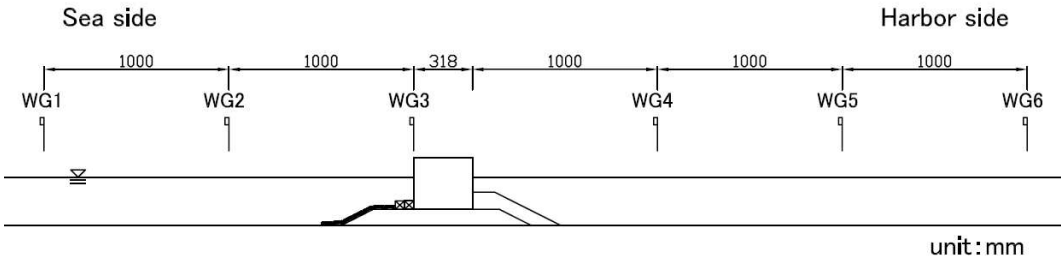

Figure 4.4 : Measurement locations of water level.

4.2.1.5 Method for the stability tests

The stability limits of the armor units were examined by increasing the overflow depth in increments of 1 cm (0.5 m in the prototype scale). The overflow depth was defined as the difference between the sea-side water level and the crest height of the caisson. The section was not rebuilt after tsunami attack with each overflow depth. The number of the moved armor units was counted as an accumulated number. The damage to armor units were defined using the relative damage N_0 (Van der Meer, 1988), which is the actual number of displaced units related to the width of one nominal diameter D_n. The nominal diameter D_n is the cube root of the volume of the armor unit. In this study, N_0 = 0.3 was applied as the criterion of damage.

4.2.2 Experimental Result

4.2.2.1 Feature of the damage by tsunami overflow

Figure 4.5 shows snapshots of the tsunami overflow in the experiment. As soon as the armor blocks on the slope section were washed away, scouring of the rubble mound progressed rapidly and reached to the sea bottom within about 1 minute (7 minutes in the prototype scale). Though the widened protection using additional stones exhibits a function to delay scouring, the damage expands rapidly if the armor units are washed away and the rubble mound is exposed. This is one of the features of damage by tsunami overflow. This also suggests the importance of accurate estimation of the armor stability.

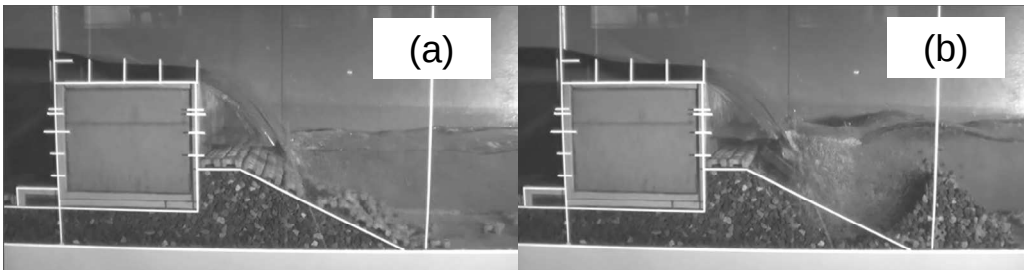

Figure 4.5 : Snapshots of tsunami overflow. (a) : 27 seconds after the beginning of overflow. (b) : 87 seconds after the beginning of overflow.

4.2.2.2 Influence of harbor-side water level

The impingement position of the overflow jet will change with various factors such as the shape of the harbor-side mound and the overflow depth. The influence of the impingement position on armor stability was examined by changing the crown width of the harbor-side mound. Fig. 4.6(a) shows an example of the stability test results. In this condition, the overflow jet impinged on the slope section when the number of armor units on the crown section was one or two, whereas it impinged on the crown section in the case of more than four units on the crown section. The cases in which the jet impinged on the slope section showed higher stability than the cases of impingement on the crown section. This shows that the impingement position largely affects the armor stability. The effect of the impingement position depended on the structural conditions such as the shape of the armor units and the presence or absence of widened protection. Thus, it is necessary to incorporate properly this effect into the estimation of the armor stability.

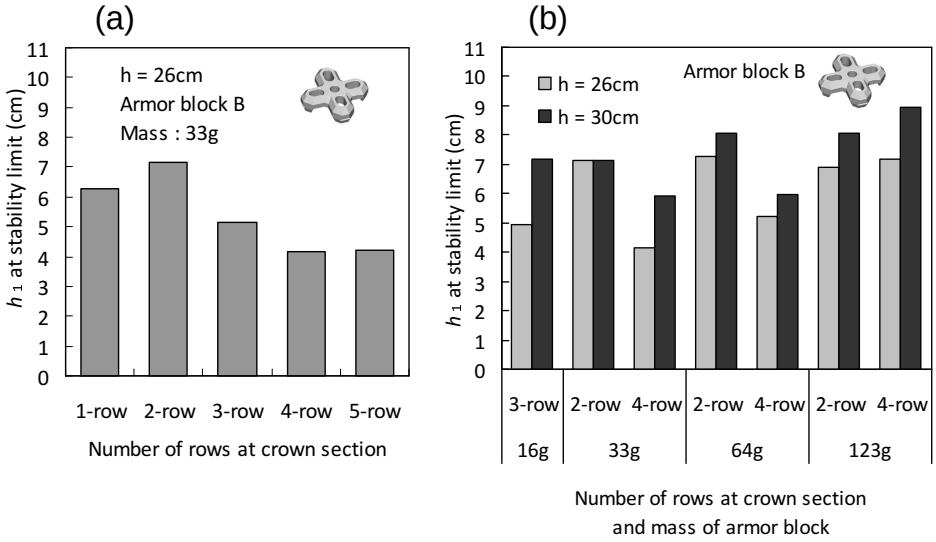

Figure 4.6 : (a) : Influence of impingement position on the overflow depth at stability limit. (b) Influence of harbor-side water level on the overflow depth at stability limit.

4.2.2.3 Influence of harbor-side water level

When a tsunami overflows the caisson, the discharged water from the rear end of the caisson accelerates during the freefall above the water surface, and decelerates under the water surface due to diffusion. Therefore, the stability of armor units should decrease as the crown height of the caisson above the harbor-side water level increases. Also, it should increase as the submerged depth above the armor units increases. Fig. 4.6(b) shows a comparison of the stability test results with two different harbor-side water levels. On the whole, the results of deep-water cases showed higher stability than those of shallow-water cases.

4.2.2.4 Failure modes of armor units

Two failure modes for flat-type armor blocks were observed in the experiments. One was an overturning mode in which armor blocks near the impingement position overturned. The other was a sliding mode in which all the blocks on the slope section slid together. Fig. 4.7 shows the relationship between the nominal diameter of the armor block D_n and the overflow depth h_1 at the occurrence of damage. In the cases of overturning mode, overflow depth at the occurrence of damage was almost proportional to the nominal diameter D_n. On the other hand, in the cases of sliding mode, it had only small dependence on D_n. These results suggest that enlargement of the block size causes an increase in the acting force as much as the increase in the resistance force with regard to the sliding mode. For the wave-dissipating blocks, almost every failure pattern was

that of blocks near the impingement position being displaced individually.

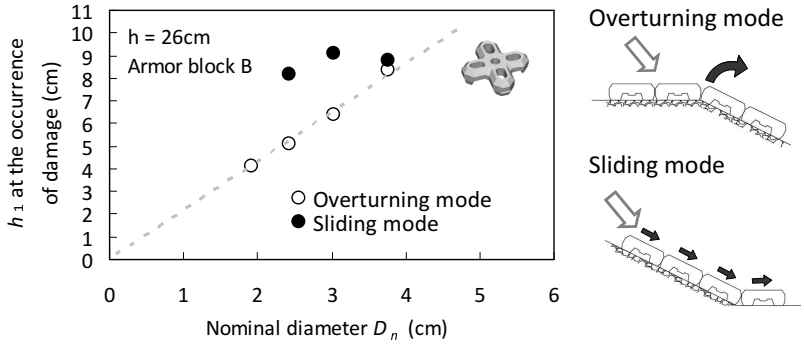

Figure 4.7 : Relationship between the nominal diameter and the overflow depth at the occurrence of damage by each failure mode.

4.2.2.5 Performance of the wave-dissipating concrete blocks

A characteristic of the wave-dissipating blocks installed in the two layers is that scouring is hard to progress rapidly even when many blocks displaced. Fig. 4.8 shows an example of the experimental result. The blocks of mass 122 g were placed in two layers. The damage began to occur at h_1 = 6 cm. At h_1 = 7 cm, no scouring occurred though a lot of blocks fell down. At h_1 = 8 cm, The deformation of the mound was slight though the damage to the blocks progressed. Wave-dissipating blocks are considered to have such a toughness for the following reasons: (1) It takes a longer time before the rubble stones are exposed since they are covered with two layers. (2) Displaced blocks piled up behind the impingement position prevent the progress of the scouring by staying interlocked without being washed away. Avoiding the rapid progress of scouring is important from the viewpoint of resilience of a breakwater in the prevention of large scattering of the caisson (Arikawa et al. 2013). The widened protection mound covered with wave-dissipating blocks may provide such resilience.

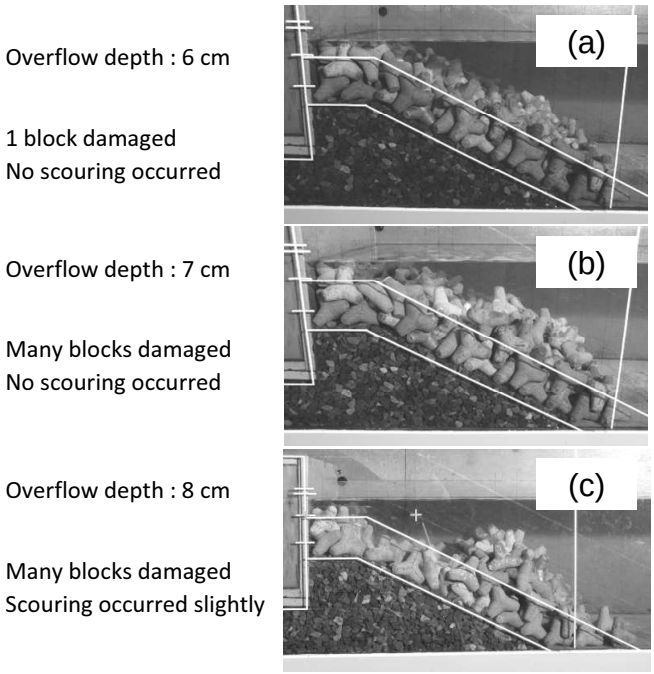

Figure 4.8 : Example of the progress of damage in the case of wave-dissipating blocks placed in two layers. The blocks of mass 122 g were used.

4.3 Numerical Analysis on Tsunami Overtopping Caisson

As mentioned above, two failure modes were observed in the experiments. The failure mechanism was investigated in detail by numerical analysis. First, the computation method of the flow field at the harbor-side of the breakwater was investigated. The method was validated by comparing the measured and computed flow field. The stability of the armor units was then investigated by computing the hydrodynamic force acting on each armor unit.

4.3.1 Numerical Analysis Method

With regard to the numerical computation of the tsunami overtopping the caisson, the VOF method implemented in the OpenFOAM model adequately reproduced the laboratory experiment of a tsunami generated by a wavemaker as described in Chapter 3. In the case of the steady overflow of tsunami, however, computation results using the volume of fluid (VOF) method did not reproduce well due to the excessive entrainment of air into the impinging jet as shown in Fig. 4.9. Bricker et al. (2013) pointed out that this model overestimates the eddy viscosity at the air-water interface, and that it can be improved by neglecting all the turbulence in the air phase. In this study, the overflow jet

above the water surface and the flow field on the harbor-side were solved separately as shown in Fig. 4.10 to avoid excessive entrainment of air.

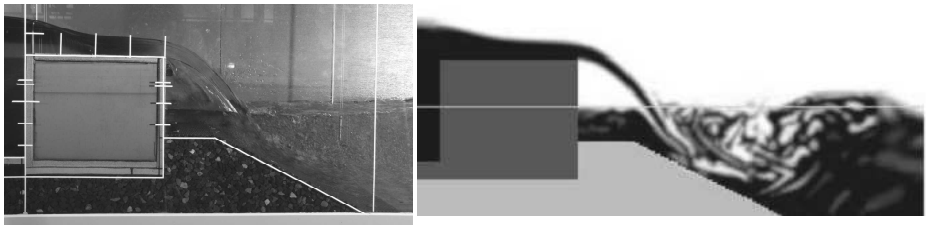

Figure 4.9 : Preliminary computation result by the VOF method. (Left) : Experiment. (Right) : Computation.

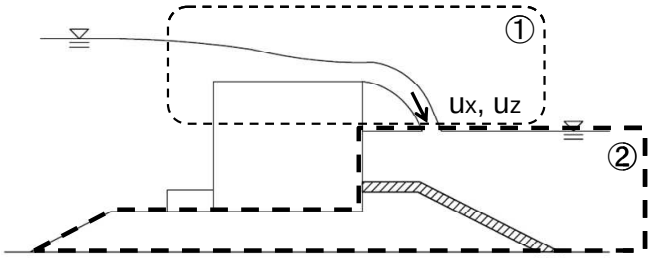

Figure 4.10 : Schematic diagram of the numerical analysis method.

4.3.1.1 Calculation method for the overflow nappe based on empirical formulae

Two methods were examined for the calculation of the overflow nappe above the water surface. One is a simple method based on some empirical formulae, the other is the numerical method based on the VOF model. The former has an advantage that the calculation done immediately though the applicability is limited to rectangular caissons. The latter is suited to caissons with complicated shapes.

Firstly, the simple method using empirical formulae is shown below. The definition of each symbol is shown in Fig. 4.11. The overflow discharge per unit width q is calculated by using the Hom-ma formula (Hom-ma, 1940b):

$$q = 0.35 h_1 \sqrt{2 g h_1}\ , \tag{4.1}$$

where, h_1 is the overflow depth, g is the gravitational acceleration. The applicable condition of this formula is $h_1/B_c < 1/2$. The effect of the approaching velocity u_1 can be disregarded if $h_1/h_d < 0.5$ (Hom-ma, 1940a). The water depth above the caisson at the rear end of the caisson h_2 and the cross sectional averaged flow velocity u_2 are calculated according to Hom-ma (1940a) as shown below.

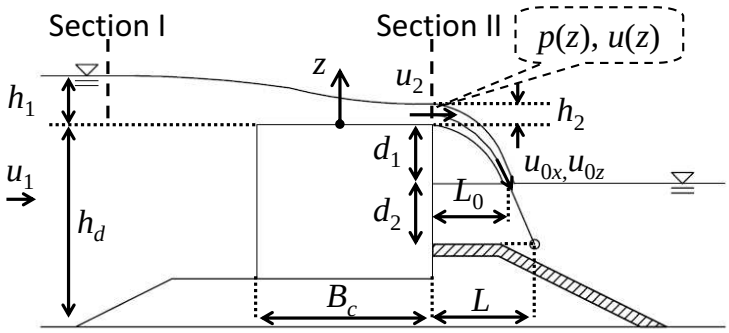

Figure 4.11 : Definition of the symbols used in the calculation of the overflow nappe based on empirical formulae.

Applying the Bernoulli's theorem to Sections I and II yields the following relation:

$$h_1 = z + \frac{p_{(z)}}{\rho g} + \frac{u_{(z)}^2}{2g}, \tag{4.2}$$

where, z is the height measured from the top of the caisson, $p_{(z)}$ is the pressure, and $u_{(z)}$ is the flow velocity. The overflow discharge q is obtained by integrating the flow velocity $u_{(z)}$ as follows:

$$q = \int_0^{h_2} \sqrt{2g\left(h_1 - z - \frac{p_{(z)}}{\rho g}\right)}\,dz\,. \tag{4.3}$$

If the pressure distribution $p_{(z)}$ is given, h_2 can be calculated using Eq. (4.1) and (4.3). The pressure distribution is assumed as the following triangular distribution:

$$\begin{aligned} p(z) &= \rho g(h_2 - z) \quad \text{for} \quad h_2/2 \le z \le h_2 \\ p(z) &= \rho g z \quad \text{for} \quad 0 \le z \le h_2/2 \end{aligned}. \tag{4.4}$$

This means that hydrostatic pressure is assumed between the water surface and $z = h_2/2$ and that the pressure decreases linearly to the atmospheric pressure at the bottom. Using Eq. (4.1), Eq. (4.3), and Eq. (4.4), the following equation is obtained:

$$0.35h_1\sqrt{2gh_1} = \sqrt{2g}\left\{-\frac{1}{3}\left[\sqrt{(h_1 - h_2)^3} - \sqrt{h_1^3}\right] + \sqrt{h_1 - h_2}\,\frac{h_2}{2}\right\}. \tag{4.5}$$

The relationship between h_1 and h_2 is solved numerically with Newton's method as follows:

$$h_2 = 0.42h_1\,. \tag{4.6}$$

If another pressure distribution $p_{(z)}$ is assumed as shown in Eq. (4.7), the relationship

between h_1 and h_2 is calculated as shown in Eq. (4.8).

$$\begin{aligned} p(z) &= \rho g(h_2 - z) \quad \text{for} \quad 2h_2/3 \le z \le h_2 \\ p(z) &= \rho g z \quad \text{for} \quad 0 \le z \le 2h_2/3 \end{aligned}, \tag{4.7}$$

$$h_2 = 0.44h_1 . \tag{4.8}$$

In this study, the following relationship was used considering its suitability to the experimental results:

$$h_2 = 0.45h_1 . \tag{4.9}$$

The center of trajectory of the overtopped water was then obtained under the following assumptions:

(1) The overtopped water discharges horizontally from the rear end of the caisson at the flow velocity $u_2 = q / h_2$.

(2) The trajectory of the overflow nappe above the water surface is a parabola.

The landing position of the overtopped water on the harbor-side water surface, L_0, and the flow velocity u_{0x}, u_{0z} are calculated as follows:

$$L_0 = u_2\sqrt{\frac{2(d_1 + h_2/2)}{g}} , \tag{4.10}$$

$$u_{x0} = u_2, \quad u_{z0} = \sqrt{2g(d_1 + h_2/2)} . \tag{4.11}$$

The width of the water jet at the harbor-side water surface, h_0, is calculated as:

$$h_0 = \frac{q}{u_{z0}} . \tag{4.12}$$

4.3.1.2 Calculation method for the overflow nappe based on the VOF method

As the simple method mentioned above is applicable only to rectangular caissons, the numerical method based on the VOF model should be used in the cases of caissons with complicated shapes. Fig. 4.12 shows a schematic diagram of the calculation method for the overflow nappe based on the VOF model. The overflow is generated by water flowing into the computational domain from the offshore bottom boundary. In this method, the flow rate needs to be determined by trial and error as the offshore water level matches the target value.

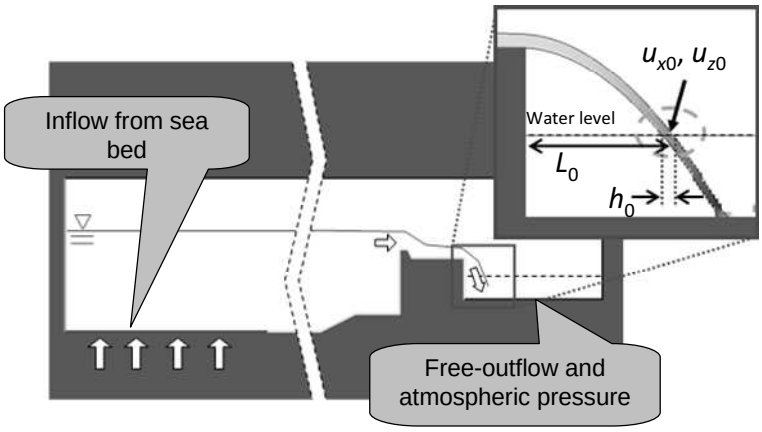

Figure 4.12 : Schematic diagram of the calculation method for the overflow nappe based on the VOF model.

4.3.1.3 Calculation method for the flow field under the water surface

The flow field under the water surface on the harbor-side was solved by a single-phase numerical model. An incompressible flow solver within the OpenFOAM was used. The governing equations were the Reynolds-Averaged Navier-Stokes (RANS) equation and the continuity equation. The Finite Volume Method with an unstructured grid was used to reproduce the complicated shape of the armor blocks. Fig. 4.13 shows the schematic diagram of the computational method. The landing position of the overtopped water L_0 and the flow velocity u_{0x}, u_{0z} at the harbor-side water surface were given as boundary conditions. These values were obtained by preliminary calculation as mentioned above. The water surface on the harbor-side was assumed as a fixed boundary.

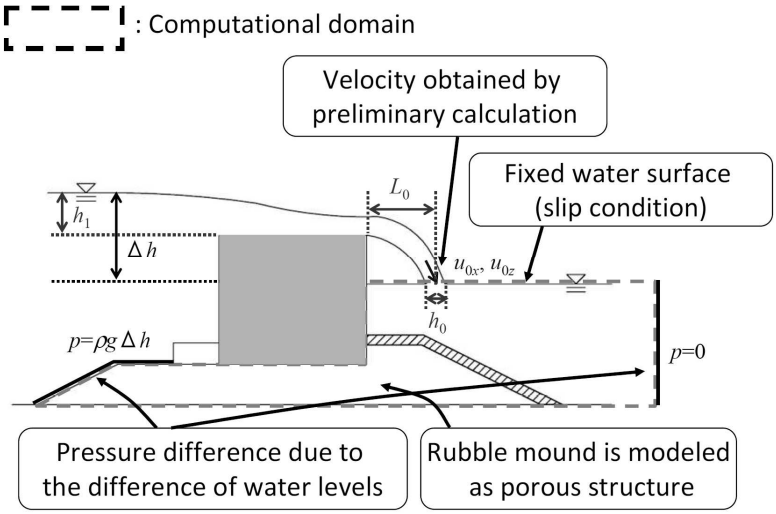

Figure 4.13 : Schematic diagram of the computation method for the flow field under the water surface.

The rubble mound was modeled as a porous structure to reproduce the seepage flow under the caisson. The pressure difference due to the water level difference between the inside and outside of breakwater was given at both ends of the computational domain. The hydraulic flow resistance **R** in the porous medium was expressed by a D-F relationship as shown below:

$$\mathbf{R} = -\left(\alpha\mathbf{U} + \beta|\mathbf{U}|\mathbf{U}\right), \tag{4.13}$$

where, **U** is the flow velocity vector, α is the laminar resistance coefficient, and β is the turbulent resistance coefficient. These coefficients were expressed using the empirical formulae from Engelund (1953) as follows:

$$\alpha = \alpha_0 \frac{(1-n)^3}{n^2}\frac{\nu}{d^2}, \quad \beta = \beta_0 \frac{1-n}{n^3}\frac{1}{d}, \tag{4.14}$$

where, ν is the kinematic viscosity of water, d is the characteristic diameter of the stone, n is the porosity, and α_0 and β_0 are the material constants. The material constants were investigated in the preliminary experiment. The relationship between the pressure difference and the discharge of the seepage was obtained in the experiment, and the constants were determined as α_0 = 2100 and β_0 = 1.5. The characteristic diameter d and the porosity n are determined by measurement as d = 0.0115 m and n = 0.39, respectively.

The computation of the flow field was conducted in cross-sectional 2-dimensions. The standard grid size was set to 2 mm. In the cases of computing the hydrodynamic forces acting on the armor blocks, the grid was subdivided into 3-dimensions. The grid size around the block was set to about 1 mm so that the block shapes could be reproduced in detail.

A Reynolds stress model (RSM) by Launder et al. (1975) was used as a relatively high accuracy turbulence model among the RANS models, since the degree of diffusion of the impinging jet was influenced by the turbulence model. Also, there was a problem that excessive turbulence was generated on the surface of the rubble mound when the jet flowed along the rubble mound. In this study, the turbulence inside the rubble mound was set to zero as a countermeasure for this problem. These effects on flow field are discussed later.

4.3.2 Numerical Result of Flow Field of Harbor-side

The validity of this numerical method was confirmed by comparing the computed flow field of harbor-side with the measured one. The flow velocity in two axes (x and z) was

measured for 20 seconds using an electromagnetic current meter after the flow field became steady state. The average velocity for 20 seconds was compared with the computed value. Measurement was conducted using cross-sections in the presence or absence of the widened protection mound as shown in Fig. 4.14. The overflow depth was set to 5 cm and 9 cm. The vertical distribution of the horizontal component of flow velocity were compared at two measurement lines.

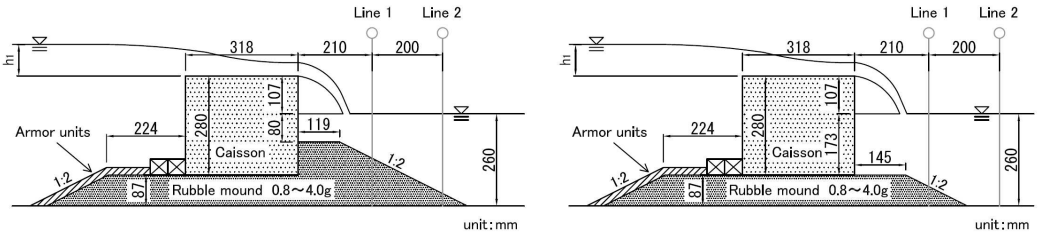

Figure 4.14 : Cross-sections of the breakwater used for the comparison of flow field. (Left) : With widened protection. (Right) : Without widened protection.

Table 4.2 shows the test cases. Case 0 is a standard case for comparison. The results of Case 1, Case 2, and Case 3 were compared with that of Case 0 to examine the influence of the calculation method on the overflow nappe, the influence of the turbulence model, and the influence of the modification of the turbulence model by removing turbulence inside the mound, respectively.

Table 4.2 : Test cases for the comparison of flow field.

	Calculation method for the overflow nappe	Turbulence model	Zero turbulence inside mound
Case 0	Empirical formula	RSM	On
Case 1	VOF method	RSM	On
Case 2	Empirical formula	Standard k-ε	On
Case 3	Empirical formula	RSM	Off

Fig. 4.15 shows a comparison of the results of Case 1 and Case 0 to examine the influence of the calculation methods for the overflow nappe. The flow fields of both Case 1 and Case 0 show good agreement with the measured values for all conditions. Therefore, both empirical formula and VOF method are applicable for the calculation of the overflow nappe.

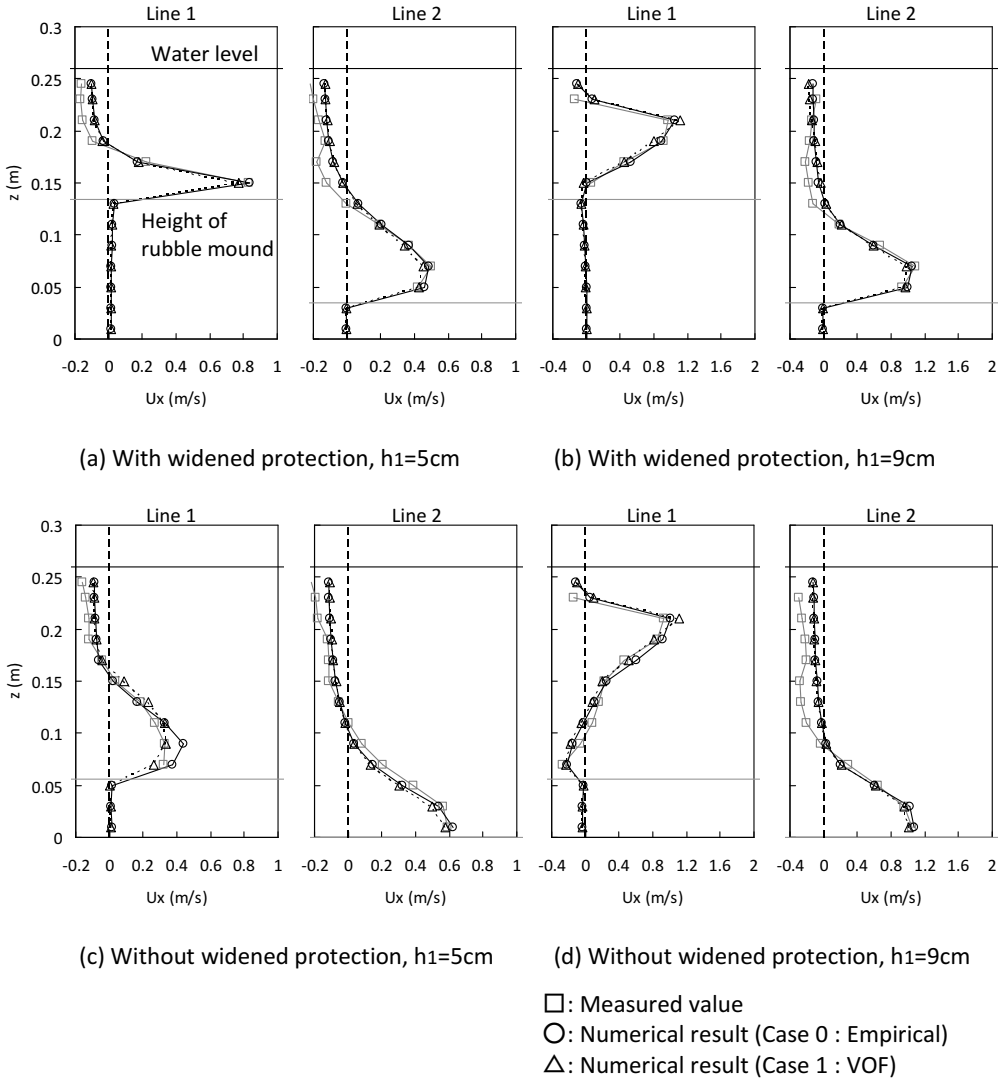

Figure 4.15 : Comparison of flow fields obtained by the different calculation methods for the overflow nappe.

Fig. 4.16 shows a comparison of the results of Case 2 and Case 0 to examine the influence of the turbulence models. Comparing the velocity on line 1 at the overflow depth of 5 cm, the RSM reproduces the peak value of the velocity and its position better than the standard k-ε model.

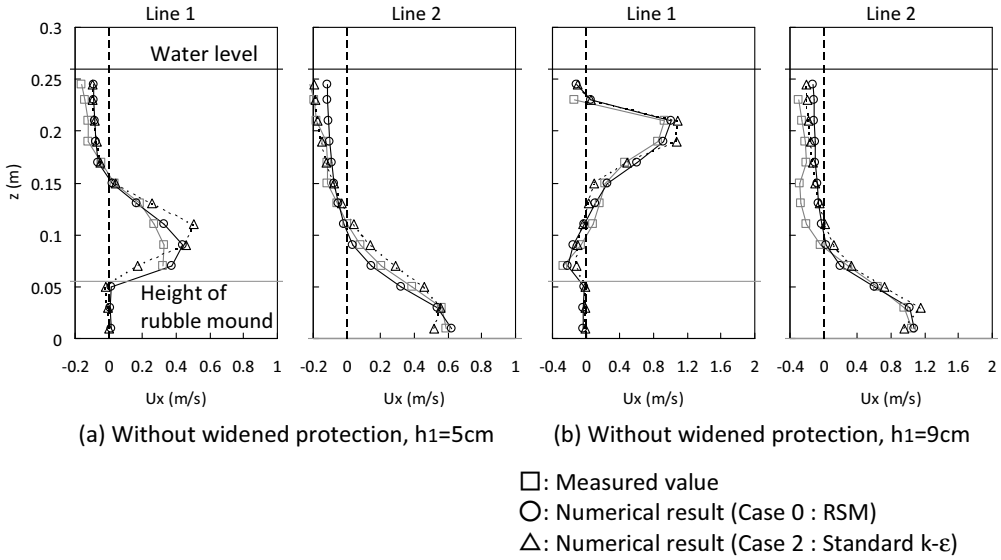

Figure 4.16 : Comparison of flow fields obtained by the different turbulence models.

Fig. 4.17 shows a comparison of the results of Case 3 and Case 0 to examine the influence of the modification of the turbulence model by removing turbulence inside the mound. In the case of no modification, the peak position of the flow locates away from the mound compared to the measured result. This suggests that the turbulence generated at the boundary of the mound is excessive. The modified model that the turbulence inside the rubble mound is set to zero favorably reproduces the water jet flowing along the mound.

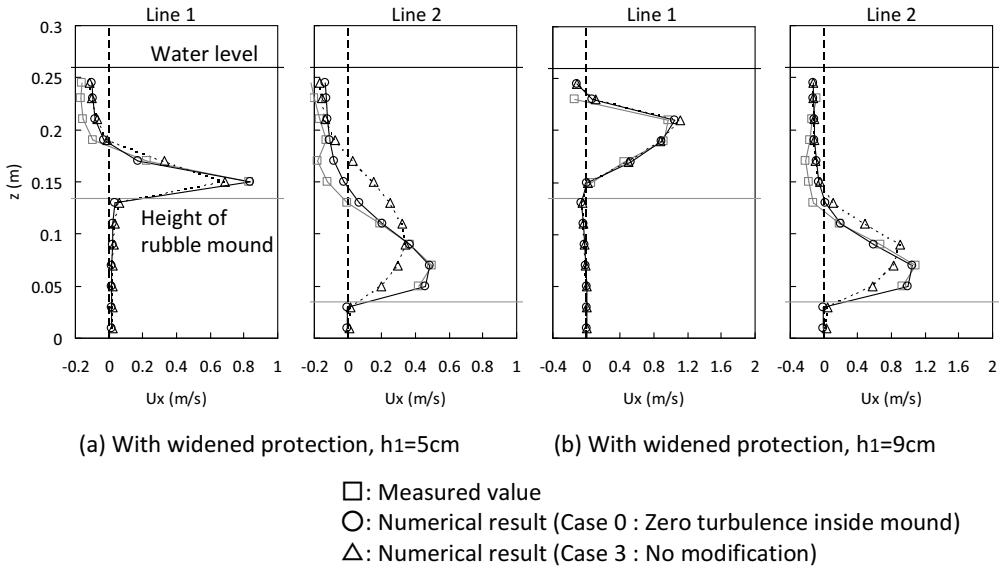

Figure 4.17 : Comparison of flow fields obtained by the presence or absence of the modification of the turbulence model by removing the turbulence inside mound.

4.4 Numerical Analysis on Stability of Armor Blocks

4.4.1 Analysis of Stability against Overturning

The stability of the armor blocks was analyzed based on the fluid force acting on each block. The fluid force was obtained by integrating the pressure around the block surface. An experimental case was selected where the overflow jet impinged on the shoulder of the mound. Fig. 4.18 shows the schematic layout of the breakwater selected for the analysis. The armor block A of mass 254 g was used. Fig. 4.19 shows the experimental results of this case. When the overflow depth was 5 cm, the blocks at the shoulder (block No. 3) were overturned. Fig. 4.20 shows the computed flow field and fluid force acting on each block. A large force is acting on the block at the shoulder (block No. 3). The stability of this block was judged by the balance of moment. In this analysis, only the fluid force, the buoyant force, and the self-weight were considered while other forces such as the friction force between blocks were disregarded. The condition of the occurrence of overturning was expressed as follows:

$$F_x a_H + F_z a_V + M_y > (\rho_r - \rho_w) V g a_V , \tag{4.15}$$

where, F_x is the horizontal hydrodynamic force, F_z is the vertical hydrodynamic force, M_y is the moment due to the hydrodynamic force, a_H and a_V are the arm length, ρ_w is the density of the water, ρ_r is the density of the block, and V is the volume of the armor block (see Fig. 4.21). The resistance moment, which is the right hand side of Eq. (4.15) was calculated to be 49.0 N·mm in this case. Meanwhile, the acting moment, which is the left hand side of Eq. (4.15), was calculated to be 42.4 N·mm when the overflow depth was 4 cm, and 54.8 N·mm when the overflow depth was 5 cm. Thus, this result agreed with the experimental one.

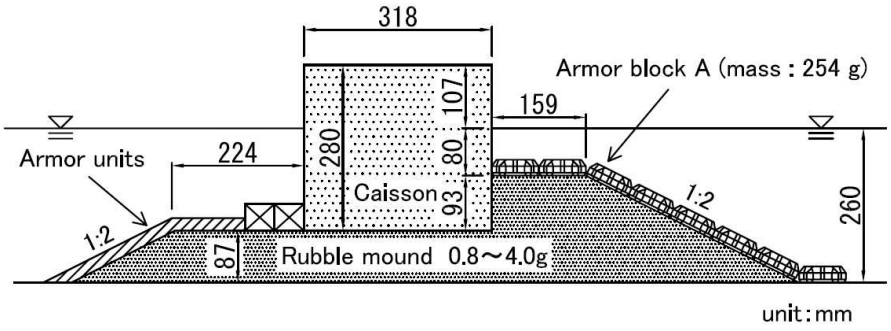

Figure 4.18 : Schematic layout of the breakwater for the analysis of armor stability against overturning mode.

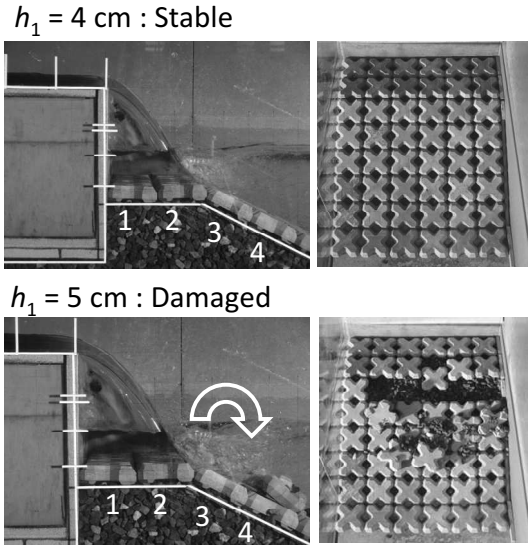

Figure 4.19 : Failure situation of the armor blocks in overturning mode. Armor blocks A of the mass 254 g were used.

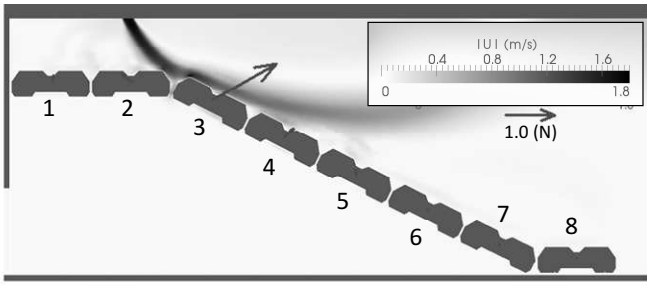

Figure 4.20 : Computed flow field and fluid force acting on each block. Overflow depth was 5 cm.

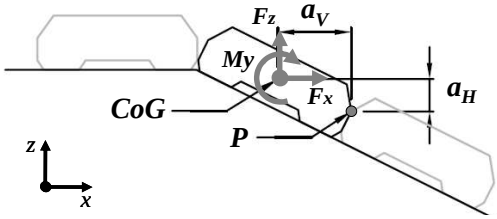

Figure 4.21 : Definition of the symbols used for the analysis of the balance of moment of the block.

Further validation is required, but this analysis suggested that the failure of the armor units in the overturning mode could be explained by the balance of the moment acting on the block.

4.4.2 Analysis of Stability against Sliding

The stability of armor blocks against sliding mode was examined. Firstly, a balance of force in the normal direction of the mound was considered for each block. The condition where the block lifts up was expressed as follows:

$$N_i > W' \cos\theta_i , \tag{4.16}$$

where, N_i is the fluid force in the normal direction acting on the i-th block, W' is the underwater weight of the block. If the block does not lift up, the difference between the left and right side of Eq. (4.16) becomes the reaction force from the mound, R_i.

A balance of the total tangential force of all the blocks located below the impingement position was then considered. The condition where the blocks slides was expressed as follows:

$$\sum_i \left(T_i + W' \sin\theta_i \right) > \sum_i \left(\mu_i R_i \right) \tag{4.17}$$

where, T_i is the fluid force in the tangential direction acting on the i-th block, μ_i is the friction coefficient. The resistance due to the interlocking between the block and stones was included in the friction force. The friction coefficient of each block was determined by tuning. The coefficient of the block at the toe of the mound was set to 0.6 regardless of the block shape as the block at the toe was placed on a mortar seabed in the experiments. The left and right side of Eq. (4.17) show the total sliding force and the total resistance force, respectively.

Fig. 4.22 shows an example of the schematic layout of the breakwater for the analysis. In this case, the armor blocks B of mass 33 g were used. The computed sliding force and resistance force of each block in the case of the overflow depth of 6 cm are shown in Table 4.3. A large force in the tangential direction of the mound was acting on block No.5 which was located near the impingement position of the overflow jet. Also, a large force was acting on block No. 11 which was located at the toe of the mound.

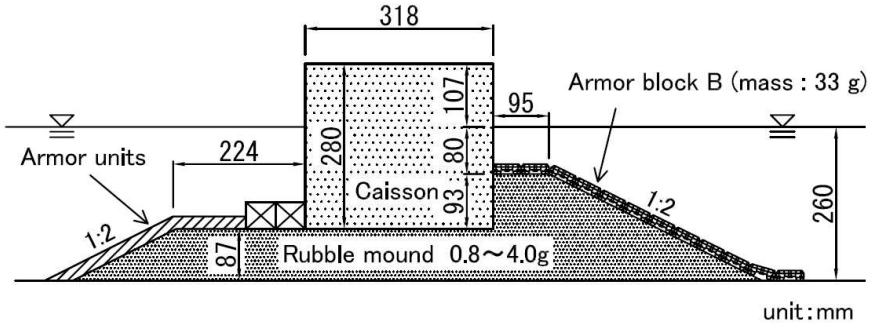

Figure 4.22 : Schematic layout of the breakwater for the analysis of armor stability against sliding mode.

Table 4.3 : Example of the computed sliding force and resistance force of each block. The armor blocks B of mass 33 g were used. The overflow depth was 6 cm.

No.	W' (N)	N_i (N)	T_i (N)	R_i (N)	μ_t	Sliding force (N)	Resistance force (N)
3	0.182	0.031	−0.046	0.132	1.0	0.035	0.132
4	0.182	−0.022	−0.027	0.185	1.0	0.055	0.185
5	0.182	0.027	0.266	0.136	1.0	0.347	0.136
6	0.182	0.088	0.143	0.074	1.0	0.224	0.074
7	0.182	0.049	0.060	0.114	1.0	0.142	0.114
8	0.182	0.019	0.016	0.144	1.0	0.097	0.144
9	0.182	0.005	−0.002	0.157	1.0	0.080	0.157
10	0.182	−0.005	−0.019	0.168	1.0	0.062	0.168
11	0.182	0.015	0.167	0.167	0.6	0.167	0.100

The stability of the armor blocks was investigated using these forces. The sliding forces were larger than the resistance forces for blocks No. 5 to No. 7 which were located near the impingement position. The sliding force on block No. 11 at the toe also exceeded the resistance force. The resistance forces were larger for the other blocks. Therefore, the stability against sliding should be judged by the balance of the total force of blocks No.5 to No. 10. The total sliding force was calculated to be 0.952 N and the total resistance force was calculated to be 0.753 N, which means sliding occurs in this calculation. Actually, blocks on the slope section did not slide in the experiment when the overflow depth was 6 cm, though the blocks at the toe slid. When the overflow depth was 8 cm, all the blocks below the impingement position slid together as shown in Fig. 4.23.

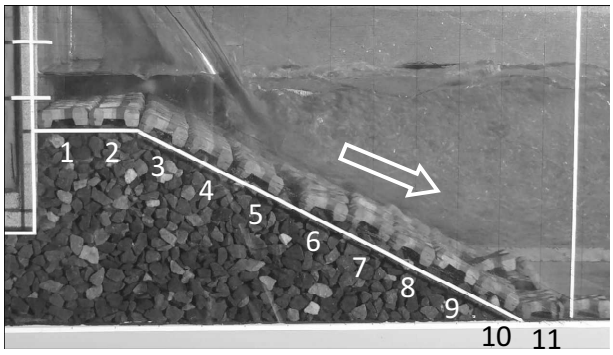

Figure 4.23 : Failure situation of the armor blocks in sliding mode. Armor blocks B of the mass 33 g were used. Overflow depth was 8 cm.

This analysis was conducted for many cases. Fig. 4.24 shows a comparison of the computed and experimented overflow depths at the occurrence of damage. The computed results almost agreed with the experimental ones. Therefore, this analysis suggested that the failure of the armor units in the sliding mode could be explained by the balance of the total force of the blocks on the slope section.

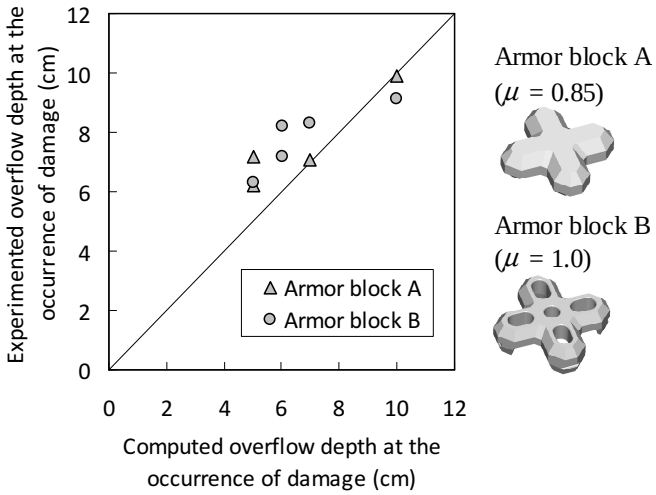

Figure 4.24 : Comparison of the computed and experimented overflow depth at the occurrence of damage.

4.5 Closure

This chapter presented the findings of the hydraulic model experiments and numerical analysis on the stability of armor units against a steady overflow of tsunami. The main

conclusions are shown below:

1. Two important factors for armor stability were found, namely the impingement position of the overflow jet and the harbor-side water level.
2. Two failure modes of overturning and sliding were observed in the experiments. Numerical analysis revealed that the stability was predicted by the balance of the moment of a block in the case of overturning mode. In the sliding mode, it was necessary to consider the balance of forces on all the blocks on the slope.
3. Wave-dissipating blocks installed in two layers showed a toughness against tsunami, namely, scouring was hard to progress rapidly even when many blocks were displaced.
4. The harbor-side flow field was favorably reproduced by the following numerical computation method:
   (1) The overflow nappe above the water surface and the flow field on the harbor-side were solved separately to avoid excessive entrainment of air.
   (2) The calculation of the overflow nappe above the water surface was carried out by either a simple method based on empirical formula or a numerical method using a VOF model.
   (3) The RSM was used as a turbulence model for the computation of the harbor-side flow field. The turbulence inside the rubble mound was set to zero to avoid excessive generation of turbulence at the surface of the mound.

References

Arikawa, T., Sato, M., Shimosako, K., Tomita, T., Yeom, G., Niwa, T. (2013) : Failure mechanism and resiliency of breakwaters under tsunami, *Technical Note of Port and Airport Research Institute*, No. 1269, 37p (*in Japanese*).

Bricker, J.D., Takagi, H., Mitsui, J. (2013) : Turbulence model effects on VOF analysis of breakwater overtopping during the 2011 Great East Japan Tsunami, *Proceedings of the 2013 IAHR World Congress*, Chengdu, Sichuan, China, paper A10153.

Engelund, F. (1953) : On the laminar and turbulent flows of ground water through homogeneous sand, *Transactions of the Danish Academy of Technical Sciences*, Vol. 3, No. 4.

Higashiyama, K., Hasegawa, I., Inagaki, S. (2013) : Study of harbor side mound scouring by tsunami overflow, *Journal of JSCE, Ser. B3* (*Ocean Engineering*), **69**

(2), I_377-I_382 (*in Japanese*).

Hom-ma, M. (1940a) : Discharge coefficient on overflow weir (part-1), *JSCE Magazine, Civil Engineering*, **26** (6), 635-645 (*in Japanese*).

Hom-ma, M. (1940b) : Discharge coefficient on overflow weir (part-2), *JSCE Magazine, Civil Engineering*, **26** (9), 849-862 (*in Japanese*).

Launder, B.E., Reece, G.J., Rodi, W. (1975) : Progress in the development of Reynolds stress turbulence closure, *Journal of Fluid Mechanics*, **68**, 537-566.

OpenFOAM, http://www.openfoam.com/

Tomita, T., Kakinuma, T. (2005) : Storm surge and tsunami simulator in oceans and coastal areas (STOC), *Report of Port and Airport Research Institute*, **44** (2), 83-98.

Van der Meer, J.W. (1988) : Stability of cubes, tetrapods and accropode, *Proceedings of the Conference Breakwaters '88*, Eastbourne, U.K., 71-80.

Chapter 5

Development of Design Method for Armor Units against Tsunami Overflow

5.1 Introduction

Establishment of an accurate prediction method for armor stability against tsunami overflow is an urgent issue. The Isbash formula (Coastal Engineering Research Center [CERC], 1977) is mentioned in the Guidelines for Tsunami-Resistant Design of Breakwaters (Ministry of Land, Infrastructure, Transport and Tourism of Japan, 2013) as the method to estimate the required mass of armor units against tsunami. This formula is expressed as follows:

$$M = \frac{\pi \rho_r U^6}{48 g^3 y^6 \left(S_r - 1\right)^3 \left(\cos\theta - \sin\theta\right)^3}, \tag{5.1}$$

where, M is the mass of the armor unit, ρ_r is the density of the armor unit, U is the flow velocity near the armor unit, g is the gravitational acceleration, y is the Isbash constant, S_r is the specific gravity of the armor unit with respect to water, and θ is the angle of slope. The Isbash constant indicates the stability of the armor unit, y = 0.86 for the exposed stones and y = 1.20 for the embedded stones are shown by CERC (1977).

The required mass calculated by this formula is proportional to the sixth power of the flow velocity. This causes a practical problem that the required mass is too sensitive to variations in the estimated flow velocity. Also, the Isbash constant is required to be set properly because the required mass varies in inverse proportion to the sixth power of the Isbash constant. For concrete blocks, y = 1.08 has been applied previously regardless of the kind of block shape. This value was based on experiments using tetrapods conducted by Iwasaki et al. (1984), and it is not appropriate for use of the same value to all blocks since the Isbash constant depends on the block shape. For

example, Sakunaka and Arikawa (2013) obtained the Isbash constants of the two kinds of flat-type armor blocks (shown in Table 5.4) from the results of hydraulic model experiments. They showed that y = 1.04 to 1.18 for armor block A and y = 1.27 to 1.33 for armor block B. In addition, the applicability of the Isbash formula to the tsunami overflow in which a fast flow acts locally on armor units has not been sufficiently validated.

In this chapter, the applicability of the Isbash formula against tsunami overflow is examined. A more practical design method for armor units based on overflow depth is then developed.

5.2 Applicability of the Isbash Formula on Evaluating the Armor Stability against Tsunami Overflow

5.2.1 Applicability to the Armor Stones

Firstly, hydraulic model experiments are conducted to grasp the damage of armor stones. Then the flow field is computed and the Isbash constant is obtained from Eq. (5.1) by using the velocity near the armor stones. The applicability of the Isbash formula is examined from the relationship between the Isbash constant and the damage to armor stones.

Experiments on stability of armor stones were conducted targeting a steady overflow of tsunami. The equipment was the same as that shown in Chapter 4. The overflow was generated using a submersible pump. The model scale was 1/50. Two cross-sections, presence or absence of the widened protection mound, were experimented as shown in Fig. 5.1. Armor stones of mass 8 g (1 t in the prototype scale) were used. The height of the overflow depth was set to 2 cm and 4 cm (1 m and 2 m in the prototype scale, respectively). The duration time of the steady overflow of tsunami was set to 127 s (15 minutes in the prototype scale). The test cases are summarized in Table 5.1.

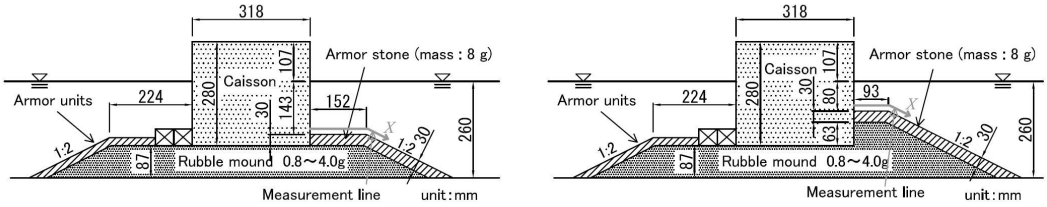

Figure 5.1 : Cross-section of the tested breakwater. (Left) : Without widened protection. (Right) : With widened protection.

Table 5.1 : Test cases on the stability of armor stones. Values in brackets represent the converted values to the prototype scale.

Case	Widened protection mound	Overflow depth h_1
Case 1	Absence	2 cm (1 m)
Case 2	Absence	4 cm (2 m)
Case 3	Presence	2 cm (1 m)
Case 4	Presence	4 cm (2 m)

Flow fields on the harbor side were computed by the method mentioned in Chapter 4. The VOF model was used for the calculation of the overflow nappe. The rubble mound and the armor stones are modeled as porous structures. The parameters and physical properties are shown in Table 5.2. The velocity distribution on the measurement line set along the mound was obtained. The distribution of the Isbash constant was then calculated backward from the Isbash formula. In this study, the flow velocity U in the Isbash formula was defined as the absolute value of the flow velocity. Measurement height of the flow velocity was set to 1.5 cm (75 cm in the prototype scale) above the mound referring to Arikawa et al. (2013).

Table 5.2 : Parameters and physical properties for the porous model.

Parameters	Rubble stones	Armor stones
Representative diameter d (m)	0.0115	0.018
Porosity n	0.39	0.46
α_0	2100	2100
β_0	1.5	1.5
Laminar resistance coefficient α	2.4×10^{1}	4.8×10^{0}
Turbulent resistance coefficient β	1.3×10^{3}	4.6×10^{2}

Fig. 5.2 shows snapshots of the experiments during and after the tsunami overflow. Fig. 5.3 shows the computed flow fields and the distribution of the Isbash constants on the measurement line. In Case 1, only a few armor stones around the shoulder of the mound moved. The Isbash constant was largest at the shoulder and the maximum value was 0.81. In Case 2, a lot of armor stones around the shoulder and slope section moved

and the rubble stones under the armor stones partly exposed at the slope section. The Isbash constant showed a maximum value of 1.16 at the slope section. In Case 3, a lot of armor stones around the shoulder moved and the rubble stones were exposed slightly. The Isbash constant showed a maximum value of 1.20 at the shoulder. In Case 4, a lot of armor stones moved and the rubble stones were also scoured. The maximum Isbash constant was 1.39 at the slope section. The damage in the cases with widened protection mound were larger than those without it. This is considered to be because the overtopped water impinges on the mound more severely due to the heightening of the mound.

The results showed that the location where the Isbash constant was large corresponded to the damaged area of the stones. Relationship between the Isbash constant and the damage to armor stones is summarized as Table. 5.3. The degree of the stone damage can be classified by using the Isbash constant of $y = 0.86$ and $y = 1.20$ as thresholds, and this agrees with the results of the past study.

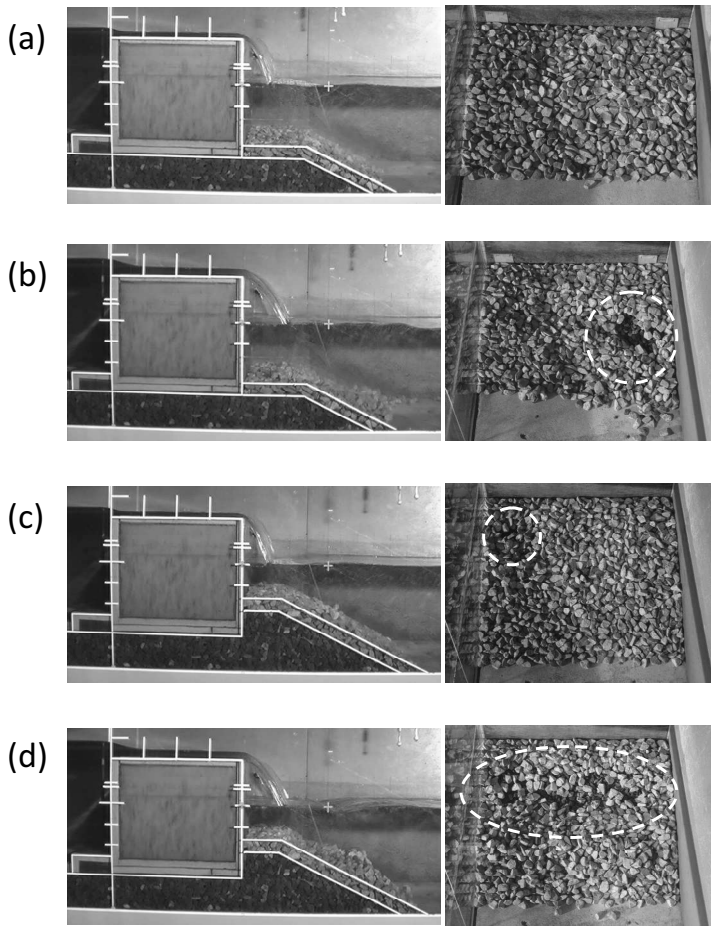

Figure 5.2 : Snapshots of the experiments during and after the tsunami overflow. (a) : Case 1. (b) : Case 2. (c) : Case 3. (d) : Case 4.

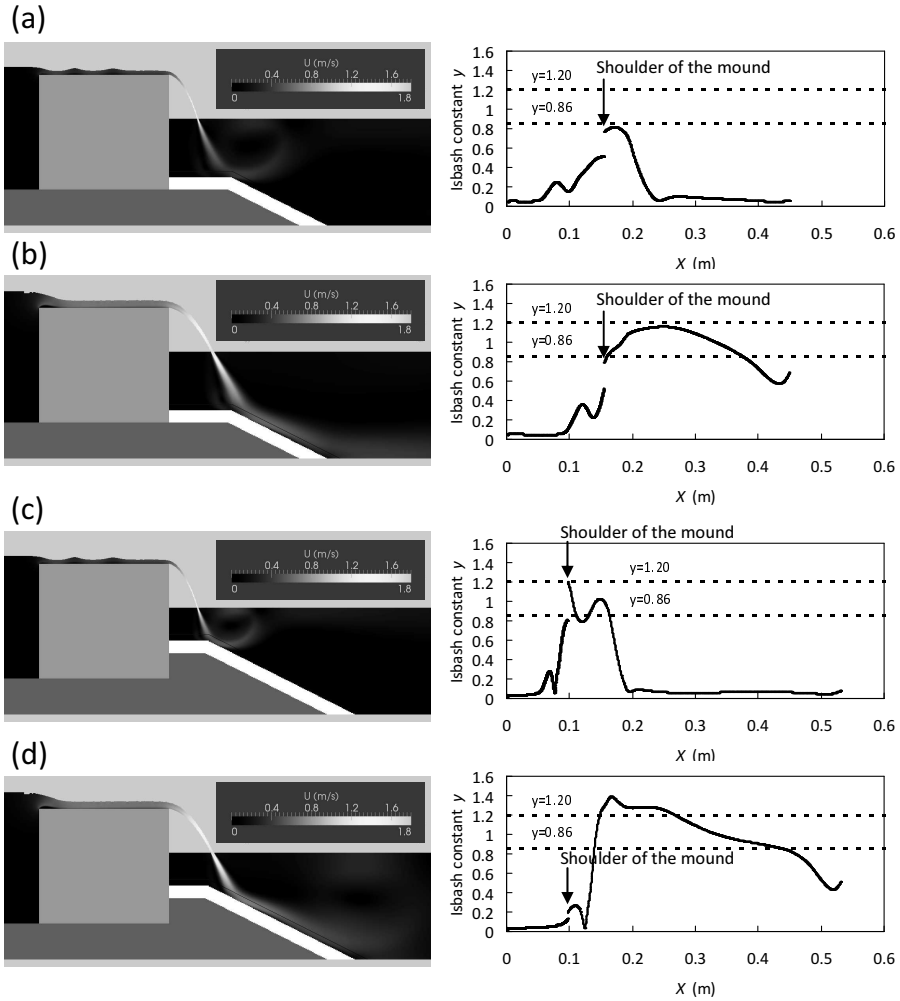

Figure 5.3 : Computed flow fields and the distribution of the Isbash constants on the measurement line. (a) : Case 1. (b) : Case 2. (c) : Case 3. (d) : Case 4.

Table 5.3 : Relationship between the Isbash constant and the damage of armor stones.

Isbash constant	Damage of armor stones
Around 0.86	Armor stones move slightly
0.86 - 1.20	Armor stones move heavily and rubble stones are exposed
More than 1.20	Armor stones move heavily and rubble stones are also scoured

5.2.2 Applicability to the Concrete Blocks

Applicability of the Isbash formula to the concrete blocks was verified by applying to the experimental results described in Chapter 4. The Isbash constant for each armor unit was calculated backward using the Isbash formula. The flow velocity used in the Isbash formula was obtained by numerical computation. Experiments were conducted by changing the shape of the harbor-side rubble mound, the harbor-side water level, and the shape and mass of the armor units as described before. The 34 cases were selected to

include a wide range of conditions as shown in Table 5.4. The impingement position in the table was determined by whether the computed flow velocity is maximum on the crown section or on the slope section.

Table 5.4 : Stability test cases, B is the crown width, h is the harbor-side water level, h_1 is the overflow depth.

Armor unit	Mass	Widened protection	B	h	h_1 at stability limit	Impinge-ment position
Wave-dissipating Block 	61 g	—	45.0 cm	26 cm	5 cm	Crown section
		—	30.0 cm	26 cm	4 cm	
	122 g	—	45.0 cm	26 cm	7 cm	
		—	30.0 cm	26 cm	6 cm	
	235 g	—	45.0 cm	26 cm	9 cm	
		—	30.0 cm	26 cm	7 cm	
	61 g	—	15.0 cm	26 cm	5 cm	Slope section
	122 g	—	15.0 cm	26 cm	6 cm	
	235 g	—	15.0 cm	26 cm	8 cm	
Flat-type armor block A 	64 g	—	46.9 cm	26 cm	5 cm	Crown section
		○	15.9 cm	26 cm	3 cm	
		○	21.1 cm	30 cm	3 cm	
	254 g	—	37.5 cm	26 cm	7 cm	
		○	16.5 cm	26 cm	4 cm	
		○	24.5 cm	30 cm	7 cm	
	17 g	—	31.6 cm	30 cm	5 cm	Slope section
	64 g	—	46.9 cm	26 cm	5 cm	
		○	10.7 cm	26 cm	6 cm	
		○	10.7 cm	30 cm	6 cm	
	254 g	—	21.5 cm	30 cm	9 cm	
		○	8.5 cm	30 cm	9 cm	
Flat-type armor block B 	16 g	—	35.8 cm	26 cm	6 cm	Crown section
		○	15.5 cm	26 cm	3 cm	
	33 g	—	43.5 cm	26 cm	7 cm	
		○	19.4 cm	26 cm	4 cm	
	64 g	○	24.3 cm	26 cm	5 cm	
	123 g	—	50.5 cm	26 cm	8 cm	
		○	30.5 cm	26 cm	7 cm	
		○	30.5 cm	30 cm	9 cm	
	33 g	—	14.9 cm	26 cm	5 cm	Slope section
		—	24.4 cm	30 cm	6 cm	
		○	9.9 cm	26 cm	7 cm	
	64 g	○	12.4 cm	30 cm	8 cm	
	123 g	○	9.0 cm	26 cm	7 cm	

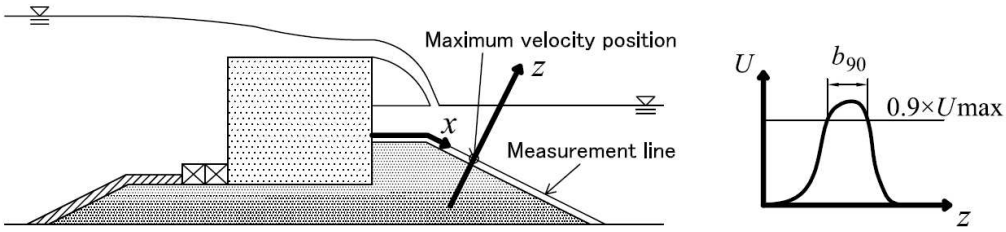

Figure 5.4 : Definition of width of water jet.

In the case of concrete blocks, since the fast flow is supposed to act only on the part of the block, the influence of the width of the water jet on the Isbash constant was examined. The definition of the width of the water jet b_{90} is shown in Fig. 5.4. The distribution of the flow velocity in the normal direction of the mound is obtained at the location of the maximum velocity on the measurement line. The width of the water jet b_{90} was defined as the range of the more than 90% of the maximum flow velocity in the normal direction of the mound. The width of the water jet b_{90} divided by the block length D is written as the relative width of water jet hereafter.

Fig. 5.5 shows the relationship between the relative width of the water jet and the Isbash constant y obtained by backward calculation using Isbash formula (CERC, 1977). The Isbash constants tend to be larger as the relative width of the water jet decreases. In particular, this tendency is remarkable in the case of the wave-dissipating blocks. Also, the trend with the Isbash constants varies depending on the impingement position of the water jet. The Isbash constants when the jet impinges on the slope section are larger as a whole. This suggests that the Isbash formula tends to overestimate the effect of the slope angle in the cases of concrete blocks. The reason for this will be discussed later.

In addition, the Isbash constants of the flat-type armor blocks vary widely when the jet impinges on the slope section. The Isbash formula is based on the balance of moment acting on a single stone, whereas the flat-type armor blocks sometimes moves as a group in a sliding failure mode when the jet impinges on the slope section. This implies that the calculation result with the Isbash formula varies widely when it is applied to the sliding failure mode.

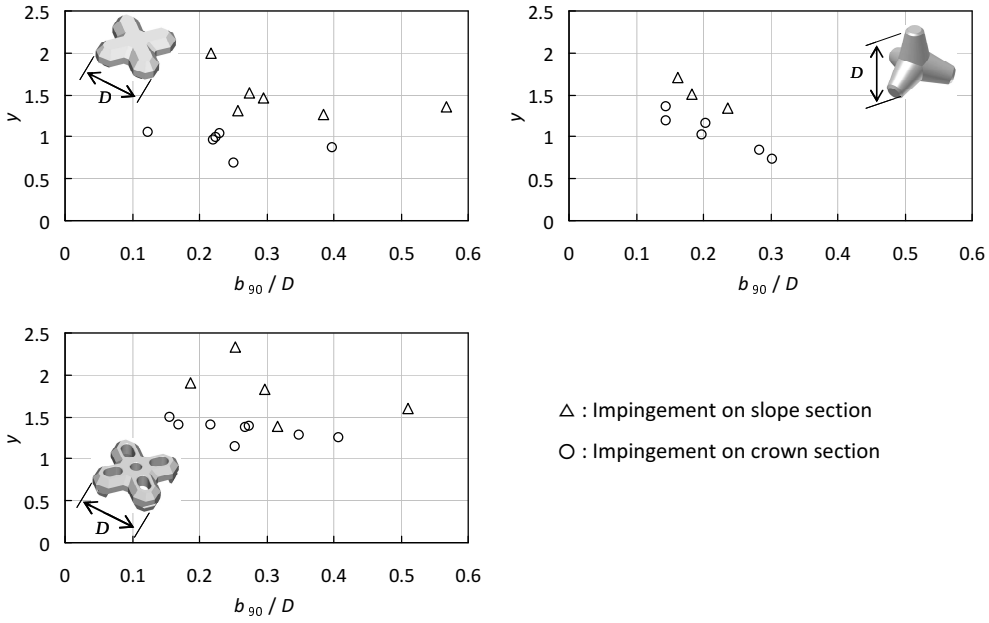

Figure 5.5 : Isbash constant *y* calculated backward using formula by CERC (1977).

5.2.3 Discussion on the Formulation of the Isbash Formula

The effect of the slope angle is discussed based on the formulation of the Isbash formula. Isbash (1932) derived the following equation of the balance of moment acting on a stone located on a slope as shown in Fig. 5.6.

$$\frac{1}{2}k\rho_w U^2 a^2 \cdot \xi a + (\rho_r - \rho_w) a^3 g \sin\theta \cdot \left(\frac{a}{2} - \zeta a\right) = (\rho_r - \rho_w) a^3 g \cos\theta \cdot \frac{a}{2}, \quad (5.2)$$

where, k is the shape factor, ρ_r is the density of the stone, ρ_w is the density of water, U is the flow velocity, a is the stone diameter, θ is the angle of the slope, ζa is the height of the rotation axis from the slope, and ξa is the height of the acting position of the fluid force measured from the rotation axis. Eq. (5.2) is simplified as follows:

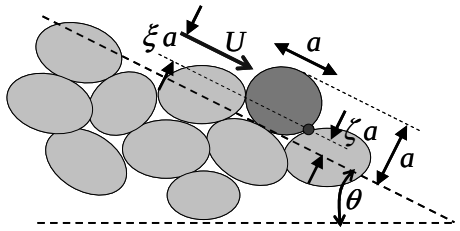

Figure 5.6 : Model of balance of the moment by Isbash (1932).

$$U = \sqrt{\frac{1}{2\xi k}}\sqrt{2g\left(S_r - 1\right)}\sqrt{a}\sqrt{\cos\theta - \left(1 - 2\zeta\right)\sin\theta}\,. \tag{5.3}$$

If $\zeta < 0.5$, the moment due to the tangential component of its own weight acts in a direction to rotate the stone. Whereas, it acts to stabilize the stone if $\zeta > 0.5$. By assuming that $\zeta = 0.5$ on average, Eq. (5.3) becomes as follows:

$$U = Y\sqrt{2g\left(S_r - 1\right)}\sqrt{a}\sqrt{\cos\theta}, \quad Y = \sqrt{\frac{1}{2\xi k}}\,, \tag{5.4}$$

where, Y is the Isbash constant for the embedded stone. It was determined that $Y = 1.20$ from the results of experiments. Assuming that the stone is a sphere of diameter a, Eq. (5.4) is rewritten as:

$$M = \frac{\pi\rho_r U^6}{48g^3 Y^6\left(S_r - 1\right)^3\left(\cos\theta\right)^3}\,. \tag{5.5}$$

In Eq. (5.5), the Isbash constant is denoted as Y to distinguish it from the Isbash constant y in Eq. (5.1). Thus, Eq. (5.5) derived by Isbash (1932) and Eq. (5.1) by CERC (1977) have different expressions for the effect of the slope angle. The Isbash formula by CERC (1977) corresponds to that the $\zeta = 0$ in Eq. (5.3). In other words, the difference between the two formulae is in how the height of the axis of rotation is assumed.

The ratios of the required mass of the armor units on a slope to that on a horizontal plane which are calculated by using two formulae are shown in Fig. 5.7. The effect of the slope angle in the formula by CERC (1977) is larger than that by Isbash (1932). For example, when the slope angle is 1:2, the ratio is calculated as about 1.4 according to the formula by Isbash (1932), whereas it becomes about 11 according to the formula by CERC (1977).

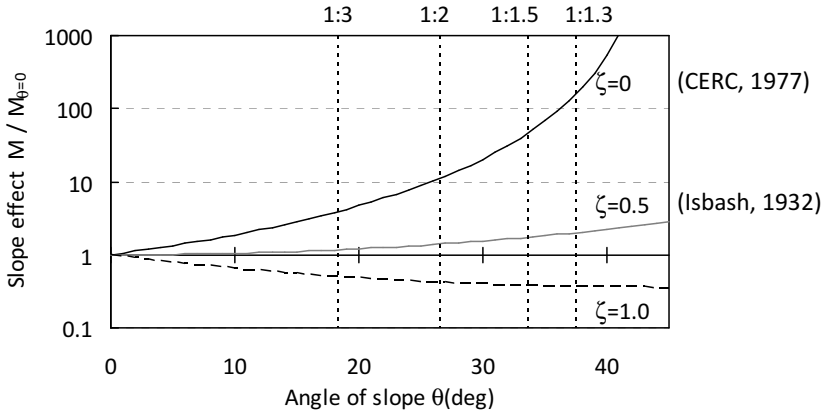

Figure 5.7 : Effect of the slope angle on the calculation of the required mass of armor units.

Fig. 5.8 shows the Isbash constant Y of each armor unit obtained by backward calculation using Eq. (5.5). Since the Isbash constant Y is regardless of the slope angle, the effect of the slope angle is properly taken into account in Eq. (5.5). The reason is considered that $\zeta = 0.5$ is closer to the actual situation than $\zeta = 0$ in the case of the concrete blocks. The range of variation in the Isbash constant Y of the wave-dissipating blocks is about ±10%, and that of the flat-type armor blocks is about ±20%.

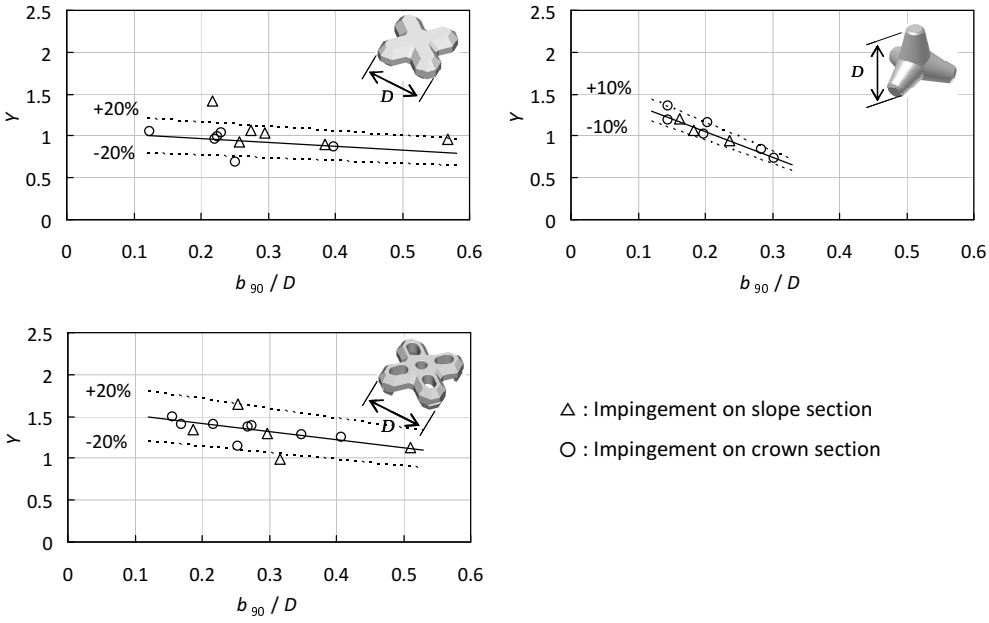

Figure 5.8 : Isbash constant Y calculated backward using formula by Isbash (1932).

When calculating the required mass of the armor units using the Isbash formula in the design work, the use of Eq. (5.5) by Isbash (1932) and the Isbash constant Y shown

in Fig.5.8 will enable the calculation more accurately than the conventional method.

5.2.4 Example of the Design Calculation

An example of the design calculation of the required mass of the armor units by the above method is shown below. The assumed cross-section of the breakwater and the water level of tsunami are shown in Fig. 5.9. The caisson is 15.0 m in height and 15.0 m in width. The rubble mound is 3.0 m in thickness, and the widened protection mound with thickness of 5.0 m and crown width of 5.0 m is placed there on. The water depth on the sea-side and harbor-side are 21.5 m and 15.0 m, respectively. The overflow depth becomes 3.5 m. Flat-type armor block B is used to cover the harbor-side mound. The specification of the block is shown in Table 5.5. There are 4 masses of the block, 2 t, 4 t, 8 t, and 16 t. Stability is examined for each mass.

The crown width of the widened protection mound is treated as a fixed value in this example, though it should be normally varied corresponding to the size of the armor blocks. In addition, the computation of the flow field is conducted in the absence of the armor blocks for simplicity.

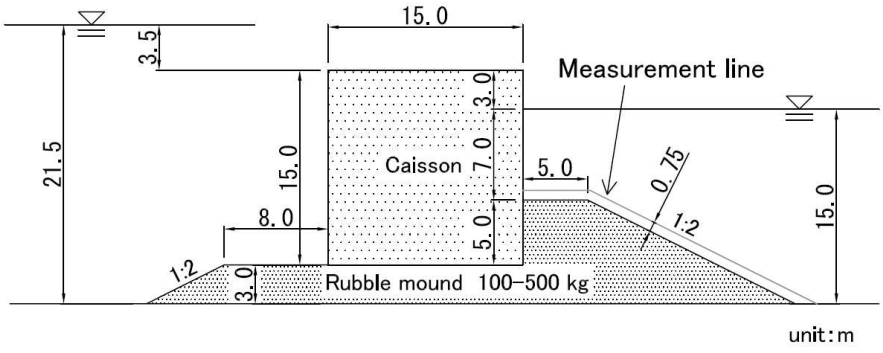

Figure 5.9 : Cross-section of the breakwater.

Table 5.5 : Specification of the blocks (Flat-type armor block B)

Type	Mass M (t)	Volume V (m^3)	Block length D (m)	Block height H (m)
2 t	2.045	0.889	1.86	0.670
4 t	4.073	1.771	2.34	0.842
8 t	8.078	3.512	2.94	1.058
16 t	16.102	7.001	3.70	1.332

Firstly, distribution of the flow velocity along the rubble mound is obtained by conducting a numerical computation of the flow field. Fig. 5.10 shows the harbor-side flow field and the distribution of the flow velocity along the mound. The maximum

flow velocity is 5.70 m/s on the slope section. The width of the water jet b_{90} is then obtained from the flow velocity distribution in the normal direction of the slope at the location of maximum flow velocity. It is obtained as b_{90} = 1.44 m as shown in Fig. 5.11. Thus the relative width of the water jet for each block size becomes b_{90}/D = 0.77, 0.62, 0.49, and 0.39, respectively. The Isbash constant is obtained by using Fig. 5.8 as Y = 0.86, 1.02, 1.14, and 1.24, respectively. The constants for 2 t and 4 t blocks were obtained by linear extrapolation. The required mass is calculated as 10.08 t, 3.72 t, 1.88 t, and 1.14 t, respectively by using Eq. (5.5). Therefore, it is judged as unstable for the 2 t block, whereas it is judged as stable for the blocks larger than 4 t. Table 5.6 summarizes the above descriptions. It is concluded that a block of 4 ton or more is required to ensure stability against this condition.

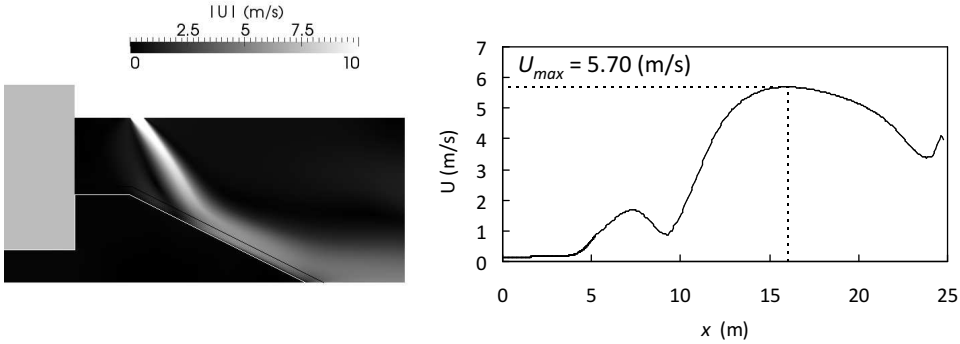

Figure 5.10 : Computed harbor-side flow field and flow velocity distribution on the measurement line.

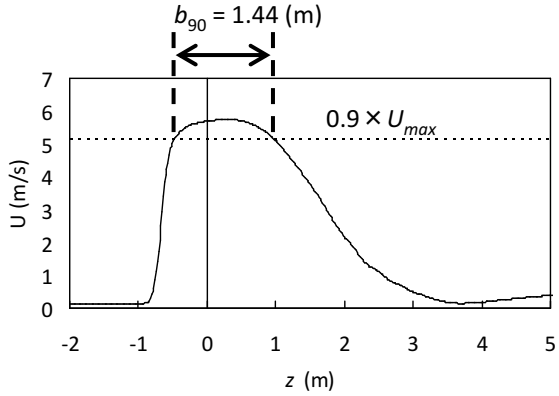

Figure 5.11 : Width of water jet b_{90}.

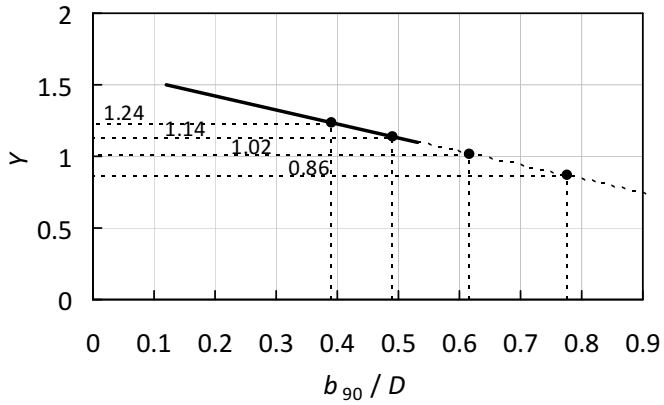

Figure 5.12 : Isbash constant *Y* for each block size.

Table 5.6 : Calculation result of the required mass.

	2 t	4 t	8 t	16 t	Remarks
Block mass M (t)	2.045	4.073	8.078	16.102	
Specific gravity S_r	2.233				
Block length D (m)	1.86	2.34	2.94	3.70	
Maximum flow velocity U (m/s)	5.70				Fig. 5.10
Water jet width b_{90} (m)	1.44				Fig. 5.11
Relative water jet width b_{90}/D	0.77	0.62	0.49	0.39	
Isbash constant Y	0.86	1.02	1.14	1.24	Fig. 5.12
Angle of slope θ (deg)	26.6				
Required mass M_{cal} (t)	10.08	3.72	1.88	1.14	Eq. (5.5)
Judgement	N.G.	O.K.	O.K.	O.K.	

5.3 Proposal of a Novel Stability Verification Method for Armor Units Based on Overflow Depth

5.3.1 Derivation of Evaluation Formula for Armor Stability

In the previous section, the applicability of the Isbash formula against tsunami overflow was examined, and some suggestions for a more accurate design were presented. However, there are still some issues to use the Isbash formula as shown below:

1. It requires a lot of labor and time to obtain the flow velocity by numerical computation.
2. The flow velocity near the armor units varies greatly depending on the numerical analysis method as pointed out by Sunakawa et al. (2014).

Thus, a new stability verification method was developed based on the findings of

experiments and numerical analysis. The basic concept is shown below. Firstly, the overflow depth is used to represent the external force acting on the armor units. This will enable the calculation more easily and robustly than the conventional method using flow velocity. Two formulae are used corresponding to the two failure modes of overturning and sliding. The overflow depth of the stability limit corresponding to each failure mode is obtained and the final stability limit is determined by the severer one. In addition, the influence of the impingement position of the water jet and the influence of the harbor-side water level are taken into account. They are the key factors for armor stability.

The developed formulae are shown below:

(Overturning mode)

$$\frac{h_1}{(S_r-1)D_n} = N_{S1} = f\left(\frac{B}{L}, \frac{d_2}{d_1}\right), \tag{5.6}$$

(Sliding mode)

$$\frac{h_1}{(S_r-1)S} = N_{S2} = f\left(\frac{d_2}{d_1}\right) \quad \text{for} \quad \frac{B}{L} \le 1.1, \tag{5.7}$$

where, h_1 is the overflow depth, S_r is the specific gravity of the armor unit with respect to water, D_n is the nominal diameter of the armor unit, S is the slope length of the harbor-side mound, N_{S1} and N_{S2} are the stability numbers, B is the crown width of the harbor-side mound, L is the impingement position of the overflow jet, d_1 is the crown height of the caisson above the harbor-side water level, and d_2 is the submerged depth above the armor units. The definition of these dimensions are shown in Fig. 5.13. The impingement position L is calculated assuming that the trajectory of the water below the water surface is a straight line:

$$L = L_0 + \frac{u_{0x}}{u_{0z}} d_2, \tag{5.8}$$

where, L_0 is the landing position of the overtopped water on the harbor-side water surface, and u_{0x}, u_{0z} are the flow velocities on the harbor-side water surface. These values are calculated by the method mentioned in Chapter 4 (see 4.3.1).

Stability numbers N_{S1} and N_{S2} are functions of B/L and d_2/d_1, which are the parameters representing the impingement position and the harbor-side water level respectively. The stability is determined only by Eq. (5.6) if B/L is larger than 1.1 since failure by sliding mode does not occur when the overflow jet impinges on the crown section. Similarly, the stability of wave-dissipating blocks is determined only by Eq.

(5.6).

For the overturning mode, the overflow depth h_1 represents the acting force on armor units, whereas the nominal diameter of armor units D_n represents the resistance force as shown in Eq. (5.6). For the sliding mode, on the other hand, the slope length S is used to represent the resistance force as shown in Eq. (5.7). This is because the resistance force should be represented by the total length of the blocks on the slope since the blocks on the slope section slide together as a whole in the sliding mode. As a result, the overflow depth of the stability limit in the sliding mode is not dependent on the block size as can be seen from Eq. (5.6), whereas, that in the overturning mode is proportional to the block size. This corresponds with the experimental results described above (see Fig. 5.14).

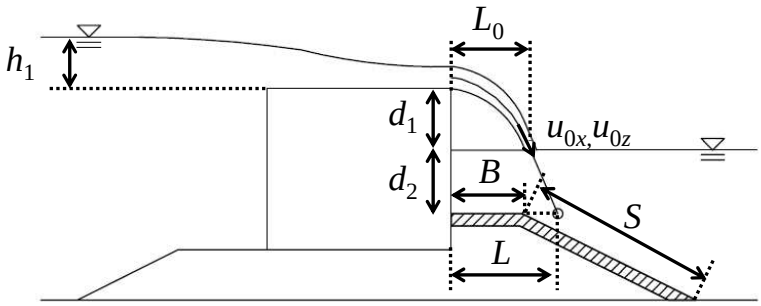

Figure 5.13 : Definition of the dimensions used in the stability verification method.

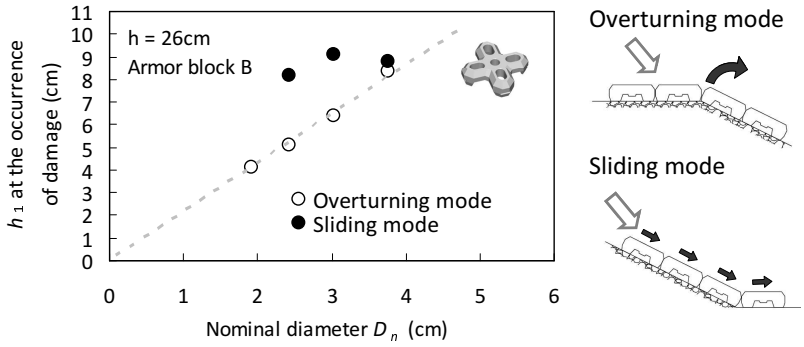

Figure 5.14 : Relationship between the nominal diameter and the overflow depth at the occurrence of damage by each failure mode. (Reshown, see 4.2.2.)

5.3.2 Determination of Stability Numbers for Armor Units

The stability numbers N_{S1} and N_{S2} for each block were determined through the experimental results. Fig. 5.15(a) shows the influence of the impingement position by plotting the stability number N_{S1} against B/L. The conditions on harbor-side water depth are almost at the same level (d_2/d_1 = 0.47 to 0.66). The damaged data with sliding mode

is excluded in the figure to reveal the stability limit of overturning mode. The stability limit is expressed in a single line as a function of B/L regardless of the mass of the block. Also, the difference in the stability due to the impingement position appears clearly. Fig. 5.15(b) shows the influence of the harbor-side water level by plotting the N_{S1} against d_2/d_1. The data on the conditions of $B/L > 1.0$ is shown. The stability tends to increase as d_2/d_1 increased.

Fig. 5.16 shows the stability numbers N_{S1} and N_{S2} for flat-type armor blocks determined through all the test results. Different lines are used according to the B/L in Fig. 5.16(a). When B/L is between 0.8 and 1.0, the value is obtained by linear interpolation. The stability number for the wave-dissipating block is shown in Fig. 5.17. In the case of the wave-dissipating block, the influence of the impingement position was different from the case of the flat-type armor blocks. Namely, the cases in which the jet impinged on the crown section showed higher stability than the cases of impingement on the slope section. This result was reflected in the stability number.

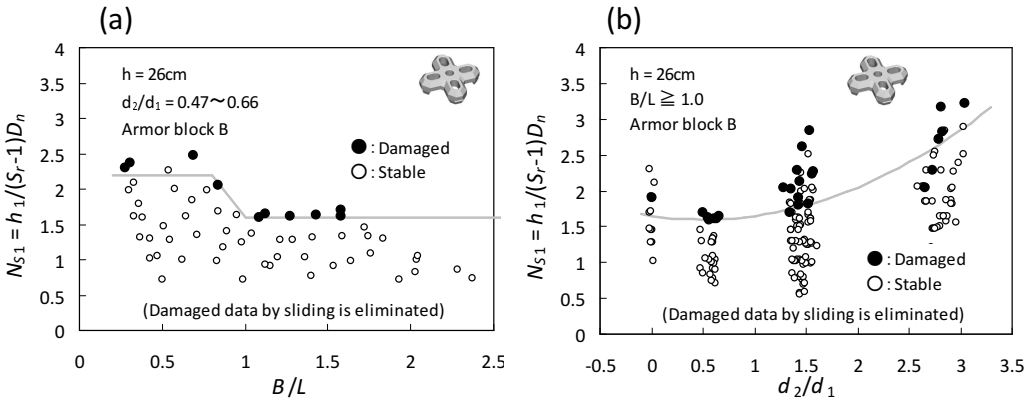

Figure 5.15 : (a) : Influence of B/L on N_{S1}. (b) : Influence of d_2/d_1 on N_{S1}.

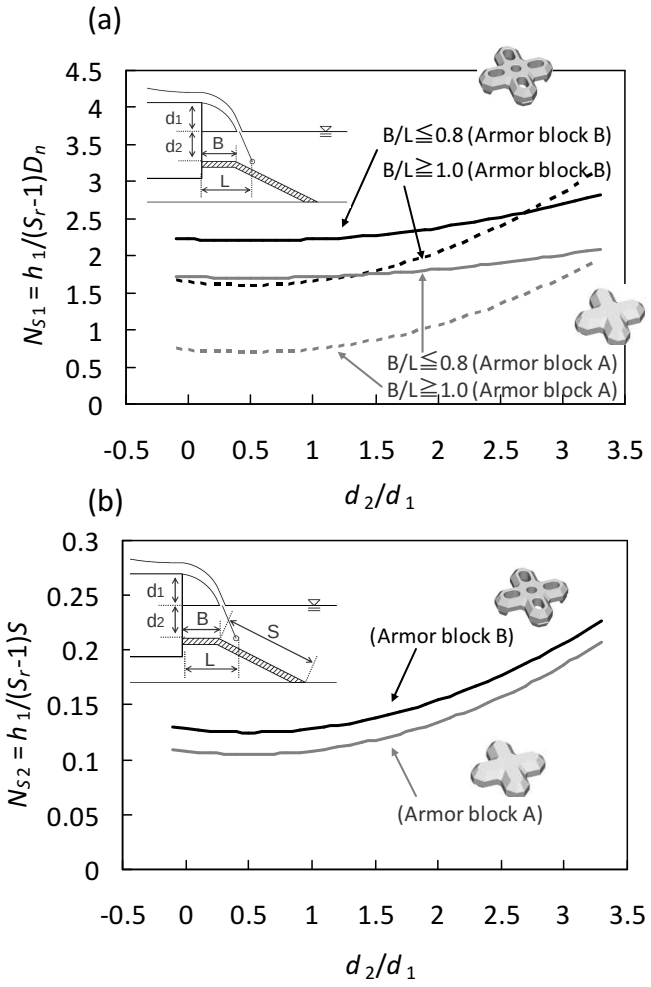

Figure 5.16 : Stability numbers for flat-type armor blocks. (a) : N_{S1} (for overturning mode). (b) : N_{S2} (for sliding mode).

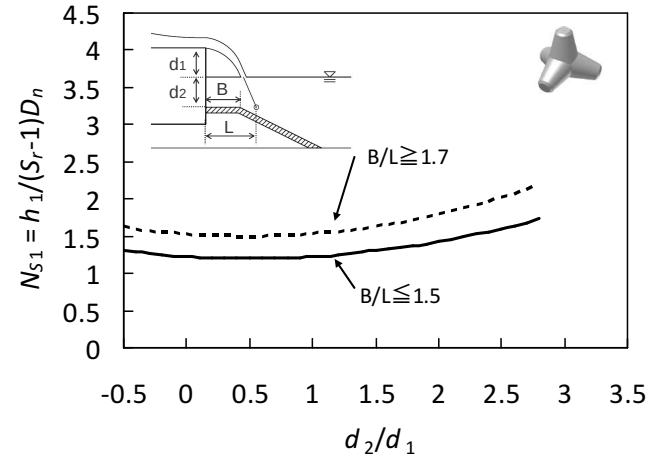

Figure 5.17 : Stability number N_{S1} for wave-dissipating block.

5.3.3 Comparison with Experimental Results

Fig. 5.18 shows a comparison of the estimated overflow depth of stability limit with the damaged overflow depth in the experiments. The estimated results are on the safe side as a whole, and they show good agreement for both failure modes.

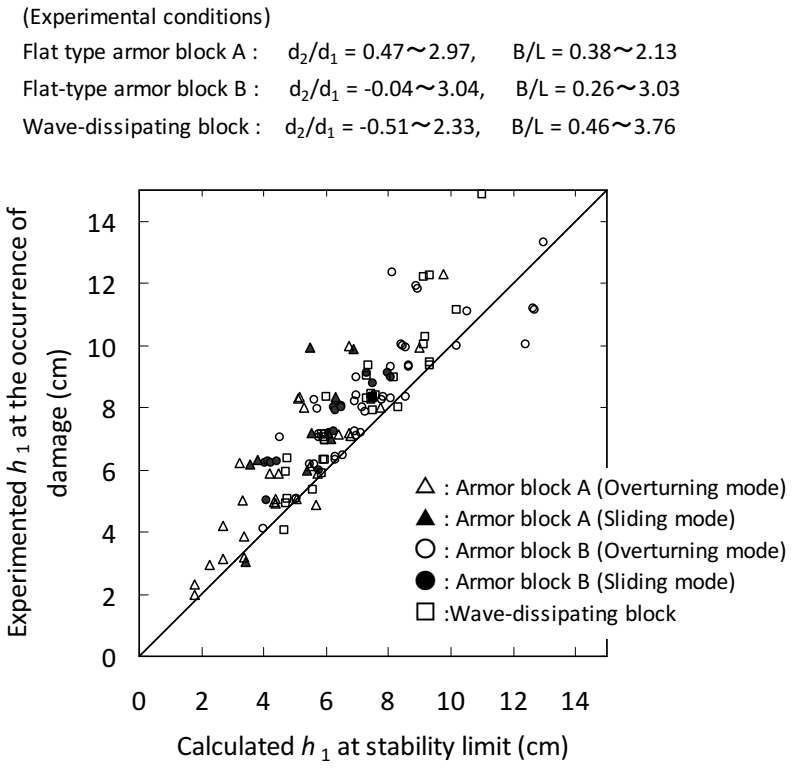

Figure 5.18 : Comparison of calculated and experimented overflow depth of the stability limit.

5.3.4 Example of the Design Calculation

An example of the design calculation of the required mass of the armor units by the above method is shown below. The assumed cross-section of the breakwater and the water level of tsunami are the same as those used in the previous section. Though the crown width was treated as a fixed value in the example of the Isbash formula for simplicity, the actual length is used in this example. The crown width is calculated as the length of two blocks.

Firstly, the dimensions h_1, d_1, d_2, B, L, and S which are used in the calculation are obtained. The dimensions except for the impingement position L are obtained immediately from the cross-section of the breakwater and the water level of tsunami. The impingement position L is calculated by using the empirical formulae as shown in Table 5.7. The parameter B/L for each block mass (2 t, 4 t, 8 t, 16 t) is obtained as 0.36,

0.46, 0.59, and 0.75. Thus they are the conditions that the overflow jet impinges on slope section. The parameter d_2/d_1 for each block mass is obtained as 2.11, 2.05, 1.98, and 1.89, respectively.

Table 5.7 : Specifications used for the design calculation.

	2 t	4 t	8 t	16 t	Remarks
Mass of block M (t)	2.045	4.073	8.078	16.102	
Volume of block V (m^3)	0.889	1.771	3.512	7.001	
Block length D (m)	1.86	2.34	2.94	3.70	
Block height H (m)	0.670	0.842	1.058	1.332	
Overflow depth h_1 (m)	3.50				
d_1 (m)	3.00				
d_2 (m)	6.33	6.16	5.94	5.67	
Crown width B (m)	3.77	4.73	5.93	7.45	
Slope length S (m)	19.39	19.77	20.26	20.86	
Overflow discharge q (m^3/s/m)	10.15				Eq. (4.1)
h_2 (m)	1.58				Eq. (4.9)
u_2 (m/s)	6.42				$u_2 = q / h_2$
L_0 (m)	5.65				Eq. (4.10)
u_{x0} (m/s)	6.42				Eq. (4.11)
u_{z0} (m/s)	8.62				Eq. (4.11)
L (m)	10.36	10.24	10.07	9.87	Eq. (5.8)

Stability against overturning is verified. The diagram of the stability number for the flat-type armor block B against overturning (Fig. 5.16(a)) is used. The d_2/d_1 and $h_1/(S_r\text{-}1)D_n$, which are obtained by the design conditions, is plotted on the diagram and the stability of the block is judged by comparing the plot point and the curve in the diagram. If the plot point is under the curve of N_{S1}, the block is judged as stable. In these conditions, the curve for $B/L \leqq 0.8$ is used for comparison. The results are shown in Table 5.8 and Fig. 5.19. It is judged as unstable for the block of 2 t, whereas stable for the blocks larger than 4 t against overturning mode.

Table 5.8 : Verification result of the stability against overturning.

	2 t	4 t	8 t	16 t	Remarks
B / L	0.36	0.46	0.59	0.75	
d_2 / d_1	2.11	2.05	1.98	1.89	
D_n (m)	0.962	1.210	1.520	1.913	$D_n = V^{1/3}$
$N_{S1} = h_1/(S_r\text{-}1)D_n$	2.95	2.35	1.87	1.48	
N_{S1} (Diagram of stability number)	2.41	2.39	2.38	2.35	
Judgement (overturning)	N.G.	O.K.	O.K.	O.K.	

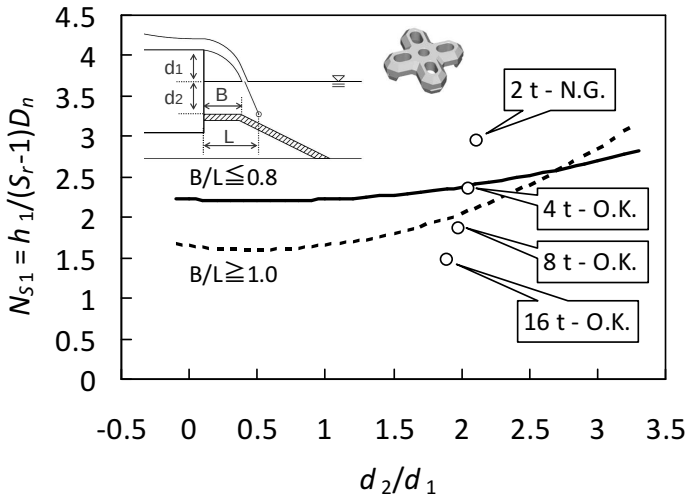

Figure 5.19 : Verification result of the stability against overturning.

Stability against sliding is then verified. The diagram of the stability number for flat-type armor block B against sliding (Fig. 5.16(b)) is used. The same procedure as that for overturning is performed. The results are shown in Table 5.9 and Fig. 5.20. It is judged as stable for all the blocks against sliding mode.

By combining the judgement against two failure modes, it is concluded that a block of 4 t or more is required to ensure stability.

Table 5.9 : Verification result of the stability against sliding.

	2 t	4 t	8 t	16 t	Remarks
B / L	0.36	0.46	0.59	0.75	
d_2 / d_1	2.11	2.05	1.98	1.89	
Slope length S (m)	19.39	19.77	20.26	20.86	
$N_{S2} = h_1/(S_r\text{-}1)S$	0.146	0.144	0.140	0.136	
N_{S2} (Diagram of stability number)	0.159	0.156	0.153	0.150	
Judgement (sliding)	O.K.	O.K.	O.K.	O.K.	
Judgement (overall)	**N.G.**	**O.K.**	**O.K.**	**O.K.**	

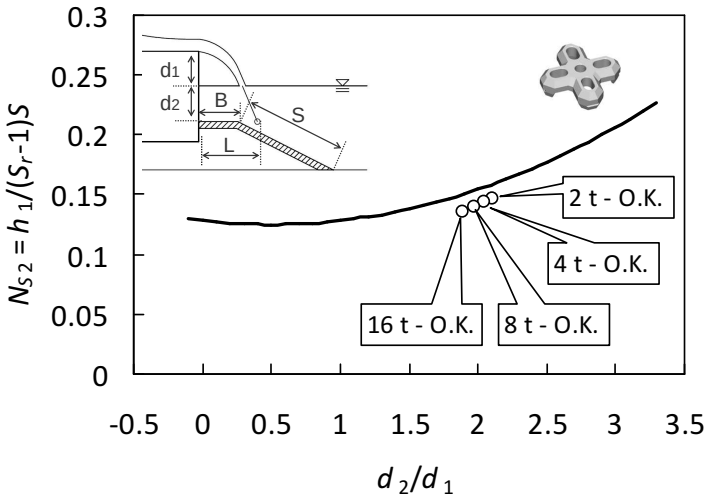

Figure 5.20 : Verification result of the stability against sliding.

5.4 Closure

This chapter examined the applicability of the Isbash formula, which is the conventional design method for the armor units based on the flow velocity, against tsunami overflow. Also a more practical design method was presented. The main conclusions are shown below:

1. The applicability of the Isbash formula by CERC (1977) against armor stones has been confirmed from the result that the relationship between the Isbash constant and the degree of damage to armor stones almost agreed with that in the past study.
2. In the case of concrete blocks, the Isbash constant depends on the width of the water jet.
3. The formula by CERC (1977) tends to overestimate the slope effect in the case of concrete blocks. The formula by Isbash (1932) takes the slope effect into account more properly.
4. A new practical design method of the armor units against tsunami overflow has been proposed. The features of the method are the following: (1) Overflow depth is used to represent the external force and this enables the calculation more easily and robustly than the conventional method using flow velocity. (2) Two formulae are used corresponding to the two failure modes of overturning and sliding. (3) The influence of the impingement position of the water jet and the influence of the

harbor-side water level are taken into account.

5. The validity of the new method was confirmed by comparing with the experimental results.
6. Examples of design calculation of the armor units were shown for two method. One is the Isbash formula by Isbash (1932) with the use of the Isbash constant considering the width of the water jet. The other is the newly proposed method using overflow depth.

References

Arikawa, T., Sato, M., Shimosako, K., Tomita, T., Yeom, G., Niwa, T. (2013) : Failure mechanism and resiliency of breakwaters under tsunami, *Technical Note of Port and Airport Research Institute*, No. 1269, 37p (*in Japanese*).

Coastal Engineering Research Center (1977) : Shore Protection Manual, U.S.Army Corps of Engrs., U.S.Govt. Printing Office, Vol. II, 7_213-7_216.

Hudson, R.Y. (1959) : Laboratory investigation of rubble-mound breakwaters, *Proceedings of the American Society of Civil Engineers*, ASCE, Vol. 85, WW3, 93-121.

Isbash, S.V. (1932) : Construction of dams by dumping stones into flowing water, Sci. Res. Inst. Hydrotech. Leningrad, Translated by A. Dovjikov, U.S.Army Corps of Engineers, 1935.

Iwasaki, T., Mano, A., Nakamura, T., Horikoshi, N. (1984) : Experimental study on hydraulic force acting on mound and pre-packed caisson of submerged breakwater under steady flows, *Proceedings of the 31st Japanese Conference on Coastal Enginiiring*, 527-531 (*in Japanese*).

Ministry of Land, Infrastructure, Transport and Tourism of Japan, Ports and Harbours Bureau (2013) : Guidelines for Tsunami-Resistant Design of Breakwaters, Sept. 2013, http://www.mlit.go.jp/common/001012142.pdf (*in Japanese*), (accessed 2014-12-18).

Sakunaka, J., Arikawa, T. (2013) : Research on stability of opening section at baymouth breakwater, *Technical Note of Port and Airport Research Institute*, No. 1274, 26p (*in Japanese*).

Sunakawa, T., Okubo, Y., Tsujio, D., Suzuki, N., Ogasawara, T. (2014) : Applicability of numerical simulations for ductility design of breakwaters against mega tsunami,

Journal of JSCE, Ser. B2 (*Coastal Engineering*), **70** (2), I_191-I_195 (*in Japanese*).

Chapter 6

Development of Economical Construction Method for Artificial Reefs in Deep Sea Area

6.1 Introduction

Production in fisheries has been declining in Japan. In particular, production in offshore fishing which accounts for 40% of the total fishing production has declined by nearly 40% in the 10-year period from 1994, and the development of fisheries in offshore areas has become an urgent matter (Nakamura et al., 2008). Snow crabs support a valuable commercial fishery as a luxury food in Japan. Though the snow crab catch in the western part of the Sea of Japan had reached 15,000 tons before 1970, it decreased sharply to 2,000 tons in the early 1990s. In recent years, it is steadily recovering thanks to imposed catch limits (Fisheries Agency of Japan, Resources Enhancement Promotion Department, 2013). For the purpose of a reliable recovery to a higher level, the Fisheries Agency of Japan has been constructing artificial nursery reefs for snow crabs since 2007 (Fisheries Agency of Japan, Construction Division, 2007 ; Nakamura et al., 2008).

The roles of the nursery reefs for snow crabs are to ensure their feeding grounds, hiding places, and spawning grounds. The nursery reefs are configured by installing concrete blocks on the sea bottom at regular intervals as shown in Fig. 6.1. The planned reefs are within a 2 km square on the basis of the group size of the snow crabs (Fisheries Agency of Japan, Fisheries Infrastructure Department, 2008). The installed interval of blocks is about 250 m to prevent entry of trawlers. The installation depth is about 250 m, corresponding to the depth of the female snow crab habitat. The blocks used for the nursery reefs should satisfy the following conditions (Fisheries Agency of Japan, Fisheries Infrastructure Department, 2008) : (1) The height of the block should be more than 3 m so that a fishfinder can recognize it. (2) The block should have a

enough weight so as not to be moved by a trawl net. (3) The block should be of a structure so that settlement and embedding does not occur. (4) The block should be stable against ocean currents. Snow crabs were observed to reside in blocks in a remotely operated vehicle (ROV) survey conducted by Ito et al. (2008). Such blocks should have a wall structure around the bottom support. The accuracy for placement position is required to be within 30 m in radius around the planned position.

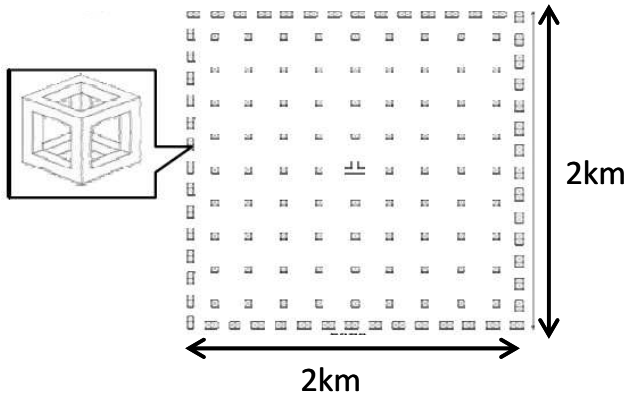

Figure 6.1 : A schematic diagram of the nursery reef for snow crabs (from Fisheries Agency of Japan, 2007).

Fish reef blocks in shallow areas are usually dropped from a ship to land on the sea bottom in a range from about 30-100 m deep. The accuracy of placement often becomes a problem (Matsumi and Seyama, 1988). Because it is difficult to ensure placement accuracy in a 30 m radius in deep water of about 250 m by a free-fall method, placing each block suspended by wire ropes has been adopted in past construction (Inada et al., 2009). However, this method is time-consuming and uneconomical at depths of more than 250 m. To ensure that the free-fall method would be possible, the block must be of a shape that falls with stable behavior in water. Also, the placement position of the block in the presence of an ambient current must be predictable so as to determine the release point.

In this chapter, a new fish reef block ensuring accurate placement by free fall is developed to enable a more economical construction of nursery reefs for snow crabs. Firstly, numerical analysis method of the fish reef blocks with complicated 3-dimensional shapes falling through water is investigated by applying the numerical method mentioned in Chapter 2. A fish reef block for snow crabs which falls with stable behavior is then developed by laboratory experiments and numerical analysis. The mechanism that stabilizes the falling behavior is discussed based on the numerical

results. The distribution of the placement position is investigated by stochastic model. Finally, a quick estimation method for the placement position is developed to determine the release point of the block in the presence of an ambient current during actual installation.

6.2 Numerical Analysis on Behavior of Fish Reef Blocks with Complicated 3-Dimensional Shapes Falling through Water

6.2.1 Numerical Analysis Method of Falling Behavior

The falling behavior of the blocks was analyzed by computing the fluid field coupled with the movement of a rigid body. The OpenFOAM CFD model was used. The governing equations for the fluid domain consist of the 3-D incompressible Navier-Stokes equation and the continuity equation. For the rigid body, the equations of motion for the translation and rotation are solved. A finite-volume method and an unstructured grid subdivided around the rigid body are used. The dynamic mesh functionality (Jasak and Tukovic, 2007) equipped in the OpenFOAM are used. At every time step, fluid domain and the motion of the rigid body are calculated alternately. Computational grid of the fluid domain is deformed along with the movement of the rigid body.

6.2.2 Validation of Numerical Analysis Method

The validity of this numerical analysis method was examined. First, experiment and numerical analysis of the falling behavior of a 2-D cylinder in water tank by Ushijima et al. (2003) were reproduced. The experimental setup is shown in Fig. 6.2. Dimensions and physical properties are shown in Table 6.1.

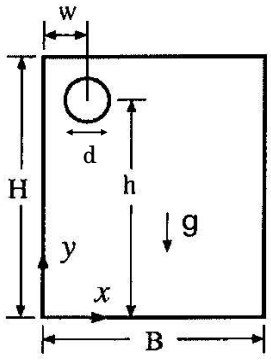

Figure 6.2 : Experimental setup for the falling behavior of a 2-D cylinder (From Ushijima et al., 2003).

Table 6.1 : Dimensions and physical properties for the computation of the falling behavior of a 2-D cylinder.

Parameters	Values
Tank width : B	100 mm
Tank height : H	150 mm
Horizontal position of cylinder : w	15 mm
Vertical position of cylinder : h	100 mm
Diameter of cylinder : d	20 mm
Density of cylinder : ρ	1200 kg/m^3
Density of water : ρ_w	1000 kg/m^3
Kinematic viscosity of water : ν	1.0×10^{-6} m^2/s

The computation was performed with three different grid sizes to examine the influence of the grid size. Each computational grid is shown in Fig. 6.3. Grid 2 and Grid 3 are obtained by subdividing the Grid 1 into 1/2 and 1/4, respectively. The number of the cells of each grid is 3520, 14080, and 56320, respectively.

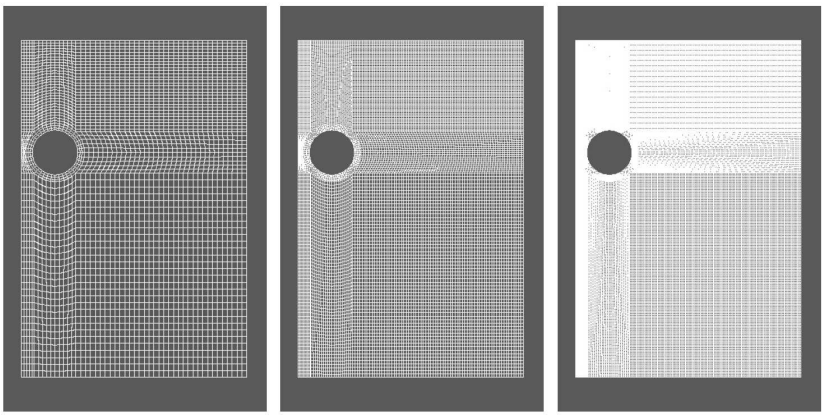

(a) Grid 1 (b) Grid 2 (c) Grid 3

Figure 6.3 : Computational grids for the analysis of the falling behavior of a 2-D cylinder.

A comparison of the computed falling tracks with the experimental and numerical results by Ushijima et al. (2003) is shown in Fig. 6.4. The numerical results reproduce the overall trend which the cylinder moves away from the side wall in the middle of the fall. The final horizontal position x/d is about 1.25 in the case of the coarsest grid (Grid 1), which is smaller than the results by Ushijima et al. (2003). The result using the finest grid (Grid 3) is about 1.9, which is a reasonable value when compared with the results in the literature.

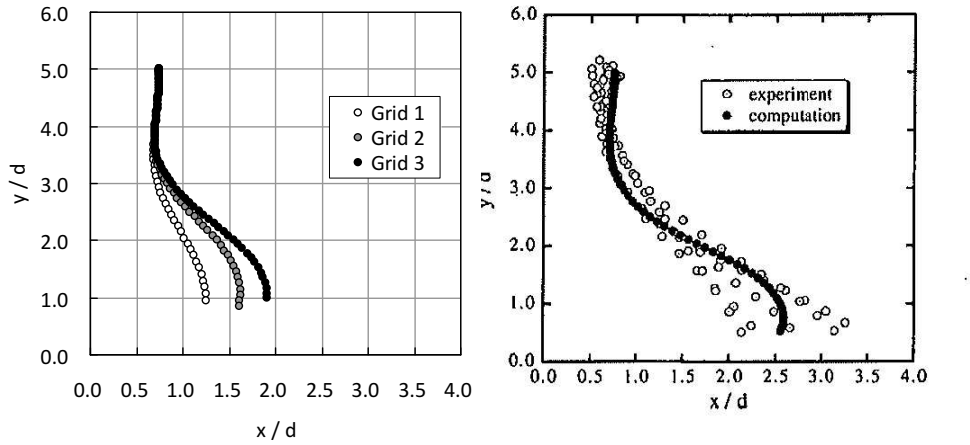

Figure 6.4 : Comparison of the falling track of cylinder. (Left) : Computed results in this study. (Right) : Results by Ushijima et al. (2003).

As another validation case, computation of the falling behavior of a coin-shaped thin cylinder was conducted to confirm whether the swing motion during free-fall could be reproduced. A schematic diagram of the computational domain and the dimensions and physical properties are shown in Fig. 6.5 and Table 6.2, respectively. The computational grid is subdivided around the cylinder as shown in Fig. 6.6. The number of grid cells is 52,788. An angular velocity of ω_y = 10 deg/s is given to the cylinder as the initial condition to give the small disturbance.

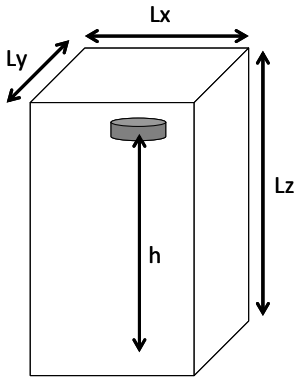

Figure 6.5 : Schematic diagram of the numerical analysis of the falling behavior of a coin-shaped cylinder.

Table 6.2 : Dimensions and physical properties for the computation of the falling behavior of a coin-shaped cylinder.

Parameters	Values
Width of tank : $L_x = L_y$	100 mm
Height of tank : L_z	250 mm
Vertical position of cylinder : h	200 mm
Diameter of cylinder : d	10 mm
Thickness of cylinder : t	1 mm
Density of cylinder : ρ	2300 kg/m^3
Density of water : ρ_w	1000 kg/m^3
Kinematic viscosity of water : ν	1.0×10^{-6} m^2/s

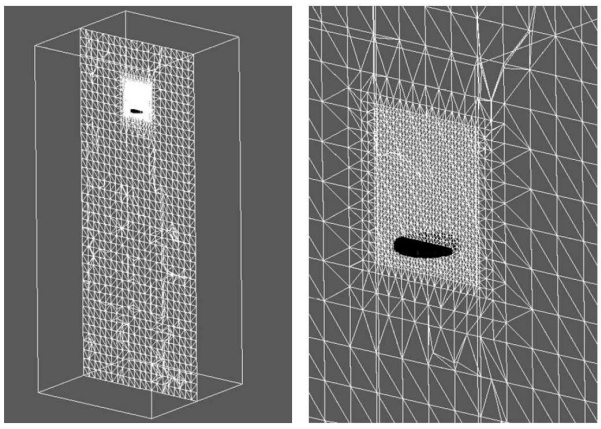

Figure 6.6 : Computational grid for the analysis of a coin-shaped cylinder.

Computed falling track is shown in Fig. 6.7. Time interval of display is 0.02 s. As the result shows the swing motion during free-fall, this computational method confirmed that it could reproduce such phenomenon.

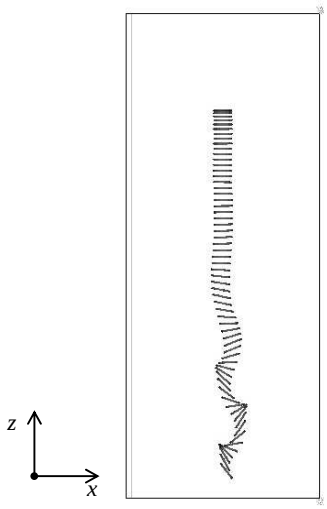

Figure 6.7 : Computed falling track of a coin-shaped cylinder.

The numerical analysis of the falling behavior of a fish reef block was conducted. The validity of the computational method was examined by comparing the falling tracks and velocities with experimental results. The analysis was performed using a developed block shape (Fig. 6.12(b)) as described below. The computation was performed with three different grid sizes since the grid size is expected to affect the computational result. The computational grid is subdivided around the block as shown in Fig. 6.8. The number of the cells in each grid is about 129,000 for Grid 1, about 162,000 for Grid 2, and 453,000 for Grid 3, respectively.

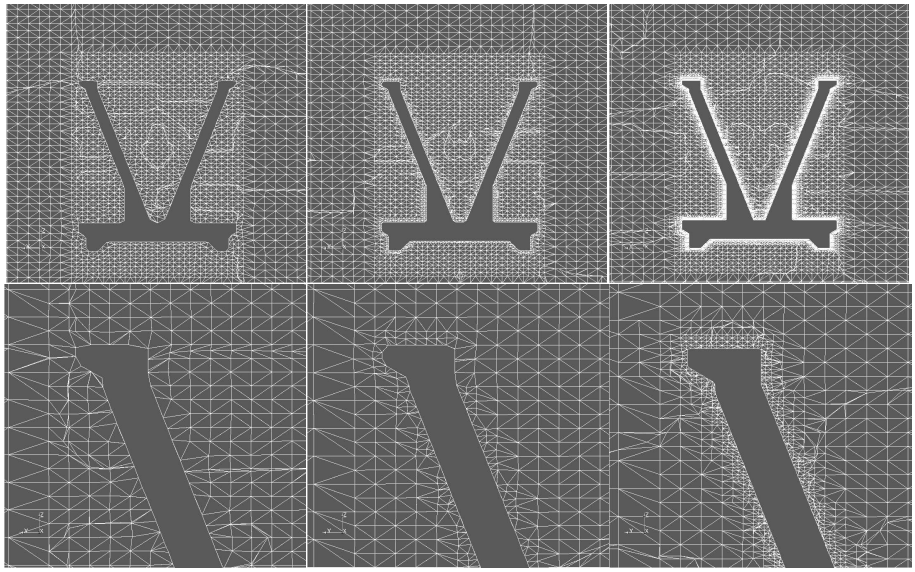

(a) Grid 1 (b) Grid 2 (c) Grid 3

Figure 6.8 : Computational grids for the analysis of the falling behavior of a fish reef block.

For comparison with the experimental results, the computation was conducted with a scale of 1/60 as well as the model experiments described below. Dimensions and physical properties are shown in Table 6.3. An angular velocity of ω_y = 1 rad/s is given to the block as the initial condition to give the small disturbance.

Table 6.3 : Dimensions and physical properties for the computation of the falling behavior of a fish reef block.

Parameters	Values (model scale)	Values (prototype scale)
Width of tank : $L_x = L_y$	60 cm	36 m
Height of tank : L_z	200 cm	120 m
Falling height : h	160 cm	96 m
Density of cylinder : ρ	2300 kg/m^3	2300 kg/m^3
Density of water : ρ_w	1000 kg/m^3	1000 kg/m^3
Kinematic viscosity of water : ν	1.0×10^{-6} m^2/s	1.0×10^{-6} m^2/s

The computed falling tracks are shown in Fig. 6.9. The experimental results are also shown in the figure. The time interval of display is 0.2 s. In the numerical result with the coarsest grid (Grid 1), the block began to slide to the left, and the inclination also became large. The falling track is displayed only up to the middle in this case because the computation stopped halfway. Since the computational grid around the block deforms along the movement of the block in this method, a very small cell occurs locally when the deformation of the grid becomes too large. As a result, the computation sometimes stops due to the limitation of the Courant number. In the case of Grid 2, the swing motion reproduced though its amplitude is overestimated. In the case of the finest grid (Grid 3), the amplitude of the swing motion is smaller than that of Grid 2 and almost agrees with the experimental result.

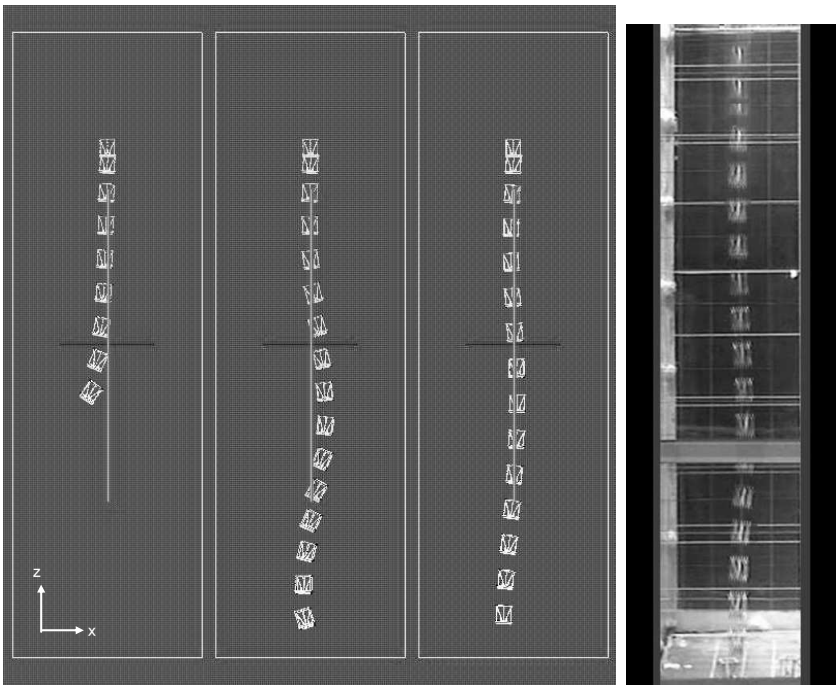

(a) Grid 1 (b) Grid 2 (c) Grid 3 (d) Experiment

Figure 6.9 : Comparison of the falling behavior of the fish reef block. Time interval of display is 0.2 s.

Fig. 6.10 shows a comparison of the settling velocity. The settling velocity in the experiment is the average velocity obtained from the time taken to pass through each interval of 0.2 m in the vertical direction. The computation results almost agree with the experimental one regardless of the computational grid.

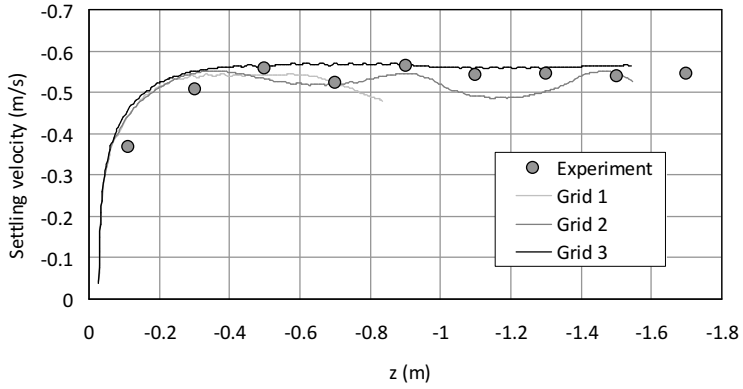

Figure 6.10 : Comparison of the settling velocity.

The above results showed that the present numerical computation method reproduces the falling behavior of the fish reef block with its complicated 3-dimensional shape. Since it was found that the sufficiently fine grid was necessary to reproduce the

falling behavior accurately, the finest grid (Grid 3) is used in the following.

6.3 Development of Fish Reef Block Ensuring Accurate Placement

6.3.1 Laboratory Experiment

Model experiments were conducted to decide a fundamental shape of block which would fall with stable behavior in water. Fig. 6.11 shows the setup of the experiments in quiescent water. The model scale was 1/60. A water tank of 1.0 m square and 2.3 m high was used. The water depth was 2.0 m (120 m in the prototype scale). The model block made of mortar was released gently from just under the water surface. The behavior of the block was recorded with two video cameras from two orthogonal directions. Horizontal lines every 20 cm were marked on the walls of the tank to measure the vertical position and orientation of the blocks from the video images.

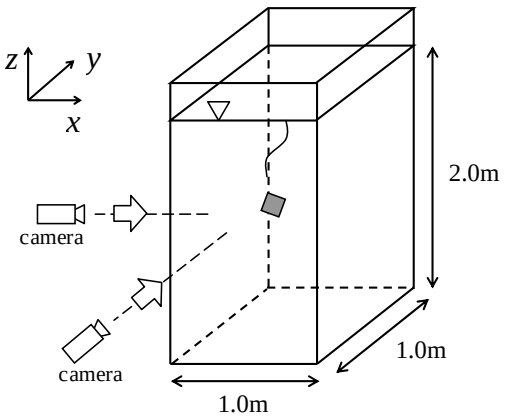

Figure 6.11 : Setup for the experiment in quiescent water.

Several kinds of model blocks with frame structures were tested, for example cubic, prismoid and circular cylinder, etc. The cubic type shown in Fig. 6.12(a) (hereafter the “Base model”) was selected as it fell without rotation and the amplitude of rolling motion was smallest among them. The block was improved by numerical analysis as mentioned below and shown in Fig. 6.12(b) (hereafter the “Improved model”) was also tested. The feature of the “Improved model” is the extra shelf areas attached to the upper and lower frames to act as stabilizers. The tests with the “Improved model” were repeated more than 100 times to investigate the probabilistic distribution of the

placement position.

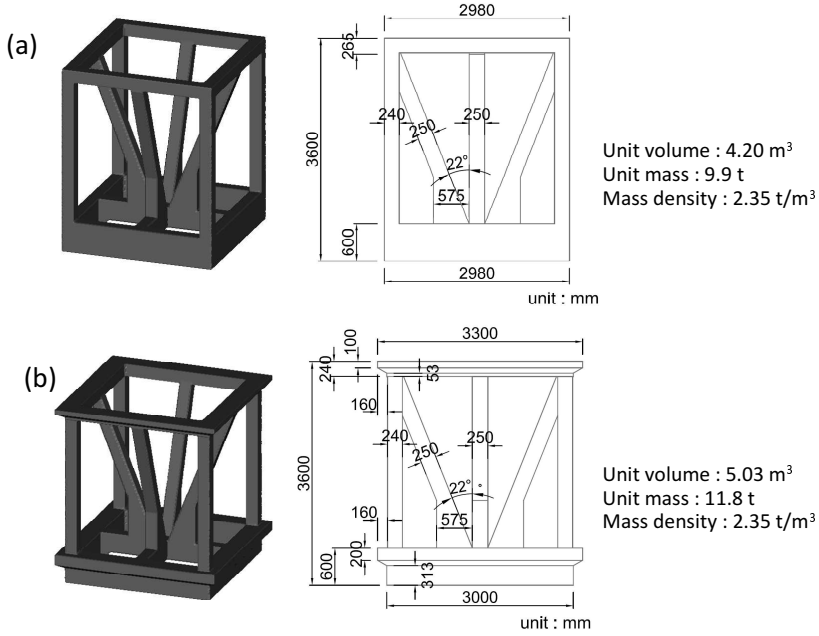

Figure 6.12 : Shapes of the blocks. (a) : Base model. (b) : Improved model.

Because the falling behavior is influenced by the ambient current during actual construction, experiments in a flow field were also conducted. The experimental setup is depicted in Fig. 6.13. A submersible pump was installed in a flume (50 m long, 1.0 m wide, and 1.3 m deep) to generate a steady flow. The water depth was about 0.85 m (51 m in the prototype scale). The target flow velocity was 5 cm/s (0.39 m/s in the prototype scale) and vertically uniform. This velocity corresponds approximately to the current in the assumed sea area measured by Ito et al. (2009). The flow velocity was confirmed by using an electromagnetic current meter before the experiments. The behavior of the block was recorded from the side of the flume with a video camera. The “Improved model” was used and the tests were also repeated more than 100 times.

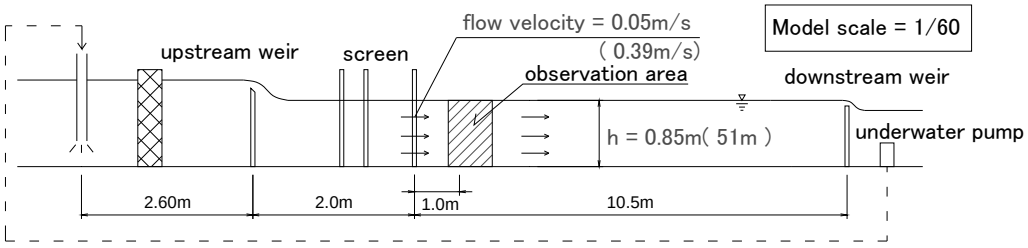

Figure 6.13 : Setup for the experiment in flow field.

Examples of the falling behavior of the block taken by video camera are shown in Fig. 6.14. In the quiescent-water experiment, the block fell almost straight with limited swinging and swaying from side to side. In the flow-field experiment, it fell almost linearly to the downstream side. The block landed vertically in all the tests. The block should land on its bottom on the sea bed to function as a nursery reef. Fig. 6.15 shows the falling tracks of the center of gravity of the block. The horizontal displacement at the bottom (at a depth of 120 m in the prototype) was up to 8.8 cm (5.3 m in the prototype scale) in the quiescent-water experiment. In the flow-field experiment, the average placement position was 8.5 cm (5.1 m in the prototype scale) to the downstream side. The placement variation at the bottom (at a depth of 51 m in the prototype) from the average placement position was ±2.9 cm (±1.7 m in the prototype scale). Considering that the accuracy requested for placement is within a range of 30 m in radius, the developed block can be expected to satisfy this accuracy, although the water depth in the experiment is shallower than the planned water depth, and the ambient current may exceed 0.4 m/s, occasionally.

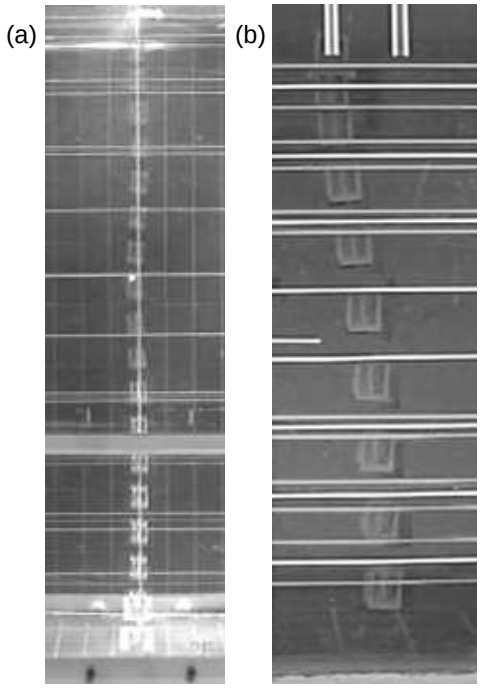

Figure 6.14 : Examples of falling behavior of the block taken by video camera. (a) : In quiescent water. (b) : In flow field. Time interval of display is 0.2 s.

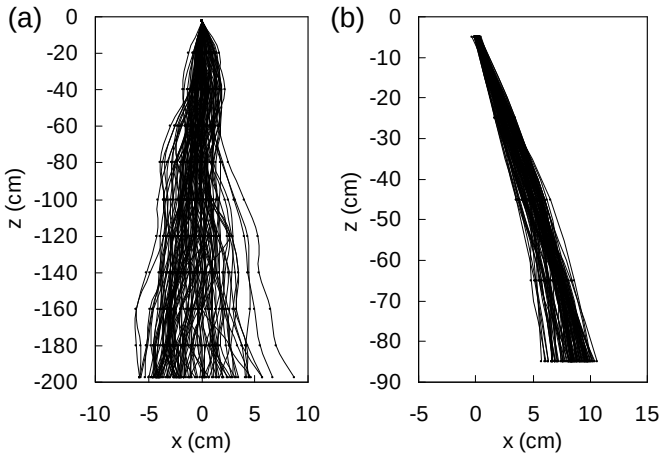

Figure 6.15 : Falling tracks of the block. (a) : In quiescent water. (b) : In flow field.

6.3.2 Stabilization of Falling Behavior by Improving the Block Shape

The features of the “Improved model” is the extra shelf areas attached to the upper and lower frames to act as stabilizers as shown in Fig. 6.12. The effect of these stabilizers was investigated. Fig. 6.16 shows the comparison of the computed falling behavior of the “Improved model” and the “Base model”. The experimental results are also shown in Fig. 6.16. The amplitude of the swing motion has been reduced by the stabilizers. The amplitude of the swing motion is overpredicted for the “Base model”, but the falling behavior of the “Improved model” is well predicted.

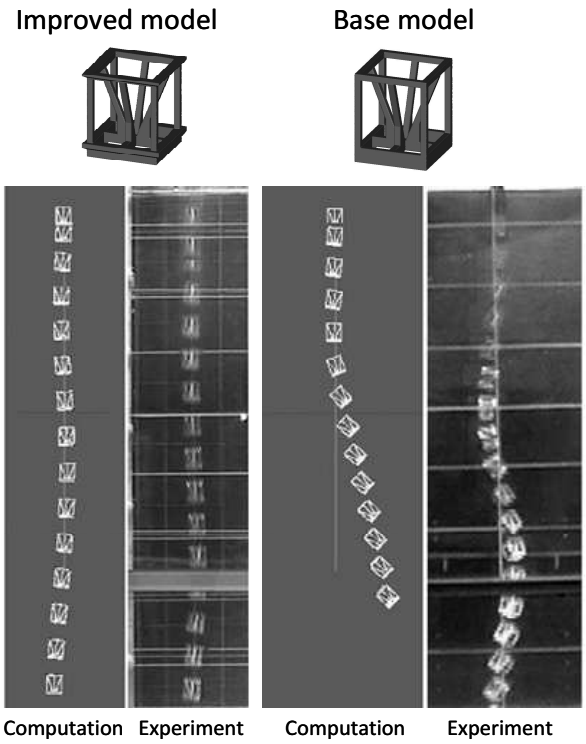

Figure 6.16 : Comparison of the falling behavior of the “Improved model” and “Base model”. Time interval of display is 0.2 s.

The reduced swing motion of the “Improved model” results in the increased settling velocity. The horizontal displacement of the “Improved model” by the ambient current will be reduced with the decrease of the settling duration. The reduced amplitude of the swing motion also implies that the distribution range of the placement position will be smaller, and the probability of landing on the block bottom on the sea bed will be larger. Therefore, the block should be shaped in such a way that the block settles downward as fast as possible with minimum swing motion and minimum horizontal displacement from the ambient current. Fig. 6.17 shows a comparison of the computed settling velocities and the rotating angles of the “Improved model” and the “Base model”. Fig. 6.17(a) shows the settling velocity increase as a result of the stabilizers. Fig. 6.17(b) shows that the rotating angle of the “Improved model” is less than 10°, whereas the “Base model” may rotate up to 45°.

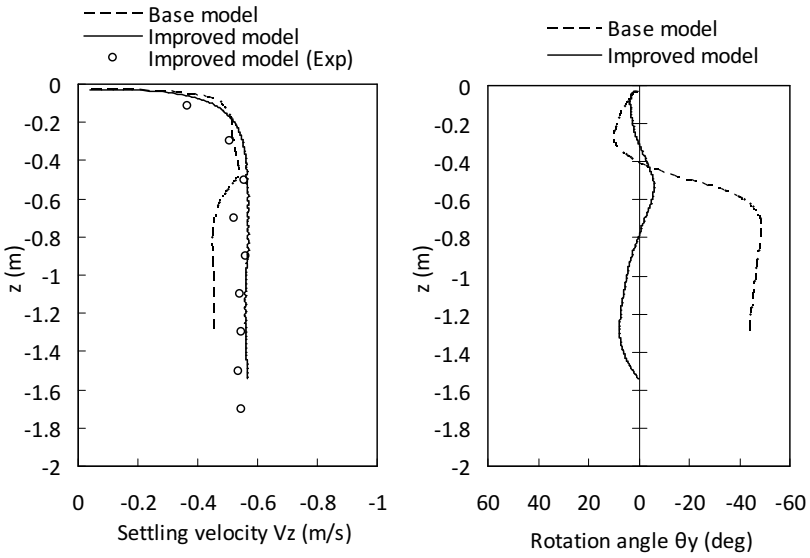

Figure 6.17 : Comparison of the (a) settling velocities and (b) rotation angles.

The mechanism of stabilization due to the stabilizers was investigated by analyzing the pressure and velocity fields. Fig. 6.18 shows the spatial distribution of the dynamic pressure, which is defined as the difference between the computed total pressure and hydrostatic pressure. The cross section of the block (see Fig. 6.12) in the plane $y = 0$ is shown in white. The stabilizers decrease the dynamic pressure around the upper stabilizer in the wake zones, accordingly the upper stabilizer is pulled upward. This suggest that the upper stabilizer has the effect of suppressing the block inclines as shown in Fig. 6.19.

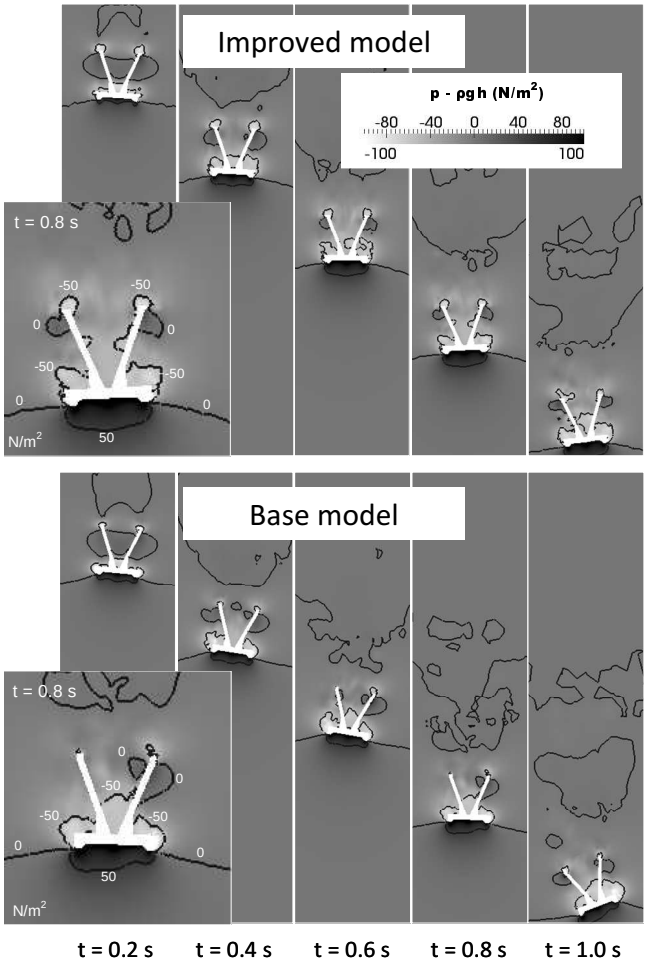

Figure 6.18 : Spatial distribution of dynamic pressure.

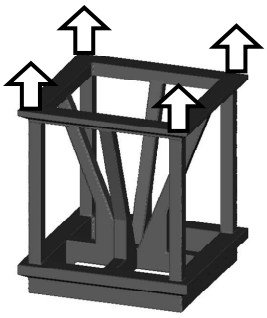

Figure 6.19 : Schematic diagram of the stabilization due to the upper stabilizer

Fig. 6.20 shows the spatial distribution of the magnitude of the velocity. The stabilizers make the flow field more symmetric about the diagonal members of the block. The symmetry of the flow field around the “Base model” is broken soon after release. The diagonal member on the right side of the “Base model” is out of the wake zone at time t = 0.6 s (4.2 s in the prototype scale). For the pressure distribution at t =

0.6 s, a large restoring moment is acting on the diagonal member on the right side of the "Base model". The block then rotates in the opposite direction at t = 1.0 s. This suggests that the lower stabilizer may stabilize the falling behavior by maintaining a symmetric wake zone.

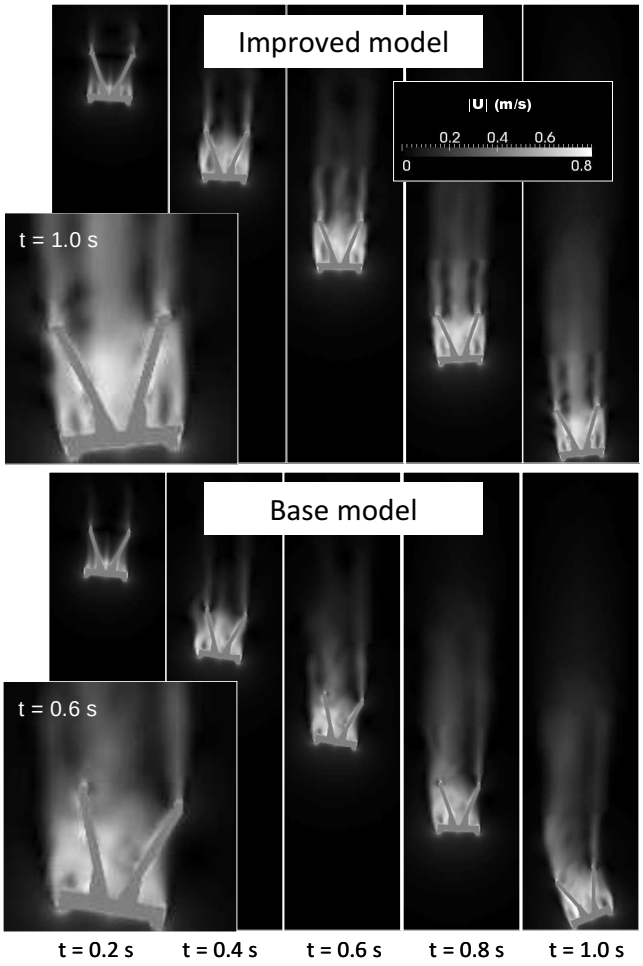

Figure 6.20 : Spatial distribution of velocity magnitude.

Hydrodynamic stability was analyzed by using the computed hydrodynamic forces in steady flow. To keep a stable falling behavior, the center of pressure defined below must be above the center of gravity. The center of pressure is defined as the point on a body where the total pressure field acts, causing a force and no moment about that point. Fig. 6.21 shows the center of pressure at each angle of flow. The center of pressure of the "Base model" lowers to near the center of gravity at an angle of 30°, whereas it is located higher on the whole in the "Improved model".

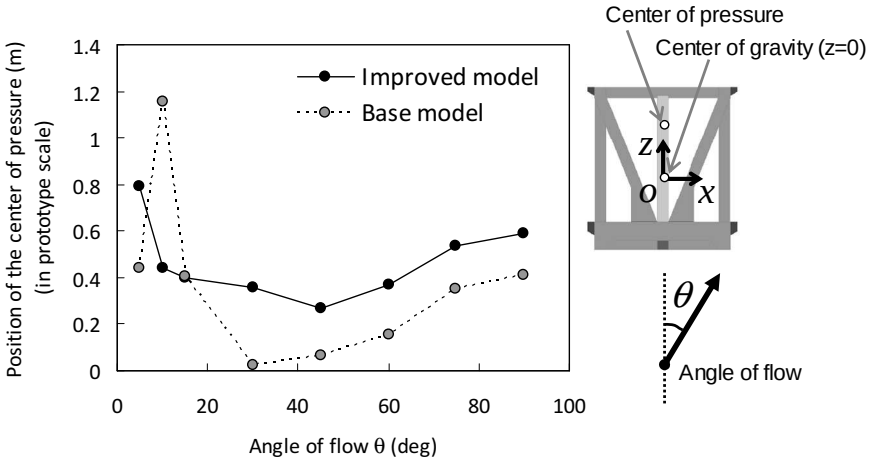

Figure 6.21 : Position of center of pressure.

6.3.3 Influence of Initial Posture on Falling Behavior

Because the block may be released in a tilted posture in actual construction, the influence of the initial posture on falling behavior was investigated numerically. Block tilts of 2, 5, and 10° were specified as the initial condition. The other conditions of the computation were the same as before (see Table 6.3). Fig. 6.22 shows the falling tracks and rotation angles. The swing amplitude and rotation angle do not increase as much as the increased initial tilt. The maximum horizontal displacement and maximum rotating angle for the case of 10° of tilt is about 0.05 m (3.0 m in the prototype scale) and 20°, respectively. The stabilizers reduce the effect of initial tilt on subsequent falling behavior.

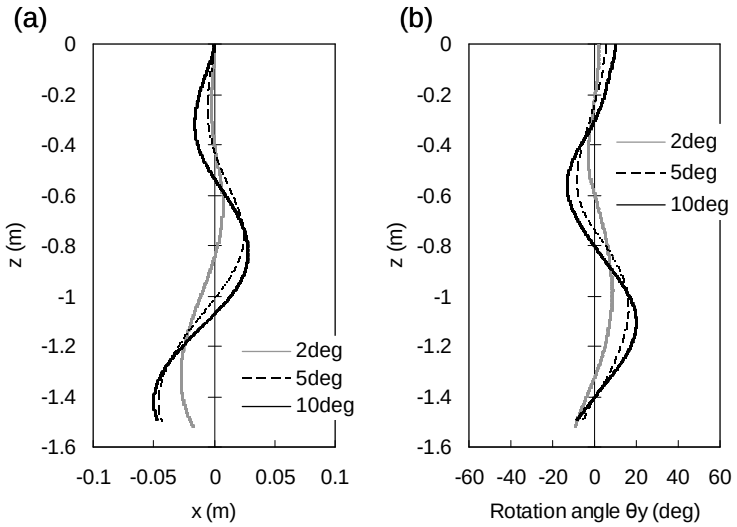

Figure 6.22 : Influence of initial posture on (a) falling tracks and (b) rotation angles.

6.3.4 Prediction of the Distribution of Placement Position by Stochastic Model

Placement in the water at a depth of 250 m could not be obtained because of the limitations of the water-tank size. The variation of placement position was investigated using a stochastic model. The stochastic model by Matsumi and Kimura (1992) was applied. The model assumes that the horizontal displacement of the settling block at a given elevation follows the Gaussian distribution, which is independent of block elevation. The model also assumes a Markov-chain theory with respect to horizontal displacement, where the next state depends only on the current state without regard to the preceding sequence of events.

First, the probabilistic distributions of the horizontal displacement Δx and Δy between the two elevations were investigated by analyzing the experimental data. Fig. 6.23 shows the standard deviation (SD) of Δx and Δy as a function of elevation z. The elevation spacing Δz was 0.2 m (12 m in the prototype scale). The normalized SD is plotted in Fig. 6.23 by dividing it by the length of the block L, which was 5.5 cm (3.3 m in prototype scale). The SD is found to be almost constant independent of its elevation. Because the average of the normalized SD in the flow-field experiments was 0.101 and slightly smaller than 0.131 in the quiescent-water experiment, the ambient current tended to reduce the horizontal displacement variation.

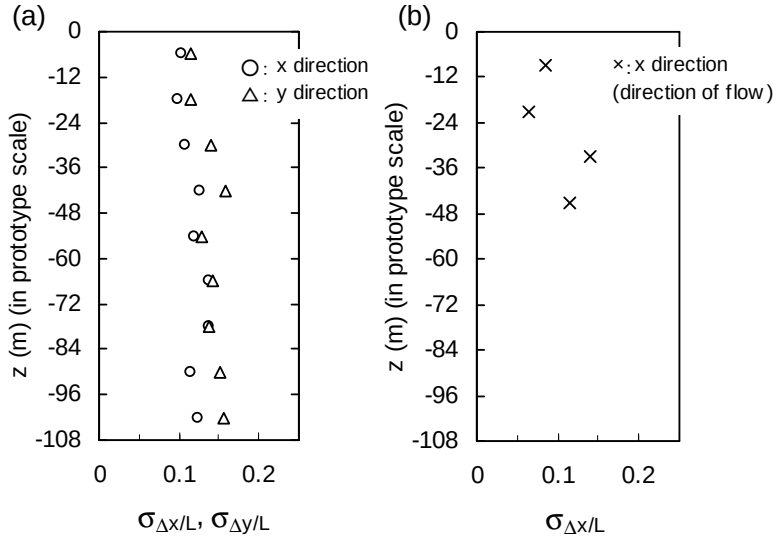

Figure 6.23 : Standard deviation of the non-dimensional horizontal displacement $\Delta x/L$ and $\Delta y/L$. (a) : In quiescent water. (b) : In flow field.

Secondly, the distributions of Δx and Δy in the quiescent-water experiment were

confirmed based on whether approximation by a Gaussian distribution could be done. Fig. 6.24 shows examples of the results. The mean value of the Gaussian distribution was set to zero and the SD was set to the mean value in the quiescent-water experiments which was 0.131. It can be seen that the Gaussian distribution fitted reasonably well with the measured distributions.

According to the Markov-chain theory, if the probability distributions of the horizontal position $f(x)$ at $z = z_0$ and Δx (written as $g(x)$) are given, $f(x)$ at $z = z_0 + \Delta z$ can be obtained as follows:

$$f(x)\Big|_{z=z_0+\Delta z} = \int_{x_0=-\infty}^{x_0=\infty} g(x_0 - x)\, f(x)\Big|_{z=z_0} dx_0 \,. \tag{6.1}$$

Also, $g(x)$ is a Gaussian distribution written as

$$g(x) = \frac{1}{\sqrt{2\pi\sigma^2}} \exp\left[-\frac{(x-\mu)^2}{2\sigma^2} \right], \tag{6.2}$$

where, μ is the mean value (= 0.0), and σ is the SD (= 0.131). The distribution of the horizontal position at arbitrary elevations can be obtained by solving Eq. (6.1) sequentially from $z = 0$. Fig. 6.25 shows the calculated results in comparison with the experimental results. This model reproduces the distribution spreading with the block falling distance. In a water depth of 252 m, the range of 99% nonexceedance probability is predicted to be ±5.1 m. Because the accuracy requested for placement is a range within 30 m in radius, the distribution range resulting from the swing motion of the block in still water is found to be small enough.

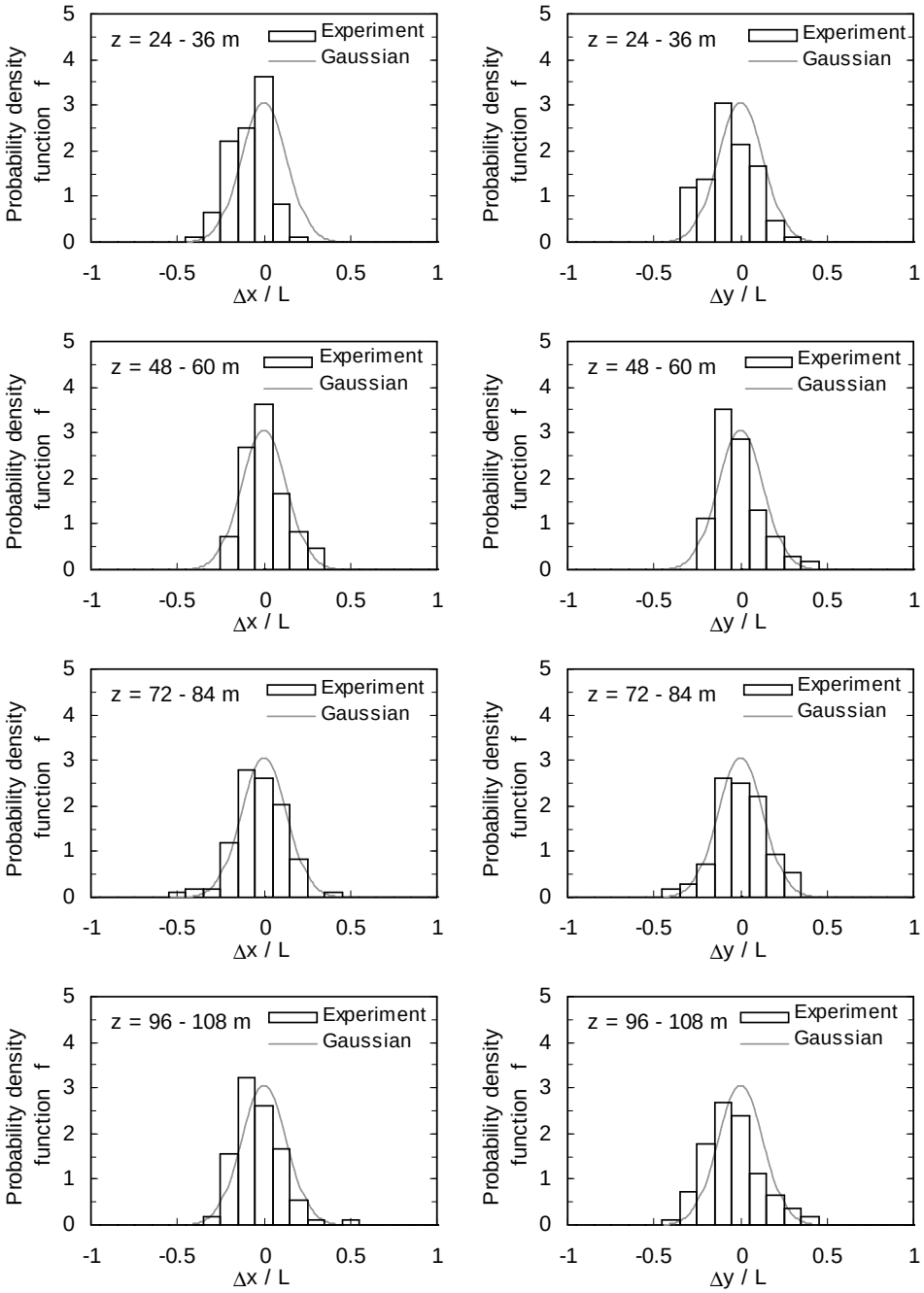

Figure 6.24 : Comparison of the measured distribution of the horizontal displacement Δx , Δy and the Gaussian distribution.

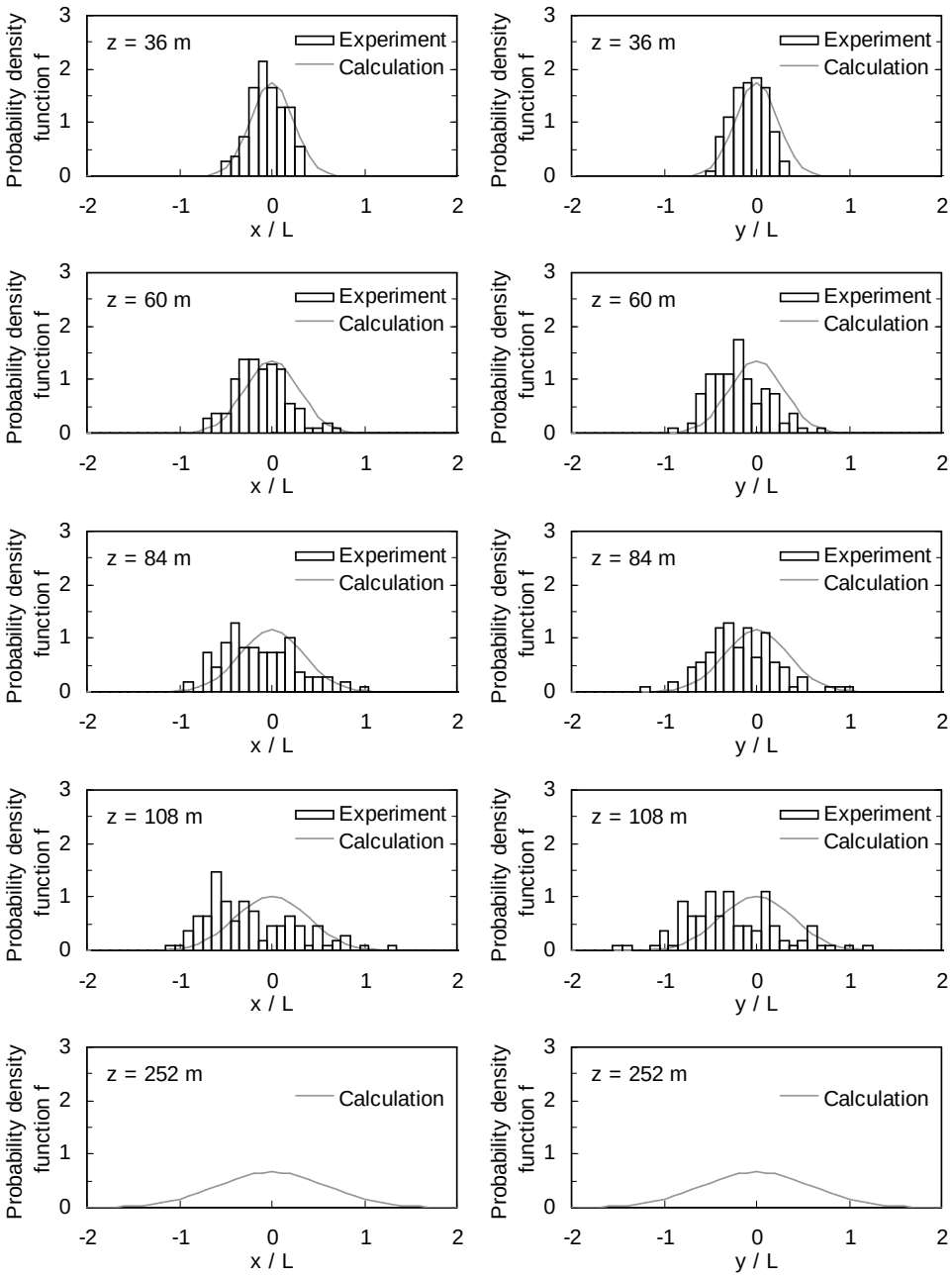

Figure 6.25 : Probabilistic distribution of the horizontal position.

6.4 Development of Quick Estimation Method for the Placement Position

Placement of the blocks can be done in the following steps:

1. The floating crane navigates slowly near the release location.

2. Flow at the site is measured using an Acoustic Doppler Current Profiler (ADCP).
3. The release point is calculated accounting for crane velocity and flow conditions.
4. The block is released.

It is necessary to forecast the placement position quickly because the release point needs to be determined on the floating crane. The computational method based on the Navier-Stokes equation is not suited for such an application. Therefore, a quick estimation method was developed for field applications.

6.4.1 Estimation Method for Averaged Placement Position

To reduce the computational time, the hydrodynamic force acting on the block was evaluated using the hydrodynamic force coefficients instead of computing the pressure field based on the Navier-Stokes equation. In addition, the rotational motion of the block was neglected since the rotational motion could be considered not to influence on the average placement position so much.

Fig. 6.26(a) shows the coordinate system for the calculation. Kumagai et al.(2004) proposed a prediction method for the falling behavior of a block. In their method, the hydrodynamic force acting on the block was evaluated by using the drag-force coefficient. In this study, transverse hydrodynamic forces were included to predict the transverse block motion.

The equation of motion is written as :

$$\left(M+\rho_w k_m V\right)\frac{d\mathbf{v}_b}{dt}=\mathbf{F}+\left(M-\rho_w V\right)\mathbf{g}, \tag{6.3}$$

where M is the mass of the block, ρ_w is the density of water, k_m is the added mass coefficient, V is the volume of the block, $\mathbf{v}_b$ is the velocity of the block, $\mathbf{F}$ is the hydrodynamic force, and $\mathbf{g}$ is the gravitational acceleration vector acting downward. The hydrodynamic force is expressed as

$$\mathbf{F}=\frac{1}{2}C_D\rho_w A\left|\mathbf{v}_r\right|^2\mathbf{l}+\frac{1}{2}C_L\rho_w A\left|\mathbf{v}_r\right|^2\mathbf{m}+\frac{1}{2}C_S\rho_w A\left|\mathbf{v}_r\right|^2\mathbf{n}, \tag{6.4}$$

$$\mathbf{v}_r=\mathbf{v}_w-\mathbf{v}_b, \tag{6.5}$$

where C_D, C_L, and C_S are the hydrodynamic force coefficients, $\mathbf{v}_w$ is the flow velocity, $\mathbf{v}_r$ is the flow velocity relative to the moving block (see Fig. 6.26(b)), A is the representative area of the block (= 16.19 cm^2 in model scale), which is defined as the projected area viewed from the z-axis, and **l**, **m**, and **n** are the unit vectors. The flow velocity does not include the wave-induced velocity because the flow velocity used for the prediction during actual construction is an average value for tens of seconds of the

velocity measured by ADCP. The vector **l** is in the direction of the relative flow velocity, and **m** is defined as the vector perpendicular to **l** and **n**, with **n** defined as the vector perpendicular to the relative flow vector $\mathbf{v}_r$ and the *z*-axis. Therefore, **l**, **m**, and **n** can be expressed as follows:

$$\mathbf{l} = \frac{\mathbf{v}_r}{|\mathbf{v}_r|}, \tag{6.6}$$

$$\mathbf{m} = \frac{(\mathbf{k} \times \mathbf{v}_r) \times \mathbf{v}_r}{|(\mathbf{k} \times \mathbf{v}_r) \times \mathbf{v}_r|}, \tag{6.7}$$

$$\mathbf{n} = \frac{\mathbf{k} \times \mathbf{v}_r}{|\mathbf{k} \times \mathbf{v}_r|}, \tag{6.8}$$

where **k** is the unit vector in the direction of the *z*-axis. The hydrodynamic force coefficients C_D, C_L, and C_S are obtained beforehand by the method which will be described below. The coefficients depend on the direction of the relative flow velocity. The direction is expressed by the two angles, θ_V and θ_H, where θ_V is the angle between the relative flow velocity and the *z*-axis, and θ_H is the angle between the *x*-axis and the component of the relative velocity in the *xy*-plane, as shown in Fig. 6.26(c). Eq. (6.3) is solved using the Newmark-β method, which is an implicit time-marching method. The values of C_D, C_L, and C_S are updated at every time step after computation of the direction of the relative flow velocity $\mathbf{v}_r$.

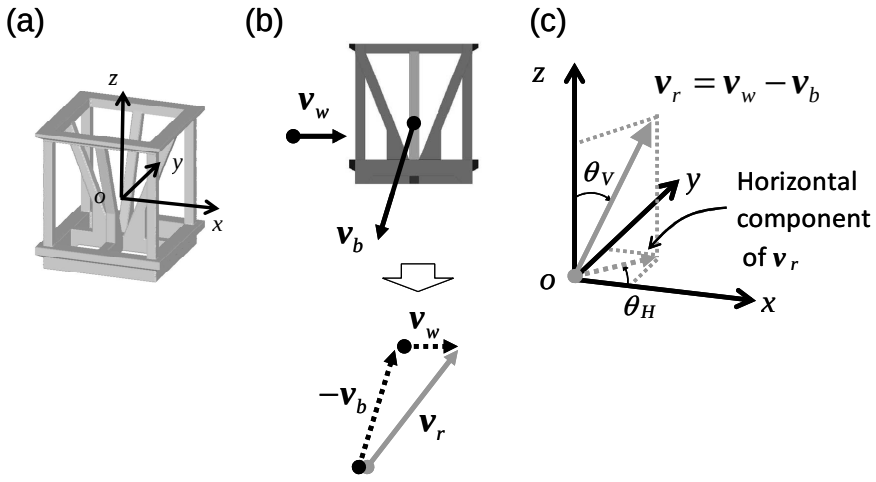

Figure 6.26 : Definition of (a) coordinate system, (b) relative flow velocity, and (c) direction of relative flow velocity.

The hydrodynamic force coefficients C_D, C_L, and C_S were obtained by computing the hydrodynamic force acting on a block fixed in a steady flow. As shown in Fig. 6.27,

the block was placed at the center of the computational domain of 0.6 m × 0.6 m × 0.6 m. A spatially uniform flow of 1.0 m/s was given at the lower boundary of the computational domain. The C_D, C_L, and C_S for each direction was computed with varying the angle of the block. An incompressible flow solver in the OpenFOAM model was used. The range of the Reynolds number during the free-fall in the model and the prototype scale is from 10^4 to 10^7. Since the preliminary computation clarified that the drag coefficient was almost constant in this range of the Reynolds number, the influence of the Reynolds number on the hydrodynamic force coefficients was disregarded. Fig. 6.28 shows the computed coefficients. For computation of the falling track, linearly interpolated values of the coefficients are used.

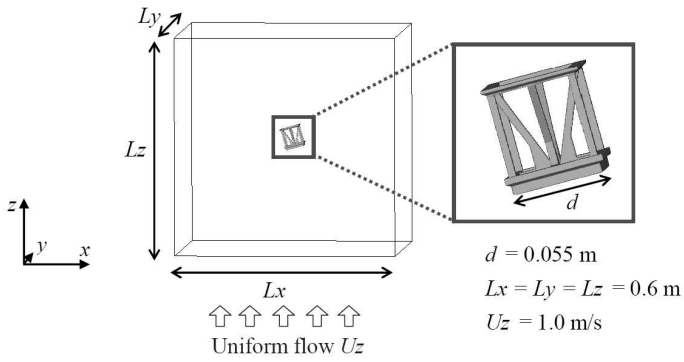

Figure 6.27 : Computational domain for the computation of the hydrodynamic force coefficients.

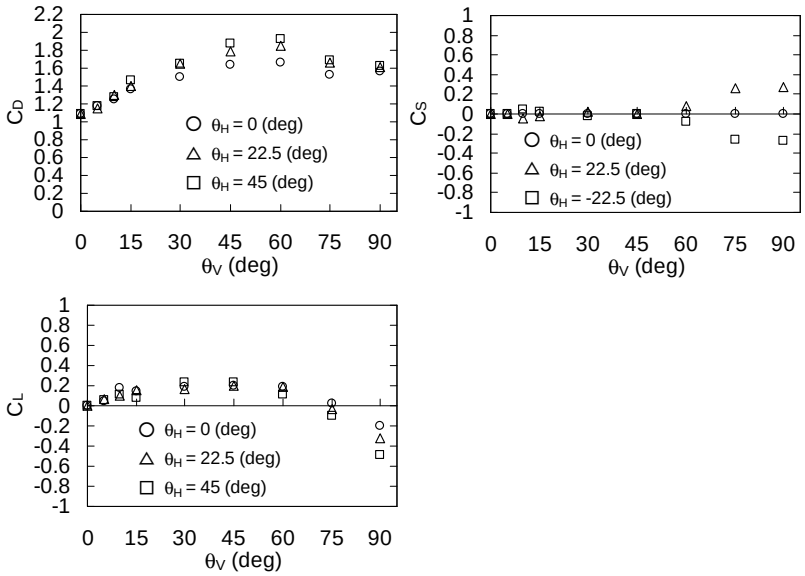

Figure 6.28 : Hydrodynamic force coefficients of the “Improved model”.

Similarly, the added mass coefficient k_m was calculated. The spatially uniform flow accelerating at 1 m/s^2 was given at the lower boundary. The added mass coefficient was assumed as a constant value independent of the angle of the block. It was obtained as 4.6.

6.4.2 Validation of the Estimation Method

To validate this estimation method, the calculated falling behavior in a flow field was compared with the computational result based on the Navier-Stokes equation and experimental ones . The flow velocity was 5 cm/s (0.39 m/s in the prototype scale) and vertically uniform. The calculation condition is shown in Table 6.4.

Table 6.4 : Calculation conditions.

Parameter	Value
Time integration method	Newmark-β (β = 0.1666)
Time increment Δt	0.001 s
Density of block ρ	2300 kg/m^3
Density of water ρ_w	1000 kg/m^3
Added mass coefficient k_m	4.6
Flow velocity (x direction) $\mathbf{v}_w$	5 cm/s (0.39 m/s in the prototype scale)

Fig. 6.29(a) shows a comparison of the falling track. Because the rotational motion is neglected, the oscillating behavior cannot be reproduced in this method. However, the average falling track can be sufficiently predicted. Fig. 6.29(b) shows a comparison of the settling velocity. The result of the quick estimation method agreed well with the experimental result and the computed one based on the Navier-Stokes equation. In addition, since the computational time decreased to a few seconds, this estimation method for placement position can be applied on site.

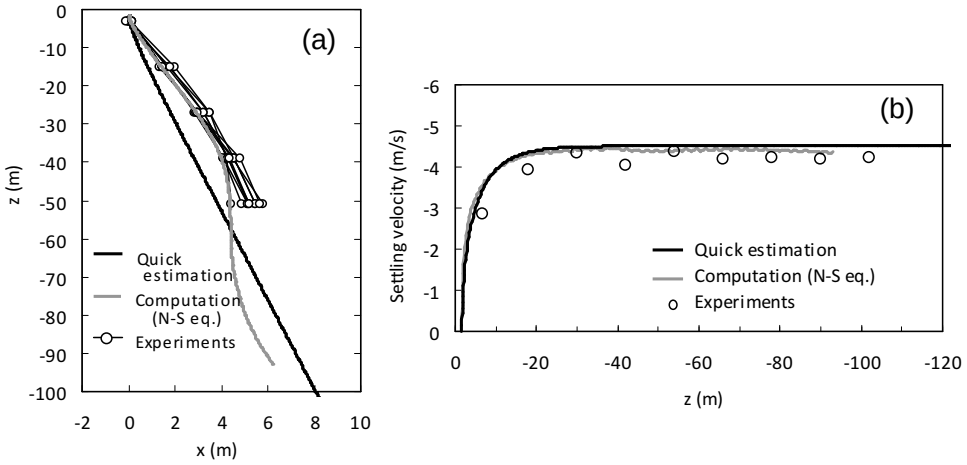

Figure 6.29 : Comparison of (a) falling tracks and (b) settling velocities in flow field.

6.5 Closure

This chapter presented an economical placement method for fish reef blocks utilizing free fall in the deep sea. The main conclusions are shown below:

1. Numerical computational method to analyze the falling behavior of fish reef blocks in water was investigated. The method was validated by comparing with experimental results.
2. A new fish reef block which falls with stable behavior through water was developed by laboratory experiments and numerical computation. The newly developed block is based on a cube-shaped frame structure with extra shelf areas attached to the upper and lower frames to act as stabilizers.
3. The computation results indicated that the upper stabilizer produced a restoring moment for the tilted block by decreasing the dynamic pressure around the upper stabilizer, and the lower stabilizer reduced instability in the wake of the falling block by maintaining a symmetric wake zone.
4. A stochastic model based on experimental results showed that the distribution of the placement position as a result of the swing motion was sufficiently small and well within the required accuracy.
5. A quick prediction method for the placement position was developed to determine the release point of the block during actual construction in the presence of ambient current. Use of the hydrodynamic force coefficients computed in advance will allow

the method to estimate the average falling track of the block with sufficient accuracy and within a few seconds.

References

Fisheries Agency of Japan (2007) : Outline of the development plan of fishing ports and grounds implemented by the national government in the western part of the Sea of Japan,http://www.jfa.maff.go.jp/j/gyoko_gyozyo/g_zyoho_bako/tokutei/pdf/sub82_001.pdf (*in Japanese*), (accessed 2014-12-21).

Fisheries Agency of Japan, Construction Division (2007) : Document for explanation to the prefectures on budget requests for FY2008, October 2 2007, http://www.jfa.maff.go.jp/j/gyoko_gyozyo/g_thema/pdf/sub3954.pdf (*in Japanese*), (accessed 2014-12-21).

Fisheries Agency of Japan, Fisheries Infrastructure Department (2008) : Development manual of fishing grounds implemented by the national government (draft), Section of nursery reefs for snow crab and flathead flounder, January 31 2008, http://www.jfa.maff.go.jp/j/gyoko_gyozyo/g_thema/pdf/sub3927.pdf (*in Japanese*), (accessed 2014-12-21).

Fisheries Agency of Japan, Resources Enhancement Promotion Department (2013) : Resource evaluation of snow crabs in the Sea of Japan in FY2013 , http://abchan.job.affrc.go.jp/digests25/details/2516.pdf (*in Japanese*), (accessed 2014-12-21).

Inada T., Oka, S., Nakamura, T., Yanase, T., Takeuchi, K., Yoshida, R. (2009) : Development of a fish reef block detection and guidance system in a large depth of water, *Journal of Coastal Zone Studies*, **22** (2), 89-99 (*in Japanese*).

Ito, Y., Matsumoto, T., Oshitani M. (2009) : The water quality and flow regime in the western Sea of Japan and the vicinity of the Tsushima island, *Annual Journal of Civil Engineering in the Ocean, JSCE*, **25**, 77-82 (*in Japanese*).

Ito, Y., Miura, H., Nagahama, T., Ohno, Y., Yanase, T., Nakamura, T. (2008) : Evaluation of the function of protective developmental reefs for snow crabs *Chionoecetes opilio*, *Annual Journal of Civil Engineering in the Ocean, JSCE*, **24**, 25-30 (*in Japanese*).

Jasak, H., Tukovic, Z. (2007) : Automatic meth motion for the unstructured finite volume method, *Transactions of FAMENA*, **30 (2)**, 1-18.

Kumagai, T., Yamamoto, S., Hirayama, T., Manabe, T., Shimizu, H., Kawaguchi, T., Hirata, K., Komiya, K., Kobayashi, K. (2004) : Movement of cube blocks dropped from barge vessel to construct artificial marine ridge, *Annual Journal of Coastal Engineering, JSCE,* 51, 801-805 (*in Japanese*).

Matsumi, Y., Kimura, A. (1992) : Hydraulic approach to determining optimum interval of discharge sites of barge in constructing rubble foundation of deep water breakwater, *Proceedings of 23rd International Conference on Coastal Engineering*, Venice, Italy, pp.3149-3162.

Matsumi, Y., Seyama, A. (1988) : The fundamental study to reduce the settled area of the fish aggregation devices on the sea floor thrown from a ship, *Proceedings of 21st International Conference on Coastal Engineering*, Torremolinos, Spain, pp.2937-2951.

Nakamura, T., Oka, S., Yamamoto, R., Yanase, T., Asakawa, N., Nakagawa, Y. (2008) : The political meaning and the technical issues on development of offshore artificial fishing grounds, *Fisheries Engineering*, **45** (1), 67-74 (*in Japanese*).

OpenFOAM, http://www.openfoam.com/

Ushijima, S., Takemura, M., Yamada, S., Nezu, I. (2003) : Computational method for multiphase incompressible flows (MICS) and its applicability to particle-laden liquid flows, *Proceedings of the Japan Society of Civil Engineers*, (740/II-64), 121-130 (*in Japanese*).

Chapter 7

Summary and Conclusions

In this thesis, a design method has been presented for armor units covering rubble mound of composite breakwaters. An economical construction method for artificial reefs in the deep sea has been also presented. These design and construction methods were developed by introducing the CFD approach in addition to the hydraulic model experiments. In the following, a summary of the previous Chapters and future work are described.

7.1 Summary

In Chapter 1, the background, the objective of this study, and the thesis outline were described.

In Chapter 2, a versatile numerical wave flume was developed by using an OpenFOAM based on an unstructured grid.

- The validation of the water surface profile and wave forces acting on a structure were confirmed through the dam-break tests.
- It was confirmed that wave generation method by reproducing a motion of a wavemaker could generate the waves accurately and that the processes of wave propagation, deformation, and wave breaking could be reproduced appropriately. The computed wave height in the surf zone tended to be underestimated. This was improved to some extent by setting the aspect ratio of the computational grid to 1:1.
- The total volume of water in the computational domain was conserved well in this wave-generation method. This is an advantage in performing a long-time simulation. A future challenge will be to introduce a function of active generating-absorbing for

long-time simulation.

- The validation of the porous model was examined through the following two tests: (1) the wave transmission coefficient of a sloping breakwater and (2) the effectiveness of a detached breakwater against tsunami. The overall trend of the computed results agreed with the experimental ones. Further study is required on the value of the material constants and the formulation of the resistance coefficients for the improvement of the accuracy.

In Chapter 3, stability of the armor units against overtopping jet caused by tsunami with rapid water level rise was examined.

- When the tsunami with rapid water level rise overtopped the breakwater and impinged onto the harbor-side water surface, the water jet generated vortices. The armor units received uplift forces when the vortex passed through above the armor units.
- The flat-type armor block with large holes showed high stability against the water jet in the experiments. Numerical analysis revealed that the holes in the blocks reduce the uplift force acting on the block and improve the stability against impinging water jet.
- Reinforcement by placing heavier blocks along the toe of the slope enhanced the total stability of the armor layer.
- The wave profile of the tsunami and the impinging jet were accurately reproduced by numerical computation based on the VOF method.
- The stability of the armor blocks was predicted qualitatively by numerical analysis which took the 3-dimensional shape of the block into account.

In Chapter 4, stability of the armor units against steady overflow of tsunami was investigated.

- Two important factors for armor stability were found. These were the impingement position of the overflow jet and the harbor-side water level.
- Two failure modes of overturning and sliding were observed in the experiments. Numerical analysis revealed that the stability was predicted by the balance of the moment of a block in the case of overturning mode. In the sliding mode, it was necessary to consider the balance of forces of all the blocks on the slope.
- Wave-dissipating blocks installed in two layers showed a toughness against tsunami, namely, scouring was hard to progress rapidly even when many blocks displaced.
- The harbor-side flow field was favorably reproduced by the following numerical

computation method: (1) The overflow nappe above the water surface and the flow field on the harbor-side were solved separately to avoid excessive entrainment of air. (2) The calculation of the overflow jet was carried out by either a simple method based on an empirical formula or a numerical method using a VOF model. (3) The RSM was used as a turbulence model for the computation of the harbor-side flow field. The turbulence inside the rubble mound was set to zero to avoid excessive generation of the turbulence at the surface of the mound.

In Chapter 5, the applicability of the Isbash formula, which is the conventional design method for the armor units based on the flow velocity, against tsunami overflow was examined. Also a more practical design method was presented.

- The applicability of the Isbash formula by CERC (1977) against armor stones has been confirmed from the result that the relationship between the Isbash constant and the degree of damage of armor stone almost agreed with that of the past study.
- In the case of concrete blocks, the Isbash constant depends on the width of the water jet.
- The formula by CERC (1977) tends to overestimate the slope effect in the case of concrete blocks. The formula by Isbash (1932) takes the slope effect into account more properly.
- A new practical design method for the armor units against tsunami overflow has been proposed. The features of the method are the following: (1) Overflow depth is used to represent the external force and this enables the calculation more easily and robustly than the conventional method using flow velocity. (2) Two formulae are used corresponding to the two failure modes of overturning and sliding. (3) The influence of the impingement position of the water jet and the influence of the harbor-side water level are taken into account.
- The validity of the new method was confirmed by comparing with the experimental results.
- Examples of design calculation of the armor units were shown for the two methods, the Isbash formula and the newly proposed method.

In Chapter 6, an economical placement method for fish reef blocks utilizing free fall in the deep sea was presented.

- Numerical computational method to analyze the falling behavior of fish reef blocks in water was investigated. The method was validated by comparing with experimental results.

- A new fish reef block which falls with stable behavior in water was developed by laboratory experiments and numerical computation. The newly developed block is based on a cube-shaped frame structure with extra shelf areas attached to the upper and lower frames to act as stabilizers.
- The computation results indicated that the upper stabilizer produced a restoring moment for a tilted block by decreasing the dynamic pressure around the upper stabilizer, and the lower stabilizer reduced instability in the wake of the falling block by maintaining a symmetric wake zone.
- A stochastic model based on experimental results showed that the distribution of the placement position as a result of the swing motion was sufficiently small and well within the required accuracy.
- A quick prediction method for the placement position was developed to determine the release point of the block during actual construction in the presence of ambient current. Use of the hydrodynamic force coefficients computed in advance will allow the method to estimate the average falling track of the block with sufficient accuracy and within a few seconds.

7.2 Future Work

Numerical wave flume

In this study, the stability of the armor blocks were analyzed based on the fluid force acting on each block. A computation method for solving the movement of the blocks directly is required for the improvement of the accuracy.

When applying the wave generation method by reproducing motion with a wavemaker, the function of simultaneously generating incident waves and absorbing the reflected waves is required for the long-time simulation. This can be done by applying existing theories (e.g., Hirakuchi et al., 1990; Frigaard and Christensen, 1994).

As for the porous model, as indicated above, further investigation is required on the value of the material constants and the formulation of the resistance coefficients for the improvement of the accuracy.

Tsunami-resistant design of breakwaters

Expansion of the applicability of the newly proposed design method for armor units will be a future project. Because this method is limited to rectangular caissons at the moment,

it is desirable to increase the applicable range to various shapes of superstructures. The influence of the shape of superstructures on the armor stability has to be clarified. A possible way to incorporate this influence is to introduce a correction coefficient into the stability number.

As for the numerical analysis on the stability of armor blocks, it is necessary to perform validation for more cases. It may become possible to apply to the development of the block shape with higher stability and the calculation of the stability numbers for the block.

Though the present study was focused on the stability of armor units, a comprehensive stability of breakwaters, which includes the sliding of caissons, and scouring of the rubble mound and subsoil is also important.

In addition, the stability of armor units against the water jet due to a tsunami with rapid water level rise has not yet been fully revealed. The influence of the shape of tsunami, e.g., breaking bore, tsunami with soliton fission, on armor stability should be investigated. The influence of the dimensions of the harbor-side mound and the harbor-side water level will also be important for armor stability.

Artificial reefs

Application of the developed method of this study to the construction of artificial upwelling mounds can be expected. Artificial upwelling mounds have been constructed on the sea bottom to generate upwelling currents artificially aiming at increasing offshore fishery resources. The construction of such upwelling mounds in the deep sea area has been planned, and the establishment of an accurate placement method is an issue (Nakamura et al., 2008). The findings of the study herein are considered to be useful for the purposes of the investigation of the accurate placement.

References

Coastal Engineering Research Center (1977) : Shore Protection Manual, U.S.Army Corps of Engrs., U.S.Govt. Printing Office, Vol. II, 7_213-7_216.

Frigaard, F., Christensen, M. (1994) : An absorbing wave-maker based on digital filters, *Proceedings of 24th International Conference on Coastal Engineering*, Kobe, Japan, 168-180.

Hirakuchi, H., Kajima, R., Kawaguchi, T. (1990) : Application of a piston-type

absorbing wavemaker to irregular wave experiments, *Coastal Engineering in Japan*, **33** (1), 11-24.

Isbash, S.V. (1932) : Construction of dams by dumping stones into flowing water, Sci. Res. Inst. Hydrotech. Leningrad, Translated by A. Dovjikov, U.S.Army Corps of Engineers, 1935.

Nakamura, T., Oka, S., Yamamoto, R., Yanase, T., Asakawa, N., Nakagawa, Y. (2008) : The political meaning and the technical issues on development of offshore artificial fishing grounds, *Fisheries Engineering*, **45** (1), 67-74 (*in Japanese*).

OpenFOAM, http://www.openfoam.com/

Acknowledgements

I would like to express my gratitude to my supervisor, Prof. Kazuo Nadaoka, for his continuous support and guidance since I was an undergraduate student. I am deeply grateful for guiding me to the research field of coastal engineering. I would also like to thank to dissertation committee members: Prof. Toshihiro Osaragi, Prof. Shinjiro Kanae, Assoc. Prof. Naoki Kagi, and Dr. Takashi Nakamura, for their valuable comments on this thesis.

My thanks also go to Assoc. Prof. Jeremy David Bricker at Tohoku University and Assoc. Prof. Hiroshi Takagi at Tokyo Institute of Technology, for the fruitful discussions and valuable suggestions, especially on the computation and experiments of tsunami. I also thank Dr. Atsushi Watanabe and all other members of Nadaoka Laboratory for their kind help.

I would like to thank Prof. Nobuhisa Kobayashi at University of Delaware for his helpful advices throughout this work. I am also grateful for the advices given by Prof. Yoshiharu Matsumi at Tottori University on the laboratory experiments of fish reef blocks. I also appreciate the insightful comments given by Dr. Kenichiro Shimosako and Dr. Taro Arikawa at Port and Airport Research Institute on the design method for armor units against tsunami. I wish to thank Dr. Masato Yamamoto at Tripole Co., Ltd. for his guidance since he was a General Manager of Technical Research Institute of Fudo Tetra Corporation.

This thesis is primarily based on my research work conducted at Fudo Tetra Corporation that I work for, and was developed under the supervision of Prof. Kazuo Nadaoka. I would like to express my gratitude to Dr. Michio Matsuoka, General Manager of Block Environmental Business Division, Dr. Minoru Hanzawa, General Manager of Technical Research Institute, and Dr. Akira Matsumoto, Head of Hydraulics Division of Technical Research Institute, for giving me an opportunity of admission to doctoral program as well as giving me their guidance and encouragement all the time. I also thank Ms. Sanae Shibata, Mr. Shin-ichi Ogata, and Mr. Sohei Maruyama for their cooperation in conducting laboratory experiments. I am also thankful to all the members of the Technical Research Institute for their daily support.

Finally, I want to thank my family for always supporting me and encouraging me.